FEDERAL UNIVERSITY OF ITAJUBÁ
MECHANICAL ENGINEERING INSTITUTE

Vibration-Based Damage Localization in Composites Structures: Integrating CNNs, Mode Shapes, And Digital Image Correlation

Ronny Francis Ribeiro Junior

Itajubá – MG
2026

FEDERAL UNIVERSITY OF ITAJUBÁ
MECHANICAL ENGINEERING INSTITUTE

Vibration-Based Damage Localization in Composites Structures: Integrating CNNs, Mode Shapes, And Digital Image Correlation

Ronny Francis Ribeiro Junior

A thesis text presented to the Postgraduate Program of Mechanical Engineering, from Mechanical Engineering Institute of the Federal University of Itajubá, as a requirement to obtain the title of Doctor of Science in Mechanical Engineering.

Advisor: Prof. Dr. Guilherme Ferreira Gomes

Itajubá – MG
2026

Acknowledgements

I thank my parents, Ronny and Sandra, for all their support and encouragement. Thanks for all the education and affection. I also thank all my family members for their presence, encouragement, and trust placed in me.

My dissertation advisor, Guilherme Ferreira Gomes, for guidance and teachings that resulted in this work. I also thank all professors, staff, and colleagues from UNIFEI for contributing to my academic education.

I want to thank all my friends from PS Soluções for providing all the necessary equipment and helping with valuable knowledge. I also thank all my friends at Instituto Gnarus for the knowledge I've gained and the moments I've shared while working with you.

Finally, to God, who lights my way and puts people and opportunities in my life.

"I have no special talent. I am only passionately curious."

- Albert Einstein

Abstract

Composite sandwich structures offer high stiffness-to-weight ratios but are highly susceptible to complex internal damage mechanisms that are often difficult to detect using conventional inspection techniques. This work proposes a vibration-based Structural Health Monitoring (SHM) framework that integrates mode shape analysis, image processing techniques, Digital Image Correlation (DIC), and Convolutional Neural Networks (CNNs) for automated damage detection, localization, and sizing in composite sandwich structures. The investigated damage consists of a controlled stiffness-reduction region introduced by inserting a lower-stiffness material within the laminate, simulating internal debonding or delamination-type defects. A simulation-driven methodology is first established, in which mode shapes obtained from finite element models are transformed into image-based representations. These representations are used to train CNN models, demonstrating that image-based modal features outperform traditional approaches relying solely on global modal parameters, achieving detection accuracies above 90% under numerical conditions. The framework is further enhanced through physically informed image transformations, including residual-based representations, curvature enhancement, and multi-modal strategies that combine information from multiple vibration modes, as well as attention mechanisms embedded within the CNN architecture. These improvements lead to consistent performance gains, with accuracy increases of up to 10–15% and reductions of up to 20–30% in damage localization error compared to baseline image representations. Finally, the proposed framework is validated experimentally using mode shapes extracted from DIC measurements. Despite measurement noise, experimental uncertainty, and discrepancies between numerical and experimental domains, the models maintain robust performance, achieving damage detection accuracies above 85%, average localization errors below 10 mm, and reliable estimation of damage size under real testing conditions. The main contribution of this thesis is to demonstrate that vibration mode shapes, interpreted as spatial information, combined with advanced image representations and deep learning architectures, enable accurate localization and sizing of internal stiffness-reduction damage in real composite sandwich structures. These findings highlight the practical feasibility of the proposed methodology for real-world SHM applications.

Keywords: Sandwich structures, Mode shapes, Structural health monitoring, Machine learning, Damage detection, Damage localization.

Resumo

Estruturas sanduíche em materiais compósitos apresentam elevada relação rigidez-peso, porém são altamente suscetíveis a mecanismos complexos de dano interno, que frequentemente são difíceis de detectar por meio de técnicas convencionais de inspeção. Este trabalho propõe um framework de Monitoramento da Integridade Estrutural (SHM) baseado em vibrações, que integra análise de formas modais, técnicas de processamento de imagens, Correlação Digital de Imagens (DIC) e Redes Neurais Convolucionais (CNNs) para a detecção, identificação e localização automatizada de danos em estruturas sanduíche compósitas. Inicialmente, é estabelecida uma metodologia orientada por simulação, na qual formas modais obtidas a partir de modelos em elementos finitos são transformadas em representações baseadas em imagens. Essas representações são utilizadas para o treinamento de modelos CNN, demonstrando que características modais baseadas em imagens superam abordagens tradicionais fundamentadas exclusivamente em parâmetros modais globais, alcançando acurácia de identificação superior a 90% em condições numéricas. Em seguida, o framework é aprimorado por meio da introdução de transformações de imagem fisicamente informadas, incluindo representações baseadas em resíduos, realce de curvatura e estratégias multimodais que combinam informações de múltiplos modos de vibração, bem como mecanismos de atenção incorporados à arquitetura das CNNs. Essas melhorias resultam em ganhos consistentes de desempenho, com aumentos de acurácia de até 10–15% e reduções de até 20–30% no erro de localização de danos em comparação com representações de imagem de referência. Por fim, o framework proposto é validado experimentalmente utilizando formas modais extraídas a partir de medições por DIC. Apesar da presença de ruído de medição, incertezas experimentais e discrepâncias entre os domínios numérico e experimental, os modelos mantêm desempenho robusto, atingindo acurácia de identificação de danos superior a 85% e erros médios de localização inferiores a 10 mm. De modo geral, os resultados demonstram que a interpretação de formas modais de vibração como informação espacial e a combinação de representações de imagem com arquiteturas de aprendizado profundo constituem uma solução eficaz e robusta para o SHM automatizado de estruturas sanduíche compósitas, com elevado potencial para aplicações reais.

Palavras-chave: Estruturas sanduíche, Formas modais, Monitoramento da integridade estrutural, Aprendizado de máquina, identificação de danos, Localização de danos.

List of Figures

List of Tables

List of Abbreviations and Acronyms

AE	Acoustic Emission
ANN	Artificial Neural Network
AR	Autoregressive
$ARIMA$	Autoregressive Integrated Moving Average
$BVID$	Barely Visible Impact Damage
c	Semi-major axis of the ellipse (mm)
$CCFF$	Boundary condition: two opposite sides clamped, two sides free
$CCCC$	Boundary condition: all sides clamped
CDF	Cumulative Distribution Function
CI	Cornwell Indication
CLC	Conventional Load-Carrying
CNN	Convolutional Neural Network
$conf_{rx}$	Confidence radius in the x direction
$conf_{ry}$	Confidence radius in the y direction
$CFFF$	Boundary condition: one side clamped, three sides free
$CFRP$	Carbon Fiber Reinforced Polymer
CT	Computed Tomography
DIC	Digital Image Correlation
DL	Deep Learning
DOF	Degree of Freedom
E	Young's modulus (MPa or GPa)
EI	Electromechanical Impedance
EMA	Experimental Modal Analysis
$f()$	Activation function
FBG	Fiber Bragg Grating
$FFFF$	Boundary condition: all sides free
FEM	Finite Element Method
FFT	Fast Fourier Transform
FGM	Functionally Graded Material
FRF	Frequency Response Function
G_{12}	In-plane shear modulus (GPa)
GAN	Generative Adversarial Network
$GFRP$	Glass Fiber Reinforced Polymer
IC	Incremental Clustering
IDT	Impact Damage Tolerance
IGA	Isogeometric Analysis
KAN	Kolmogorov-Arnold Networks
KNN	K-nearest Neighbors
$LFRR$	Local Frequency Response Ratio
$LSTM$	Long Short-Term Memory
LVI	Low-Velocity Impact
MAE	Mean Absolute Error (mm)

MAC	Modal Assurance Criterion
ML	Machine Learning
MLP	Multilayer Perceptron
MSE	Mean Squared Error
NDT	Non-Destructive Testing
NFC	Natural Fiber-reinforced Composites
ν	Poisson's ratio
ν_{12}	In-plane Poisson's ratio
ODS	Operational Deflection Shape
OMA	Operational Modal Analysis
PCA	Principal Component Analysis
PDF	Probability Density Function
ϕ	Sub-sampling function
Φ^{-1}	Inverse cumulative distribution function
$PINN$	Physics-Informed Neural Network
PSD	Power Spectral Density
PSO	Particle Swarm Optimization
PZT	Piezoelectric Sensor
r	Aspect ratio of the ellipse
R^2	Coefficient of determination
$RAPID$	Reconstruction Algorithm for Probabilistic Inspection Damage
$ReLU$	Rectified Linear Unit
$RLCP$	Rectangular Laminated Composite Plates
$RMSE$	Root Mean Square Error
ROI	Region of Interest
ρ_{core}	Core density (kg/m^3)
ρ_{skin}	Skin density (kg/m^3)
se_x	Standard error in the x direction
se_y	Standard error in the y direction
SEM	Scanning Electron Microscopy
SGD	Stochastic Gradient Descent
SHM	Structural Health Monitoring
σ^2_{hx}	Variance of residuals in the x direction
σ^2_{hy}	Variance of residuals in the y direction
residual_x	Residual in the x direction
residual_y	Residual in the y direction
SNR	Signal-to-Noise Ratio
SVM	Support Vector Machine
$tanh$	Hyperbolic tangent
$TDCNN$	Temporal Derivative Cellular Neural Network
θ	Orientation angle of the ellipse (degrees)
$UHMWPP$	Ultra-high Molecular Weight Polypropylene
$WGFRP$	Woven Glass Fiber Reinforced Polymer
X	X-coordinate of the ellipse center (mm)
Y	Y-coordinate of the ellipse center (mm)
Z	Z-value from the standard normal distribution

Contents

1 Introduction

Composite materials constitute a versatile class of engineered materials formed by the combination of two or more distinct constituents without chemical reactions or mutual solubility, resulting in a material with enhanced properties compared to its individual components [1]. Inspired by natural composites such as wood, engineered composites exhibit outstanding strength-to-weight and stiffness-to-weight ratios, high fatigue and corrosion resistance, and remarkable design flexibility. These advantages have driven their widespread adoption in aerospace, defense, marine, civil engineering, automotive, and renewable energy applications [2–8].

Among composite systems, laminated and sandwich structures stand out due to their superior mechanical efficiency, enabling lightweight designs without compromising structural performance. However, the heterogeneous and anisotropic nature of composite materials gives rise to complex damage mechanisms, including delamination, matrix cracking, fiber breakage, skin–core debonding, porosity, and fiber misalignment. These defects may originate during manufacturing or develop progressively during service life, often evolving in a non-linear and interacting manner [9–13]. Unlike metallic structures, damage in composites is frequently internal and visually imperceptible, making early detection particularly challenging and increasing the risk of sudden and catastrophic failure, with severe safety and economic consequences [14].

Figure 1.1 illustrates the failure of the composite vertical stabilizer of an Airbus A300-600 involved in the American Airlines Flight 587 accident, one of the earliest and most emblematic catastrophic failures associated with a primary composite structural component in commercial aviation. The event highlighted the susceptibility of laminated composite structures to internal damage mechanisms, such as delamination, under complex dynamic loading conditions, and demonstrated how severe loss of load-carrying capacity may occur without clear external visual indications. This case underscores the critical importance of developing reliable techniques capable of identifying the onset and progression of damage in composite materials before catastrophic failure occurs.

To address these challenges, Structural Health Monitoring (SHM) has emerged as a key strategy for ensuring the integrity, safety, and reliability of composite structures. SHM systems aim to provide continuous or periodic assessment of structural condition, enabling early damage detection, reducing inspection downtime, and minimizing maintenance costs [14, 15]. A wide range of non-destructive testing (NDT) and SHM techniques has been proposed for composite materials, including ultrasonic testing, X-ray inspection, acoustic emission, optical methods, guided waves, and vibration-based approaches [16–22].

Among these techniques, vibration-based SHM methods have gained particular prominence due to their global inspection capability, cost-effectiveness, and suitability for in-service monitoring. Structural damage typically induces changes in mass, stiffness, and damping properties, which affect modal parameters such as natural frequencies, mode shapes, and damping ratios [23, 24]. Although natural frequencies are widely used as damage indicators, they are generally insufficient for accurate damage localization, particularly in complex composite structures. Consequently, increasing attention has been directed toward mode shape-based methods, which are more sensitive to localized stiffness variations and provide richer spatial information for damage identification [25, 26].

Despite their potential, the high dimensionality, noise sensitivity, and complexity of modal data in composite structures pose significant challenges for traditional signal processing and feature-based approaches. In parallel, the growing availability of sensing systems has led to large volumes of data, demanding advanced data-driven techniques capable of efficiently extracting meaningful patterns. In this context, machine learning methods have attracted considerable interest in the SHM community due to their ability to model complex, non-linear relationships directly from data [27].

In particular, Convolutional Neural Networks (CNNs) have demonstrated remarkable success in image-based applications and have increasingly been adopted for structural damage detection and localization tasks [28, 29]. CNNs are capable of automatically learning hierarchical features from raw or processed data, making them well-suited for capturing the spatial patterns associated with damage in composite structures. Moreover, recent advances in image processing techniques have shown strong potential to further enhance CNN performance by emphasizing damage-sensitive features, reducing noise, and improving contrast, thereby facilitating more accurate damage interpretation [30, 31].

The integration of vibration-based mode shape analysis with CNNs represents a promising framework for composite SHM, particularly for sandwich structures where damage may occur in skins, interfaces, or cores. Nevertheless, accurately detecting, localizing, and quantifying internal damage under realistic experimental conditions remains an open research challenge. Most existing approaches focus primarily on damage identification under numerical conditions or on detection without precise spatial quantification, and few studies demonstrate reliable localization and sizing of internal stiffness-reduction damage in real composite sandwich structures.

Motivated by these limitations, this thesis proposes an intelligent Structural Health Monitoring framework that integrates vibration-based mode shape information, advanced image processing techniques, Digital Image Correlation (DIC), and Convolutional Neural Networks to detect, localize, and estimate the size of damage in composite sandwich structures. The investigated damage consists of a controlled stiffness-reduction region introduced by inserting a lower-stiffness material within the laminate, simulating internal debonding or delamination-type defects. The proposed methodology not only identifies different damage scenarios but also determines their spatial position and estimates their dimensions under real experimental conditions. By combining numerical simulations and experimentally measured mode shapes under different boundary conditions, the framework demonstrates that vibration mode shapes interpreted as spatial information, when coupled with deep learning architectures, enable accurate localization and sizing of internal damage in practical composite structures. This constitutes the main contribution of the thesis and advances the applicability of vibration-based SHM toward real-world structural systems.

1.1 Research Objective

The main objective of this doctoral research is to develop and validate an intelligent Structural Health Monitoring (SHM) framework for the accurate detection, localization, and sizing of multiple damage mechanisms in composite sandwich structures, using vibration-based mode shape information and data-driven learning techniques.

To achieve this main objective, the following specific objectives are defined:

- To investigate the sensitivity of vibration mode shapes to different damage mecha-

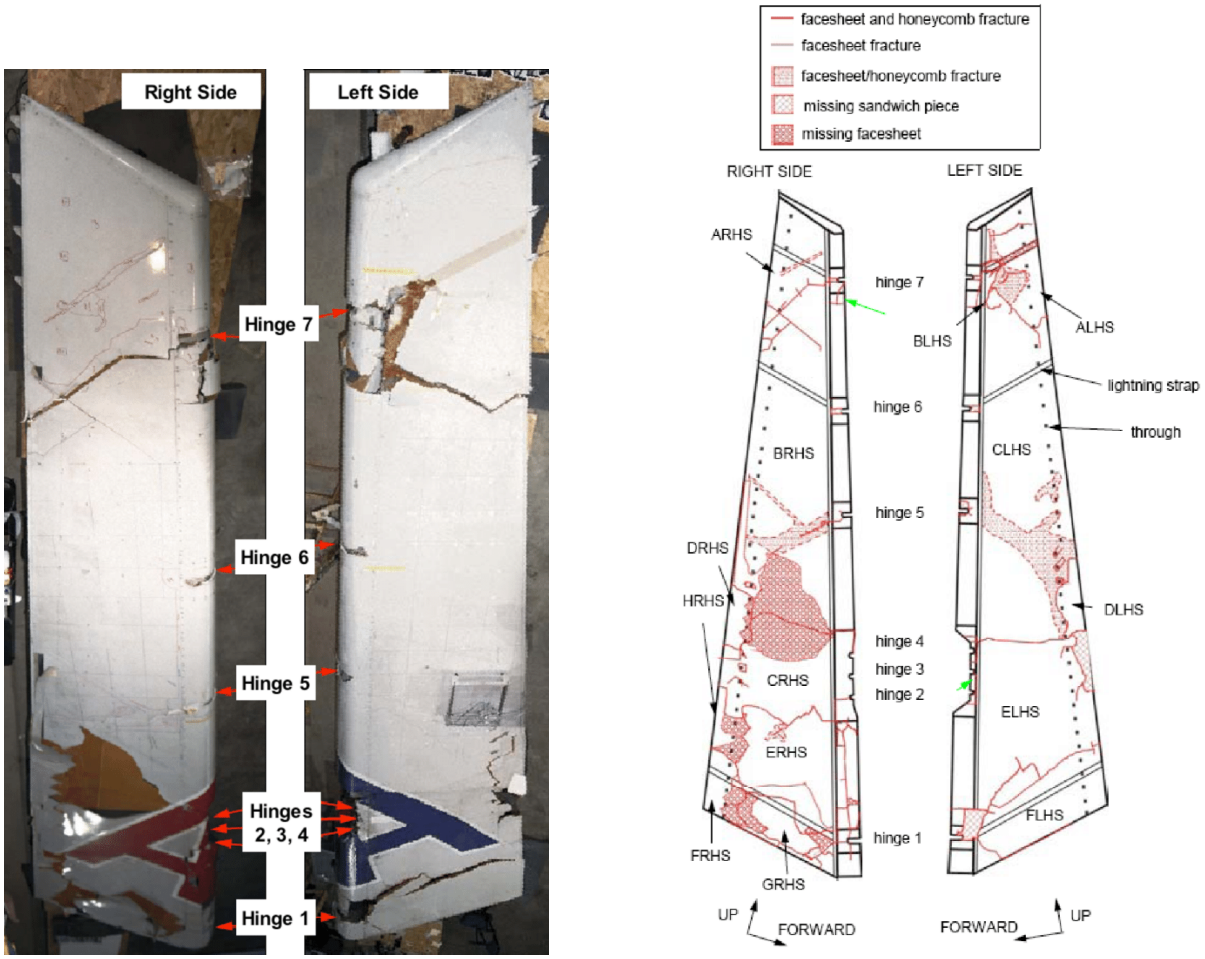

Figure 1.1: Failure of the composite vertical stabilizer of an Airbus A300-600 involved in the American Airlines Flight 587 accident.

nisms in composite sandwich structures under varying boundary conditions;

- To develop high-fidelity numerical models capable of realistically representing the mechanical behavior and damage evolution of composite sandwich plates;
- To construct a simulation-driven dataset of mode shape information suitable for training and validating data-driven damage identification models;
- To design and implement Convolutional Neural Network (CNN) architectures for damage detection, localization and sizing based on mode shape representations;
- To evaluate the influence of image processing techniques on enhancing damage-sensitive features and improving CNN performance;
- To integrate experimental measurements, including vibration testing and Digital Image Correlation (DIC), to validate the proposed framework under realistic conditions;
- To assess the robustness and generalization capability of the proposed SHM framework across different damage scenarios and boundary conditions.

1.2 Thesis Text Outline

This Thesis text is organized as follows: Chapter 2 presents a systematic review of machine learning techniques applied to damage assessment in composite structures, identifying current research trends and existing gaps. Chapter 3 describes a numerical framework that integrates finite element modeling, vibration mode shapes, and Convolutional Neural Networks for damage detection and localization in composite sandwich panels under different boundary conditions. Chapter 4 extends the proposed approach by incorporating image processing techniques and attention mechanisms to enhance damage-sensitive features in mode shape images and improve model performance. Chapter 5 presents the experimental validation of the proposed framework using vibration measurements obtained via Digital Image Correlation, assessing robustness against noise and numerical–experimental discrepancies. Chapter 6 summarizes the main conclusions and outlines directions for future research.

2 Machine Learning for Damage Assessment in Composite Structures: A Review

In this chapter, a review of the main and most recent works on machine learning methods for the damage assessment of composite structures is presented. The selected studies are covered in detail to provide researchers with an in-depth understanding of the latest advancements in machine learning algorithms for the damage assessment of composite structures. Finally, future research directions and a summary of all selected works are suggested, highlighting potential improvements to the current state of the art.

The chapter is organized as follows: Section 2.1 presents the basic concepts of the main machine learning methods. In Section 2.2 the methodological procedure used in the review is presented. The results of this review are systematically identified and discussed in Section 2.3. Section 2.4 provides research directions for the future. Finally, Section 2.5 concludes the study by highlighting the main aspects of the reviewed studies.

2.1 Machine Learning

Machine learning refers to an algorithm that creates a model by using a set of sample data, known as training data, to make predictions or decisions without requiring explicit programming [32]. There are two main types of machine learning methods: supervised and unsupervised, which differ based on the use of labeled datasets. Essentially, supervised learning algorithms use labeled input and output data, while unsupervised learning algorithms do not rely on labeled data. Within the category of unsupervised algorithms, there is a specific subgroup known as clustering, which is utilized in multivariate data sets to identify related groups of elements. Meanwhile, supervised methods are broadly categorized into two types: classification and regression approaches. Classification methods are used to predict class labels, while regression approaches are used to determine the most appropriate model for the given data. Figure 2.1 provides a visual representation of the divisions and subdivisions of machine learning algorithms.

A recent type of learning, known as reinforcement learning, has been developed for particular tasks. This approach involves the algorithm interacting with a changing environment to accomplish a specific objective, such as playing a game [33]. The objective of this form of learning is to increase the number of positive outcomes as the algorithm "plays the game". However, it is a very recent type of learning that is still in development, so, there are still not enough cases applied to composite structures to make a review.

Two methods are being used to enable intelligent structural damage diagnosis. The first method involves utilizing modern sensor technology in combination with numerical simulation approaches to collect monitoring data that can help determine the state of structural deterioration. The second method involves using machine-learning algorithms to extract concealed features from the monitoring data for intelligent structural damage diagnosis [34, 35].

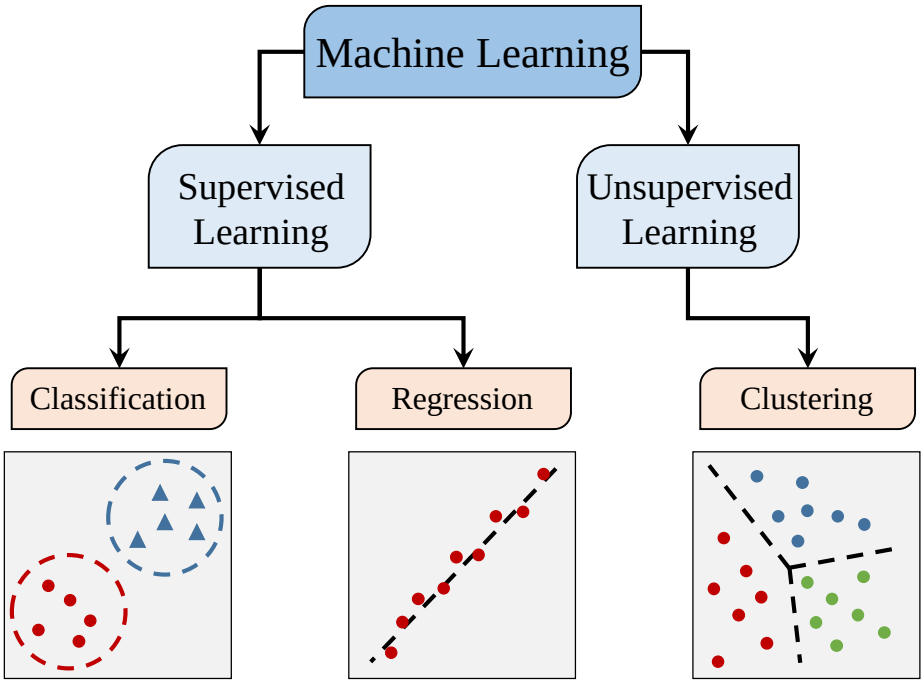

Figure 2.1: Divisions and subdivisions of machine learning algorithms.

In the upcoming sections, a general introduction to the key machine-learning techniques utilized to assess damage to composite structures will be presented. As the focus of this study is to provide a practical discussion of the application of the method, the mathematical details of the algorithms will not be explored in depth.

2.1.1 Artificial Neural Network

Artificial neural networks are computer models that mimic the activity of the human brain. They use basic processing units called neurons, which work like biological neurons, to perform calculations. These neurons are connected by weights, and during the training process, these weights are adjusted based on the data supplied to the network [36]. Figure 2.2 depicts a simple neuron model. In this work, the term ANN refers to the most classical and fundamental neural network architecture, namely the Multi-Layer Perceptron (MLP), which is a feedforward network composed of an input layer, one or more hidden layers, and an output layer.

The way an Artificial Neural Network behaves is influenced by both the arrangement of connections (topology) between its neurons and the strength of those connections (synaptic values). The parameters that determine the entire functioning of the ANN are [37]:

- Number of neuron layers
- Number of neurons per layer
- Types of connections between neurons
- Degree of connectivity between neurons

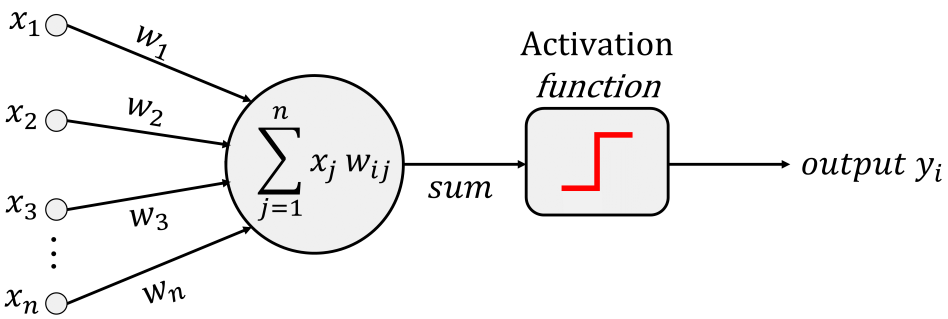

Figure 2.2: Artificial neuron representation (adapted from [37]).

2.1.2 Autoregressive Models

Autoregressive models are statistical models that aim to predict the value of a variable of interest. These models are commonly used when there is a correlation between past and future data in a series [38]. AR models are essentially linear regressions of data, where the future value is predicted based on one or more previous data points within the same series. However, due to the stochastic nature of AR models, there is a level of uncertainty and unpredictability associated with them, meaning that every forecast should be considered a trend with some level of confidence attached to it. Therefore, it is impossible to make predictions with 100% certainty.

AR model is typically denoted by $AR(p)$, where p is the order of the model. The order of an AR model refers to the number of past values in the series that are used to predict its future values. For instance, an $AR(1)$ model is a first-order model that makes use of only one previous measurement to forecast future values. The $AR(p)$ model is defined by the Equation 2.1 [39]:

$$X_t = \sum_{i=1}^{p} \varphi_i X_{t-1} + \varepsilon_t \tag{2.1}$$

where: φ_i are the AR Coefficients and ε_t is a Gaussian white-noise.

There are currently various autoregressive models that integrate different approaches to improve prediction performance. One such model is ARIMA, which is particularly noteworthy for its effectiveness [40].

2.1.3 Bayesian Classifier

A Bayesian classifier is a type of model that uses probability to predict classes within a given set of data. The model also enables the calculation of probabilities for both the classes and their associated variables. When there is no specific knowledge about the data, an approach commonly used is to assume "uninformed priors", which assigns equal probabilities to each class and attribute value [41].

The Bayesian classifier is a fundamental algorithm for classifying an instance by determining the probability of it being assigned to a specific class, such as Q1. This involves the computation of probabilities according to Equation 2.2 [42]:

$$P(C_i | A_1 = V_{1_j} \& \cdots \& A_N = V_{N_j}) \tag{2.2}$$

where an example is represented by attribute-value pairs of the form $A_i = V_i$.

If there are N independent attributes, then the probability is equal to Equation 2.3 [42]:

$$P(C_i) \prod_k P(A_k = V_{k_j} | C_i) \tag{2.3}$$

when this independence assumption is made, the classifier is called Naive Bayes.

Naive Bayesian classifiers have a significant advantage over probabilistic classification algorithms due to their straightforward and commonly used approach for performing classification tasks. This advantage is derived from their ability to calculate class and conditional probabilities, making them robust to noise, and the statistical foundation that enables them to scale effectively across domains with many irrelevant features [43].

The naive Bayesian classifier relies on two important assumptions. Firstly, it assumes that each class can be represented by a single probability distribution, and secondly, it assumes that the probability distributions of the features within each class are independent of each other. However, these assumptions may limit the model and result in reduced classifier accuracy in certain scenarios [43, 44].

2.1.4 Convolutional Neural Network

A method of learning called convolutional neural network, which was first proposed by Lecun [45], uses a feed-forward neural network to extract data by employing a convolution structure [46]. Its primary function is to classify input images into various categories. A CNN is composed of two main components: one for selecting features and another for classification. The feature selection part consists of an input layer, convolutional layer, and a pooling layer, while the classification part comprises a fully connected layer and an output layer. Figure 2.3 shows an example of a CNN architecture.

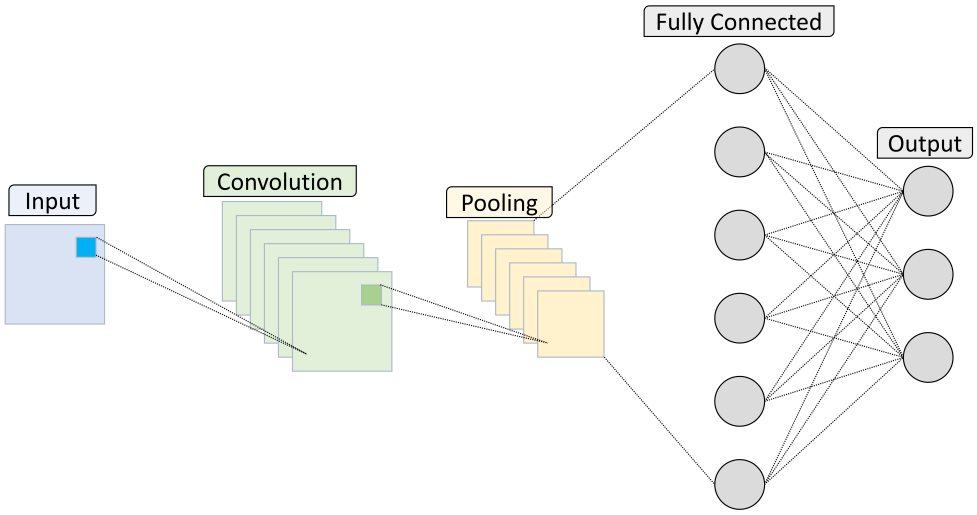

Figure 2.3: A basic architecture of Convolutional Neural Network (adapted from [47]).

Recently, a specialized variant of CNN called the 1D CNN has emerged, which utilizes a signal or 1D data as input instead of an image [48]. Despite this difference, the architecture of 1D and 2D CNNs are highly similar, except for the filter sliding mechanism. In the case of 1D CNN, the filter moves vertically (along the height dimension) to extract features, and the height determines the number of sample points involved in the convolutional

process. In contrast, the 2D CNN filter slides both horizontally and vertically (height and width) across the entire matrix.

2.1.5 K-Means and K-Nearest Neighbors

K-means, also known as K-means clustering, is an unsupervised learning technique that partitions data into predetermined classes through iterative convergence [49]. Initially, the algorithm randomly selects K cluster centers or centroids, where K is predetermined. Then, the data are allocated to the closest centroid based on the Euclidean distance [50]. The algorithm iteratively determines new centroids until convergence is achieved while minimizing the sum of the squared errors [51].

K-nearest neighbor is a type of supervised learning method that is utilized for solving both classification and regression tasks. The fundamental principle behind KNN involves analyzing the distance between each data point in a given dataset and its nearest neighbors, typically by utilizing Euclidean distance calculations [50]. If the majority of the nearest neighbors for a specific sample are of a particular category, then that sample is classified into that category. Although KNN algorithms are simple to apply, they have certain restrictions when working with multi-dimensional data that has irrelevant attributes. Additionally, there is no fixed rule to determine the ideal value for K [51].

K-means and KNN are two distinct algorithms that are often mistakenly interchanged because of their similar names. To provide clarification, the "K" in K-means specifies the number of classes, whereas the "K" in KNN refers to the number of nearest neighbors. Nevertheless, it is common in research literature to observe the utilization of these two algorithms in conjunction.

2.1.6 Principal Component Analysis

Principle component analysis is a statistical technique that utilizes a vector space transformation to decrease the number of potentially correlated variables, also known as principal components. PCA was initially developed for analyzing multivariate data, but it has now found applications in a variety of other fields [52]. As a result of its many advantages, PCA has become the most commonly used multivariate statistical approach in the scientific community [53].

If a dataset X with standardized zero-mean values, and a matrix of size $m \times n$, where m denotes the number of unique parameters and n represents the number of measurements for each parameter, then the the covariance matrix can be obtained C_X using Equation 2.4 [54]:

$$C_X = \frac{1}{n} X X^T \tag{2.4}$$

PCA involves finding an orthonormal matrix P that linearly transforms X into $Y = PX$, leading to a diagonal covariance matrix C_Y. The off-diagonal terms in C_Y should be zero, indicating uncorrelated variables. Furthermore, the subsequent dimensions in Y must be ordered by variance, with the primary components being the arranged set of p_i elements. Equation 2.5 represents the rewritten form of C_Y [54]:

$$C_Y = \frac{1}{n}(PX)(PX)^T = P C_X P^T \tag{2.5}$$

Since the covariance matrix C_X is symmetric, the matrix can diagonalize by using the orthonormal eigenvector matrix E, such that $C_X = EDE_T$. By selecting $P = E_T$ and

recognizing that the inverse of an orthogonal matrix is its transpose, the Equation 2.6 [54] can be obtained.

$$C_Y = P(EDE^T)P^T = D \tag{2.6}$$

Where C_Y is a diagonal matrix. Thus, the principal components of X is the eigenvectors of C_X.

In short, PCA aims to find a new set of meaningful and independent dimensions by linearly combining the original variables. This results in a transformed data set with reduced noise and potentially reveals hidden patterns or information.

2.1.7 Support Vector Machine

Supervised learning algorithms called Support Vector Machines are utilized for classification and regression to detect patterns in data. The conventional SVM takes a dataset as input and predicts whether the input belongs to one of two classes, without relying on probabilities, thereby functioning as a binary linear classifier. The primary objective of SVMs is to construct a decision boundary that maximizes the margin between the two classes. [55]

In simple terms, the goal of SVM is to locate a line, or hyperplane, that can divide data into two distinct classes. This hyperplane, as shown in Figure 2.4, aims to optimize the distance between the nearest points of each class [56]. The ideal hyperplane is the one with the greatest margin of separation between the classes. Although margin maximization is a measure of SVM's effectiveness, the technique prioritizes class division over margin maximization, indicating that categorizing the classes accurately is more critical than maximizing the margin.

In addition to linear classification, SVMs may do non-linear classification effectively by employing the kernel technique, which involves implicitly mapping their inputs into high-dimensional feature spaces [57].

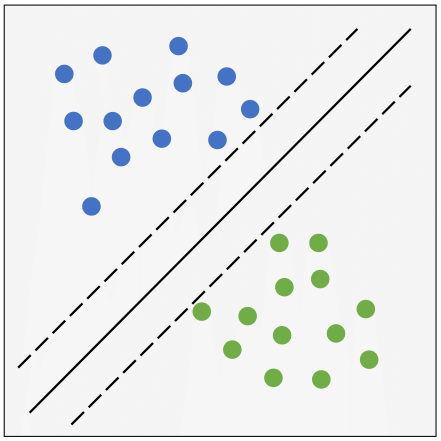

Figure 2.4: A graphical representation of an SVM (adapted from [58]).

2.1.8 Comparison of machine learning algorithms

Due to the distinct characteristics and objectives of various machine learning methods, along with their heavy reliance on data and data formats, making direct comparisons

between them to highlight advantages and disadvantages can be challenging. However, by analyzing each method carefully, that is, evaluating where each algorithm is generally applied and how it is, it is possible to extract certain general characteristics that indicate the advantages and disadvantages of each method. It's worth noting that there are cases where unconventional utilization of certain algorithms can yield favorable outcomes. Table 2.1 presents a general guide to the theoretical advantages and disadvantages of each machine learning method.

Table 2.1: Theoretical advantages and disadvantages of each machine learning algorithm (adopted from [59]).

Algorithm	**Advantages**	**Disadvantages**	**Training time**
Artificial Neural Network	Capability to learn and understand nonlinear and complex relationships	Difficult to comprehend and interpret	Long
Autoregressive Models	Simple Implementation	When the autocorrelation coefficient is less than 0.5, the prediction is inaccurate	Average
Bayesian Classifier	A simple technique, with only a small amount of training data necessary	There is no interdependence between the features	Average
Convolutional Neural Network	Obtaining major conclusions from data collection is quick and simple	Difficult to comprehend and interpret	Long
K-Means	Simple Implementation	high dependence on initial parameters	Average
K-Nearest Neighbor	Simple Implementation	In a high-dimensional space, it is easy to overfit	Quick
Principal Component Analysis	Excellent downscaling ability	Poor naming clarity	Quick
Support Vector Machine	Effective in high-dimensional spaces	Kernel function sensitive	Long

2.2 Review Methodology

This section presents the methodology used in the systematic review. In these steps, some guidelines are followed to select the best and most influential papers related to the topic of machine learning on damage assessment of composite structures.

The Scopus database was used as a screening tool to select the most suitable papers for the study. In it, keywords were used to find articles that matched the desired topic. The keywords were combined using Boolean operators, that is, AND and OR, resulting in the following search:

> (damage OR assessment OR detection OR quantification OR localization) AND
> (composite OR fiber OR polymer OR laminate) AND
> (machine learning OR support vector machine OR principal component analysis OR k-means OR K-nearest neighbors OR convolutional neural network OR Bayesian classifier OR auto-regressive model OR artificial neural network).

Other filters were also used to further narrow down the results. The surveys only included articles; conference papers, Ph.D. theses, books, editorial comments, and technical reports were not included. This was done to choose articles with the highest level of research outputs and that have been extensively peer-reviewed. Furthermore, only publications published between January 2012 and December 2022 were evaluated to avoid picking research that is no longer pertinent to the topic. After the first screening, the abstracts of the selected articles were reviewed. Those who had an abstract that did not discuss something related to damage assessment in composite structures using machine learning were also excluded.

2.3 Results and Discussion

In this section, the results obtained with the systematic review in addition to the discussions are presented. It is comprised of Research trends, Publication venues, and the Selected studies as mentioned in Section 2.2

2.3.1 Research Trend

So, sorted by year of publication, that until 2018, there were few publications on damage assessment using machine learning techniques. It was only after 2019 that can see an increase in the number of publications on the topic. This indicates its current relevance and ongoing development. Figure 2.5 shows the trend.

2.3.2 Publication Venue

In this subsection, the distribution of the selected studies in this subsection by taking into account the published channels is presented. The studies appeared in a total of 37, where Composites Structures Journal (14 articles) takes the predominant publication on the topic. It is followed by Structural Health Monitoring and Sensors, both with 6 articles. With 3 articles published, Composites Part B: Engineering, IEEE Access, Journal

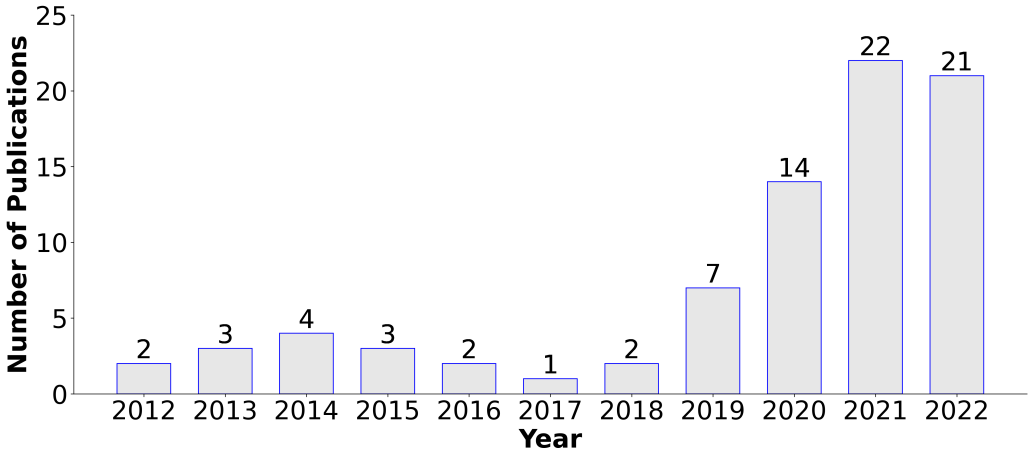

Figure 2.5: Number of publications per year.

of Intelligent Material Systems and Structures, and Journal of Nondestructive Evaluation. The other journals that share the same number of publications (2 articles) are Applied Acoustics, Applied Composite Materials, Composites Science and Technology, Cement and Concrete Composites, Materials, Proceedings of the Institution of Mechanical Engineers, Part C, and Smart Materials and Structures. Lastly, the rest journals published only one article. Table 2.2 shows all publication journals, number of articles, and publishers.

2.3.3 Selected Studies

As previously mentioned, there has been a rise in the amount of work utilizing machine learning approaches for damage assessment of composite structures in recent years. This is mainly due to the greater use of composites in the industry, which consequently requires greater monitoring of the condition of the material in order to guarantee reliability as a whole. This subsection is dedicated to state-of-the-art approaches for damage assessment of composite structures based on machine learning techniques. Figure 2.6 shows the contribution of each machine-learning technique to the overall studies chosen. The majority of research uses ANN (24.7%), followed by CNN and PCA accounting for 22.4% and 14.1%, respectively. K-means and KNN account for 12.9% and 3.5% of the total studies, respectively. SVM accounts for 11.8% of the total analyzed studies. Finally, the Bayesian classifier and AR-model account for 5.9% and 4.7% of all studies, respectively.

Artificial Neural Network Studies

Ramasamy and Sampathkumar [60] propose using Acoustic Emission and an Artificial Neural Network to assess drop impact damage on woven glass fiber reinforced polymer (WGFRP) composite laminates. The ANN trained with AE parameters accurately predicts impact damage tolerance. The average error tolerance of the estimated impact damage tolerance was 3.35%, indicating good agreement.

In another study by Ramasamy and Sampathkumar [61] extend their previous method by combining AE and ultrasonic techniques for offline and online monitoring of drop impact damage on WGFRP composite laminates. The ANN-based approach provides a real-time prediction of Impact Damage Tolerance.

Table 2.2: Dissemination of the selected articles (in number of articles).

No	Journal	Publisher	#
1	Composite Structures	Elsevier	14
2	Sensors	MDPI	6
3	Structural Health Monitoring	SAGE	6
4	Composites Part B: Engineering	Elsevier	3
5	IEEE Access	IEE	3
6	Journal of Intelligent Material Systems and Structures	SAGE	3
7	Journal of Nondestructive Evaluation	Springer	3
8	Applied Acoustics	Elsevier	2
9	Applied Composite Materials	Springer	2
10	Composites Science and Technology	Elsevier	2
11	Cement and Concrete Composites	Elsevier	2
12	Materials	MDPI	2
13	Proceedings of the Institution of Mechanical Engineers, Part C	SAGE	2
14	Smart Materials and Structures	IOPscience	2
15	Acta Mechanica Sinica	Springer	1
16	Advances in Engineering Software	Springer	1
17	Advances in Mechanical Engineering	SAGE	1
18	Applied Sciences	MDPI	1
19	Engineering Structures	Elsevier	1
20	Heliyon	Elsevier	1
21	International Journal of Damage Mechanics	SAGE	1
22	International Journal of Integrated Engineering	UTHM	1
23	International Journal of Mechanical Sciences	Elsevier	1
24	Iranian Journal of Science and Technology	ACM	1
25	Journal of Intelligent Manufacturing	Springer	1
26	Journal of Process Control	Elsevier	1
27	Journal of Reinforced Plastics and Composites	SAGE	1
28	Journal of The Institution of Engineers (India): Series C	Springer	1
29	Journal of Vibration and Control	SAGE	1
30	Journal of Vibration Engineering & Technologies	Springer	1
31	Machine Vision and Applications	Springer	1
32	Nondestructive Testing and Evaluation	Taylor & Francis	1
33	Optik	Elsevier	1
34	Structural Monitoring and Maintenance	Korea Science	1
35	Structure and Infrastructure Engineering	Taylor & Francis	1
36	JOM	Springer	1
37	Ultrasonics	Elsevier	1

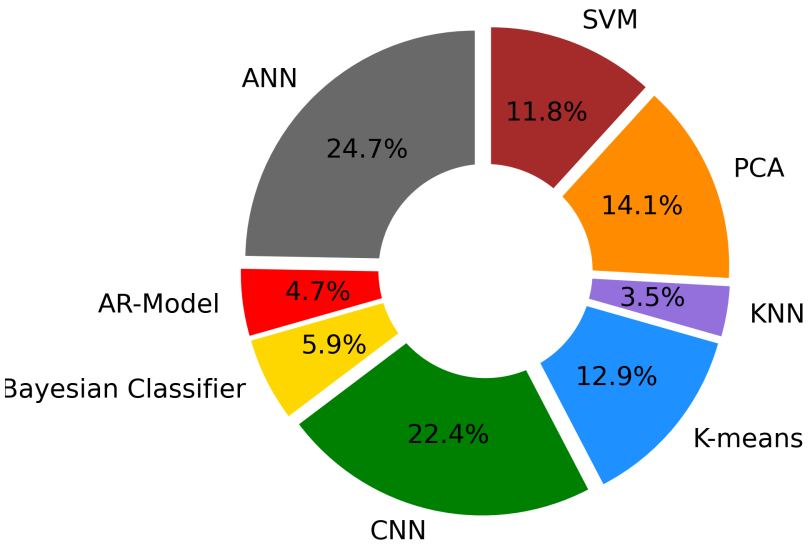

Figure 2.6: Percentage of articles chosen within machine learning topics.

Khatir *et al.* [62] propose a novel approach combining Cornwell Indication, Artificial Neural Network, and Particle Swarm Optimization to estimate damage in laminated composite plates. The method achieves high accuracy in damage quantification and significant time savings.

Qian *et al.* [63] introduces a non-destructive damage detection technique for fiber-reinforced composite structures using Lamb waves and an ANN model. The study involved simulating damages of varying sizes on a unidirectional carbon fiber-reinforced polymer composite plate using rectangular Teflon tapes. The ANN accurately quantifies damage size in these structures.

Califano *et al.* [64] describes a passive structural health monitoring method using strains and an ANN to detect damage in carbon fiber/epoxy composite plates. The approach successfully detects abnormal conditions, even if they are not structurally significant.

Zenzen *et al.* [65] propose a new damage detection method combining the transmissibility approach with ANN for improved local frequency response ratio predictions in composite structures. The method reduces data requirements and offers accurate damage prediction compared to conventional ANNs. The training results of each damage scenario are presented in Figure 2.7.

Mardanshahi *et al.* [66] investigates a nondestructive assessment system for detecting core cracking and skin/core debonding in foam core sandwich structures. A large dataset of the damaged sandwich structure's first five harmonic frequencies with varying damage amounts and locations was generated using the updated finite element model. The combination of experimental data, ANN, and finite element models shows promise for nondestructive evaluation.

Tan *et al.* [67] uses vibration characteristics and ANN to detect damage in composite bridge construction. They combined the ANN with a damage index based on modal strain energy to identify and measure damage in the steel beams. The method successfully identifies and measures deterioration in composite concrete slabs on steel girder bridges.

Jang *et al.* [68] presents a technique to identify debonding damage using natural frequency and an ANN. The authors simulated over a thousand debonding damages with

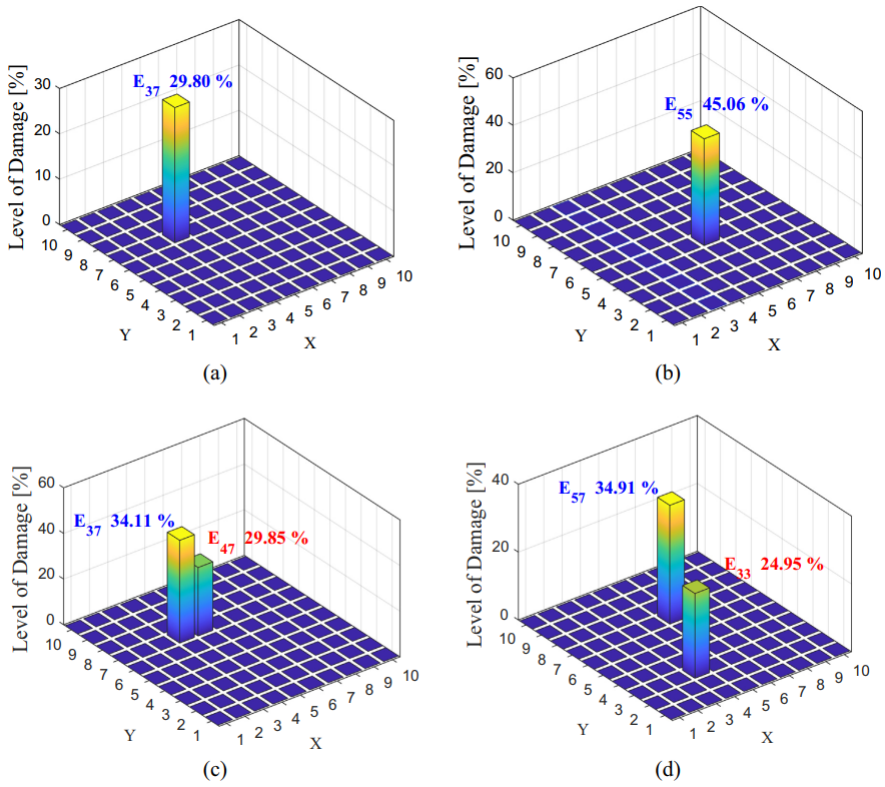

Figure 2.7: Damage quantification in cross-ply composite plate: a) scenario 1, b) scenario 2, c) scenario 3, and d) scenario 4, (adapted from [65]).

different configurations, positions, and lengths using modal analysis from a Finite element model. The method achieves a high success rate in detecting damage.

Khatir *et al.* [69] proposes a two-stage method for damage detection, localization, and measurement in functionally graded material plate structures. The authors employed isogeometric analysis to model the FGM plates, which is a more efficient approach than traditional finite element analysis. An improved ANN-based approach accurately identifies damaged components.

Tran-Ngoc *et al.* [70] develops an efficient approach for detecting damage in laminated composite structures using an ANN and a hybrid metaheuristic optimization algorithm. The method surpasses standard ANNs in terms of accuracy and reduces computing time.

Nasser *et al.* [71] explores using the piezoresistive properties of LIG interlayered fiberglass composites for damage assessment using ANNs. A two-layer Bayesian regularized ANN with 40 neurons in each layer achieved a higher level of accuracy compared to conventional degradation models.

Al-Athel *et al.* [72] combines hybrid thermography, computational modeling, and ANN techniques to analyze defects in composites. The hybrid technology accurately predicts both the form and magnitude of damage.

Feng *et al.* [73] proposes a method to locate low-velocity impacts on a composite plate using multi-frequency properties of impact-induced guided waves. Fusion techniques involving ANN achieve accurate localization of damage. Then the images were added to get the localization results with multi-frequency fusion 2.8.

Saadatmorad *et al.* [74] presents a method for damage quantification in rectangular laminated composite plates using wavelet transforms and ANN. The findings show that the proposed method can accurately quantify damage in rectangular laminated composite

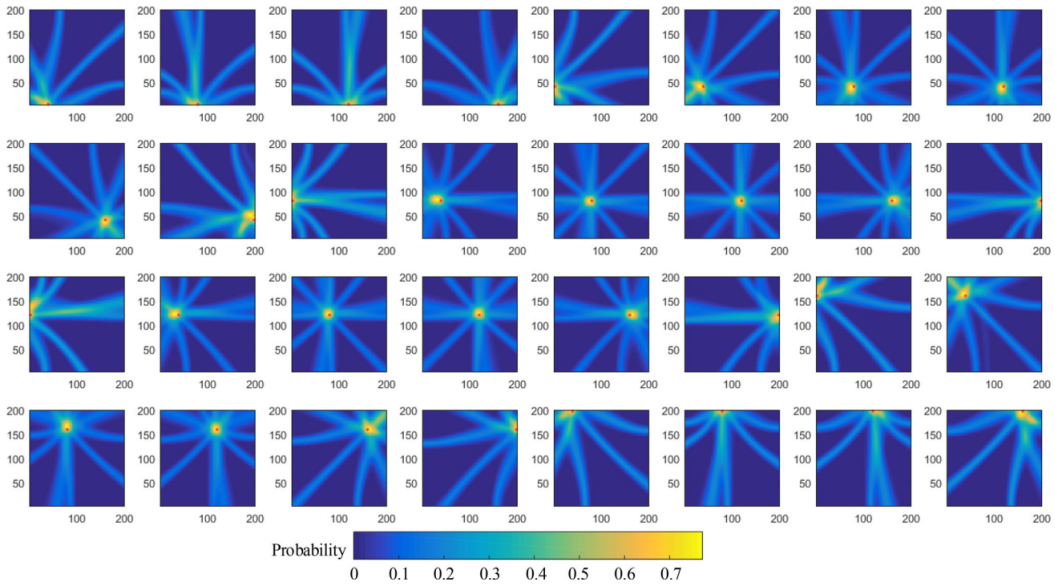

Figure 2.8: Imaging results of the 32 impacts, horizontal and vertical axes of each image are in the unit of mm, color bar shows the value of probability (adapted from [73]).

plates (with R = 0.992) and that the presence of "edge noise" can be a concerning factor in damage diagnosis algorithms that rely on wavelet transformations.

Reis *et al.* [75] develops a method to detect and classify damage in glass fiber-reinforced plastic composite beams using an ANN and vibration data. The technique shows promise in identifying damage based on dislocated time series parameters.

Overall, these articles collectively contribute to the advancement of damage detection and assessment techniques in composite structures using the most diverse sensing technologies, such as acoustic emission, strain signals, impact signals, lamb waves, and others, which have been combined with good scalability and strong nonlinear generalization of ANNs. In general, the ANNs used in the damage assessment of composite materials were of the feed-forward type, with one to two hidden layers and an average of 20 neurons per layer. Matlab® software was the most commonly used in their development. These research efforts aim to enhance the safety, reliability, and longevity of composite structures in various industries.

Autoregressive Models Studies

Mouzakis *et al.* [76] conducted a study on the impact of aging on carbon fiber-reinforced composites using AR-models. They subjected composite plates to two aging scenarios and performed impact testing on aged and non-aged composites. The results showed that impact test data could distinguish between aged and non-aged specimens and assess the level of damage. The study also correlated impact test behavior with changes in the mechanical properties of aged specimens.

Nardi *et al.* [77] explored the use of AR models for detecting delaminations in carbon-fiber-reinforced-plastic laminate plates caused by low-velocity impacts. They employed piezoelectric patches for actuation and sensing and utilized the captured signal to generate an AR Model. Linear Discriminant Analysis was applied to enhance delamination detection. The technique showed high success rates in identifying delamination-induced damage with a small number of sensors.

da Silva *et al.* [78] proposed a data-driven approach using multiple AR models to predict the time-series outputs of a PZT sensor detecting Lamb waves in composite specimens. They demonstrated a good correlation between the extrapolated model's estimations and observed damage progression. The method offers the advantage of achieving this task without complex mathematical-physical models.

Paixão *et al.* [79] investigated the use of stochastically interpolated global damage indices (DI) based on Gaussian process regression for measuring delamination area. They utilized AR models to extract damage-sensitive features from Lamb wave signals and calculated damage indices using the Mahalanobis squared distance. The methodology was tested on carbon epoxy laminate with simulated damage and carbon fiber-reinforced polymer coupons with real delamination. It effectively predicted the affected region for both simulated damage and actual delamination. Figure 2.9 shows, for the application case I, the damage indices computed sequentially for all tested conditions.

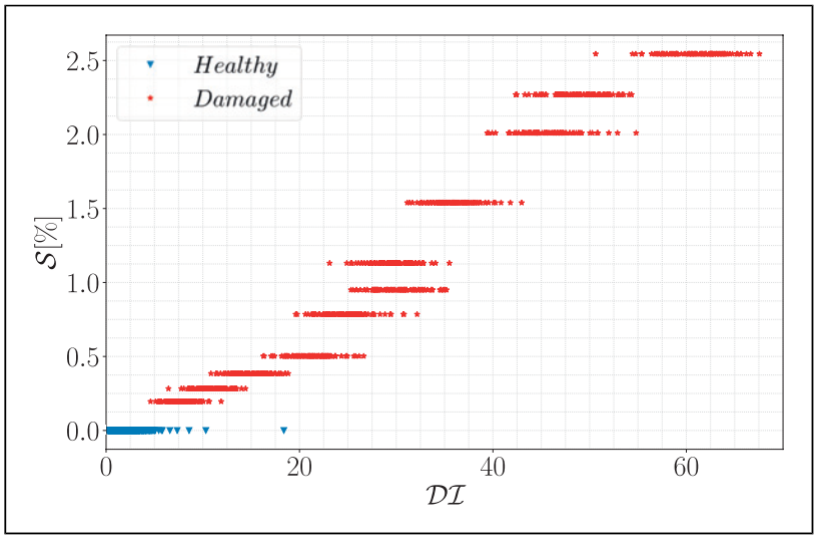

Figure 2.9: DI computed for all signals in application case I: carbon–epoxy plate (adapted from [79]).

In summary, the application of AR models has shown promising results in composite material damage assessment. These methods have demonstrated their capability to distinguish between aged and non-aged specimens, detect delaminations, predict damage progression, and measure the delamination area. They offer advantages such as capturing the effects of aging, requiring a small number of sensors (Usually Piezoelectric sensors), and providing cost-effective solutions without the need for complex mathematical-physical models. These findings highlight the potential of machine learning in advancing the field of composite material damage assessment. In most of the papers studied, the AR models used are of a high order, that is, p is greater than 20. Finally, Matlab® software was the most used in the development of AR models.

Bayesian Classifier Studies

Peng *et al.* [80] proposed a probabilistic method for detecting delamination in carbon-carbon composites using Lamb wave-based characteristics. The method utilized Bayesian imaging to create a probability image of the delaminated region, and its accuracy was validated by comparing results with X-ray images.

Fendzi *et al.* [81] damage localization in anisotropic composite materials using a Bayesian framework. They developed a unique formulation to represent the direction dependence of group velocity and demonstrated its accuracy through computational and empirical testing. The approach accurately predicted the location and size of the damage, considering different degrees of anisotropy and estimating associated confidence intervals.

Cantero-Chinchilla *et al.* [82] presented an approach for identifying and locating damage in composite beam structures using ultrasonic guided waves. The technique employed a transient wave propagation model within a multilevel Bayesian framework, enabling damage detection and localization without baseline comparison or additional transformations. The method effectively reconstructed and diagnosed various types of damage in composite beams while maintaining a reasonable computational cost.

Huo *et al.* [83] introduced a novel method for composite deterioration detection using Lamb waves. Their approach combined the elliptical loci method and the RAPID algorithm in a Bayesian framework, incorporating various damage-sensitive features to enhance reliability and robustness. Numerical simulations and experimental investigations demonstrated the method's superior accuracy and dependability compared to existing approaches. Figure 2.10 shows that the proposed method can yield more accurate damage localization results compared with the existing methods.

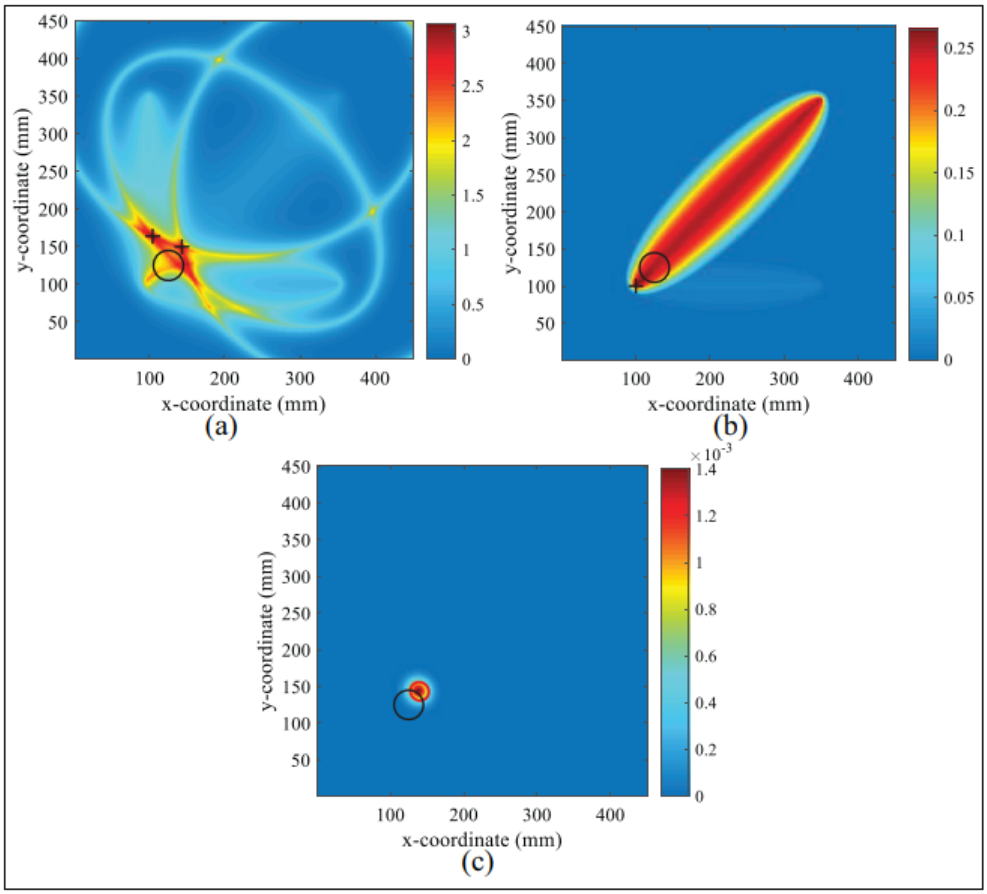

Figure 2.10: Comparisons of the damage localization results obtained using different methods: (a) the elliptical loci method, (b) the RAPID method, and (c) the proposed method (adapted from [83]).

In this subsection, the Bayesian classifiers applied in the damage assessment of composite materials were reviewed. Bayesian classifiers are a set of probabilistic techniques in

which these algorithms are based on a single principle: all classifiers assume that the value of one feature is independent of the value of any other feature, given the class variable. These articles collectively contribute to the advancement of damage detection techniques in composite materials, highlighting the use of Lamb waves and ultrasonic-guided waves. The proposed methods offer improved accuracy, reliability, and robustness in detecting and localizing damage, considering various factors such as anisotropy and uncertainty estimation.

Convolutional Neural Network Studies

Guo *et al.* [84] proposed a detection model combining a full convolution network and a gated recurrent unit for classifying ultrasonic signals from flawed 3D braided composite specimens. The study's findings show that the proposed model accurately identifies ultrasonic fault signals and outperforms six other models on the same dataset.

Nasiri *et al.* [85] developed a deep learning-based end-to-end convolutional neural network model for online monitoring of the damage advancement process of SiC_f-SiC_m composite tubes using AE data. The CNN model with single events achieves an average prediction accuracy of 84.4%, while the RF models achieve 74%. Combining several audio samples improves the accuracy of both models, with the RF accuracy reaching 82.8% and the CNN accuracy reaching 86.6%.

Tabian *et al.* [27] developed a CNN-based metamodel for impact detection and localization in complex composite structures. Piezoelectric sensors collect ultrasonic waves produced by external impact events, which are then converted into 2D images for analysis. The detection accuracy exceeded 94%, and the approach showed scalability and applicability to real-world applications. Figure 2.11 represents the confusion matrix, in which it can be observed on the main diagonal that all impacts, except one, were correctly predicted.

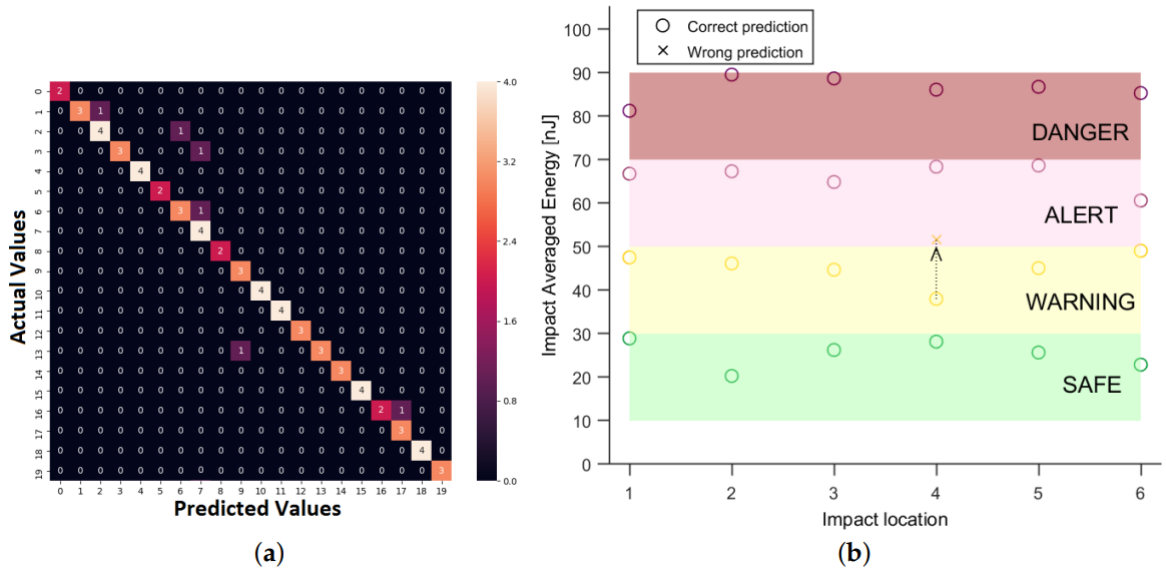

Figure 2.11: (a) The confusion matrix corresponding to run D6 in the Table 2. Each class represents a range of energy levels. (b) Energy level prediction for 6 locations, for 4 distinct energy levels. (adapted from [27]).

Salehzadeh Nobari and Aliabadi [86] developed a machine-learning technique that

utilizes voltage signals obtained from piezoelectric sensors placed on a composite panel to differentiate between hard and soft impacts.

Das *et al.* [87] proposed a framework for identifying and computing fracture parameters in thin strain-hardening cement composite cracks using a customized deep convolutional neural network, the TDCNN. To identify tiny fractures, crack parameters were derived using an image processing approach. The TDCNN demonstrated high inference capacity and resistance to uncertainty.

Saadatmorad *et al.* [88] introduced a novel technique, known as the Wavelet Transform-based Convolutional Neural Network, for detecting damage in rectangular laminated composite plates. In this method, a finite element model of the damaged RLCP is created to generate two-dimensional signals that are utilized in the wavelet transform. The proposed approach accurately predicted and identified the location of damage without requiring trial-and-error simulations.

Wu *et al.* [89] integrated a CNN with a continuous wavelet transform for detecting internal delamination in carbon fiber-reinforced plastics. The approach integrates a convolutional neural network with the continuous wavelet transform, eliminating the need for complex feature extraction and allowing for the efficient utilization of large amounts of data. The method accurately detected and located delamination damage in composite structures.

Djavadifar *et al.* [90] described a process for comparing four high-performing convolutional neural network models for detecting geometrical flaws in composites. In the best situation, wrinkle detection initially obtains a substantially lower IoU score of 0.40. The model is then assessed as a binary predictor based on per-component detection success; the model obtains a recall rate of 0.71 and an accuracy score of 0.76 (i.e., the ratio of those identified being genuinely wrinkled). Based on the data provided, this model can outperform a human operator in practice.

Augistin *et al.* [91] proposes a 3D laser scanner-based approach for the detection of inclusion on flat and curved surfaces. Using the portable laser scanner, the surfaces of each layer are scanned, and compared the resulting point clouds using reference layer data. Thicknesses between two surfaces are computed with Cloud to Cloud, Mesh to Cloud, and Hausdorff distance to enhance the visibility of inclusions. These enhanced features are used to train a multi-view convolutional neural network to mark the inclusion regions in a fast and efficient way.

Miller & Ziemiański [14] investigated the feasibility of detecting material degradation in composite structures using vibration mode shapes. A multi-layer composite cylinder was studied, with a square area of the cylinder's lateral surface designated as the material degradation zone. A CNN was employed to accurately identify the size and location of the degraded zone.

Azuara *et al.* [28] developed a technique to predict the distance-to-damage values using a convolutional neural network, which takes the received experimental data as input and transforms it into a two-dimensional picture using wavelet transform. The training process of the models resulted in an accuracy of approximately 90%, and the results obtained using the imaging method demonstrated the reliability of the whole model (CNN plus imaging algorithm) for accurate damage localization. The results for tests considering a grid size of 100 $\times$ 100 pixels (each pixel area is 9 mm2), and a σ value of 12.5 mm, are shown in Figure 2.12.

Machado *et al.* [92] proposed a machine learning approach using a convolutional neural network to automatically analyze the void content in optical microscope images. This

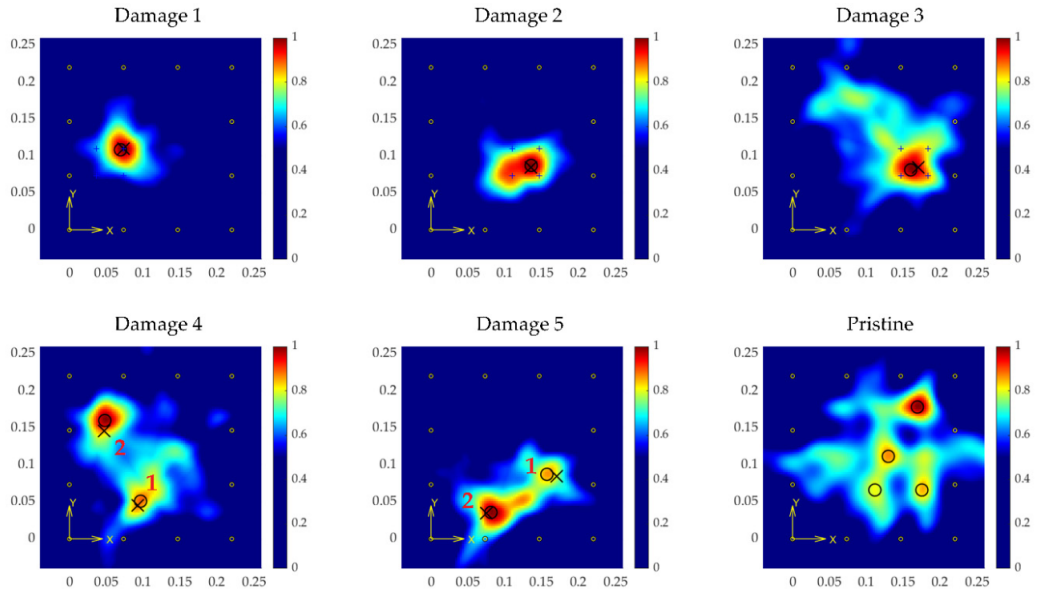

Figure 2.12: Results from the regression-based model for every test point (coordinates in m) crosses point to the actual location of the damage, and circles to the estimated locations. (adapted from [28]).

approach is designed to be robust and requires no parameter adjustment. The authors demonstrate that their approach outperforms a traditional thresholding algorithm for parsing void content from microscopy images, even across different types of laminates. While individual void statistics may show lower-than-expected accuracy, the study indicates that the proposed technique is promising.

Wang *et al.* [29] used a CNN-based image semantic segmentation method for pixel-level identification of Digital Image Correlation strain field images. The training dataset is generated through finite element simulation and validated by the model. The trained CNN model showed high accuracy for strain field segmentation.

Cui *et al.* [93] developed an ultrasonic-guided wave approach using the most sensitive wave characteristics selected by the learned training data to detect and locate structural degradation in a stiffened composite panel. The results demonstrated the technique's ability to detect damage in critical areas of the stiffened composite test panel, including the skin region, stringer flange region, and stringer cap region.

Yang *et al.* [94] proposed a novel approach combining CNN and algebraic reconstruction techniques for ultrasound tomographic imaging of composites. The proposed method uses blurred ART images as inputs to a CNN with an encoder-decoder architecture, which segments the images using convolution and max-pooling to retrieve defect-modulated image characteristics. The approach accurately detected anomalies and delamination, even with limited sensing capabilities.

Helwing *et al.* [95] analyzed the damage evolution of GFRP composites using in situ x-ray CT analysis and a CNN-based fault segmentation approach, improving defect detection quality and sensitivity. Detailed characteristic values for the damage behavior of GFRP at different stiffness decreases are obtained by selectively identifying faults according to the underlying damage mechanism. This results in a mechanism-differentiated quantification of damage progression as stiffness decreases.

Barile *et al.* [2] trained a deep convolutional network for image-based acoustic emission

waveform classification. Spectrograms of AE Waveforms from four distinct damage types, matrix cracking, delamination, debonding, and fiber breaking, were acquired in Mel scale and utilized as training and test data for the CNN. The CNN's overall prediction accuracy is 97.9%, whereas fiber breakage and delamination events may be predicted with 100% accuracy.

CNNs are a class of artificial neural networks, most commonly applied to analyze 2D signal images but also used in 1D signals. In this subsection, studies that use convolutional neural networks for damage assessment of composite materials are reviewed. In the reviewed studies, a lot of convolutional networks used defined architectures (like U-net, Mask R-CNN, Deeplab V3+, IC-net, and others) as well as networks built part by part, that is, inserting each layer in the desired sequence. CNNs have a high data-driven learning capacity and thus perform well in most problems. In general, most of the studied papers used the Python programming language in their development.

K-Means and K-Nearest Neighbors Studies

Barile *et al.* [96] investigated damage characteristics in CFRP composites using acoustic emission. They used Laplacian scores to identify appropriate AE data features and employed k-means clustering to establish their relationship. They found a strong correlation between AE signal amplitude and frequency centroid (C-Freq) for characterizing damage modes. This technique enables a comprehensive understanding of the damage modes in CFRP composites using AE analysis.

Pashmforoush *et al.* [97] developed a method for monitoring delamination in sandwich composites using AE signals. They combined k-means clustering with the genetic algorithm to categorize damage processes and identify distinct failure scenarios. The researchers validated their results through SEM observation and concluded that their approach effectively classifies damage in sandwich composites.

Xu *et al.* [98] investigated the behavior of a 59.5-meter-long composite wind turbine blade under accelerated fatigue stresses using an acoustic emission approach. They analyzed AE signal components through spectrum analysis and used a time-difference method for detecting and locating defect sources. They applied k-means clustering to identify distinct damage types. The approach was successful in detecting and characterizing defects in composite blades.

Shrifan *et al.* [99] developed a microwave-based non-destructive testing approach using the k-means algorithm for defect identification in GFRP composites. They utilized an open-ended rectangular waveguide and mean measurements to reduce the effect of permittivity changes. Unsupervised machine learning with k-means clustering successfully detected defects as small as 1 mm.

Ech-Choudany *et al.* [100] proposed an incremental clustering and k-means approach for analyzing AE data in glass fiber-reinforced composites. IC identified information-carrying signals and determined damage mechanisms without additional knowledge. The strong performance of the supervised method, as indicated by AUC values greater than 0.9 for each damage type, validated the reliability of the generated learning database. Figure 2.13 shows the results obtained by using 4 clusters.

Zeng *et al.* [101] proposed a real-time health monitoring approach for 2D C/SiC composites. They employed unsupervised recognition (k-means++) for the spectrum properties of AE signals and supervised identification for damage identification. The study identified primary damage mechanisms and examined damage evolution using AE energy accumulation curves. The proposed approach showed improved sensitivity and

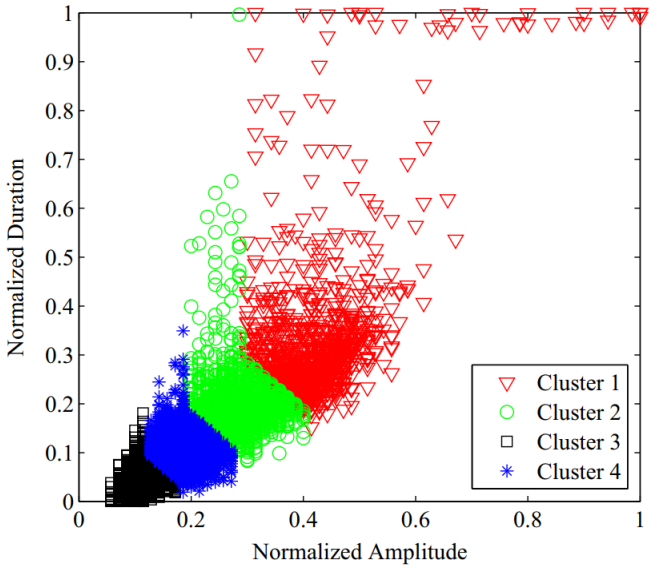

Figure 2.13: Projection of UD0 composite clustering for 4 clusters obtained by the k-means method (adapted from [100]).

accuracy compared to previous studies. Figure 2.14 shows that the method can effectively identify the damage modes.

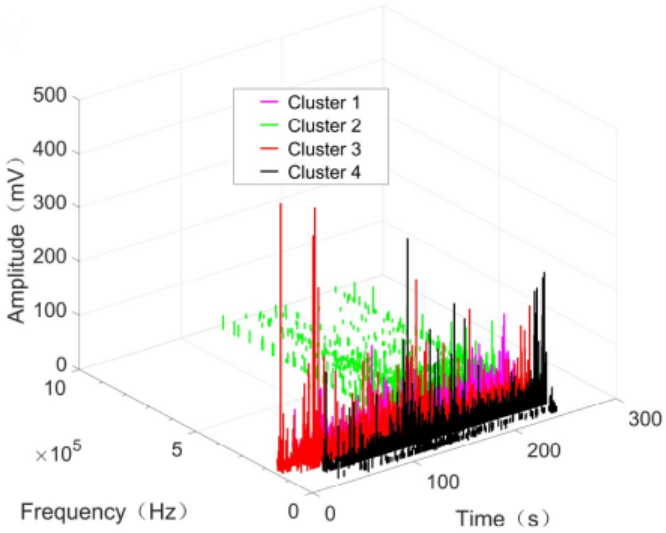

Figure 2.14: Spectral characteristics distribution of 2D C/SiC at ambient temperature related to time (adapted from [101]).

Essasi *et al.* [102] discussed the behavior of an eco-sandwich composite with an auxetic core. Different configurations were explored, and damage behavior was monitored using AE. The k-means method was used for categorization, revealing core cracking, matrix cracking, and fiber/matrix debonding as the main occurrences for each configuration.

This subsection reviewed papers that use the KNN and K-means algorithms. Despite their names, the two algorithms have significant differences, with K-means being an unsupervised ML method and KNN being a supervised method. Therefore, K-means presents lower performance compared to KNN, but it has the advantage of being capable

of anomaly detection. In general, most studies used both methods together with acoustic emission signals, and some studies combined clustering algorithms with other methods like genetic algorithms or time-difference methods for enhanced analysis.

Principal Component Analysis Studies

Taghizadeh & Ahmadi [103] investigated delamination in ultra-high molecular weight polypropylene/epoxy composites with various topologies using acoustic emission signal analysis. They performed tensile tests and Mode I delamination on epoxy resin, UHMWPP fiber bundles, and UHMWPP/epoxy specimens and managed to identify damage modes, including matrix cracking, fiber-matrix debonding, fiber breakage, and fiber pull-out using principal component analysis.

Rao *et al.* [104] proposed a diagnostic technique based on frequency response functions and principal components to detect delamination in laminated composites. Finite element models of laminated composite beams and plates were used to produce vibration data for healthy and damaged structures. Their method can identify the instant of damage, spatial location, amount of delamination, and matrix cracking.

Sierra-Pérez *et al.* [105] developed a method using fiber Bragg gratings as strain sensors and principal component analysis to detect damage in composite structures. The proposed methodology was tested on a 1.5-meter-long composite unmanned aerial vehicle wing piece, and it was able to identify variations between the baseline and different damage scenarios.

Yan *et al.* [106] introduced a stable principal component pursuit strategy combined with a moving-window strategy for analyzing thermographic data. Their method effectively extracts background information, reduces noise, and identifies defects in tested specimens.

Mohamad *et al.* [107] proposed a damage classification method for natural fiber-reinforced composites using signal processing parameters and principal component analysis. They analyzed strain data from an impact event and observed that the network could learn and classify the size of damage in the panel. The combination of features retained about 84.5% of the variance. Figure 2.15 shows the results for five impact severity classes.

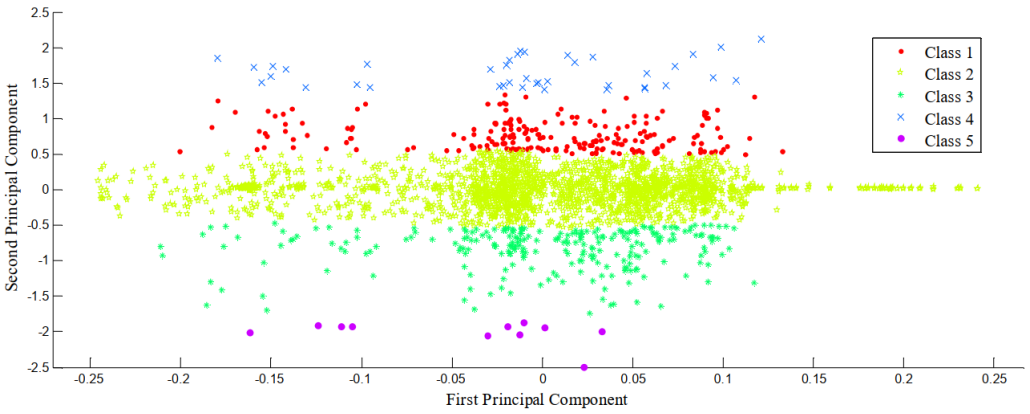

Figure 2.15: PCA plot for the combination of all time-domain features (adapted from [107]).

Lu *et al.* [108] developed a damage detection method using fiber Bragg grating sensors and principal component analysis in carbon fiber reinforced polymer structures. They first

excited the undamaged carbon fiber-reinforced polymer structure and measured its dynamic response signal. The frequency response was extracted using the Fourier transform method as the damage feature, which was then reduced in dimension using PCA. Their approach accurately detects structural damage using only undamaged state samples.

Malinowski *et al.* [109] explored the use of electromechanical impedance and principal component analysis for damage detection in glass fiber-reinforced polymer composites. They investigated a beam and a plate with simulated delamination damage. Their data processing tool utilizing PCA showed promise in managing sensor network data, differentiating between damage scenarios, and detecting damage with missing data.

Lu *et al.* [110] proposed a method for assessing damage in carbon fiber-reinforced polymer laminates using Synchrosqueezed Wavelet Transform and ensemble Principal Component Analysis. They developed an approach for extracting damaged features based on Synchrosqueezed Wavelet Transform and Singular Spectrum Analysis to reduce feature dimension and successfully extract damaged features. Their approach effectively extracted damaged features and assessed damage in the presence of noise interference and limited training samples.

All the studies reviewed in this subsection show that PCA is a technique that is extremely useful for dealing with large datasets, but as a disadvantage, the feature visualization is impaired when the problem features many classes. It was also possible to notice that the PCA was used in conjunction with several sensing techniques (impact testing, vibration, AE signals, thermography, strain, lamb waves, and EMI). Although PCA has a lower accuracy than the other techniques, it has the advantage of not requiring knowledge of the defect, only the healthy state.

Support Vector Machines Studies

Fredo *et al.* [111] developed a method for classifying damages in composite materials using photographs taken from the front and back sides of the materials after impingement of different sizes. They utilized anisotropic diffusion filtering and Fuzzy C-Means clustering for segmentation. Geometrical characteristics and Zernike Moments were used as features, and a Support Vector Machine classifier was employed. Zernike Moments performed better in both global and local damage classification.

Forero-Ramírez *et al.* [112] . investigated the effectiveness of Support Vector Machines in detecting internal defects using thermal contrast information obtained from the Background Thermal Compensation by Filtering method. They examined a 20×20 cm CFRP slab with 25 square Teflon insertions to simulate flaws, and IR images were captured using Active Pulsed Thermography equipment under two different conditions. They achieved higher sensitivity in flaw detection by combining the Background Thermal Compensation by Filtering contrast method with SVM.

Shyamala *et al.* [113] used Support Vector Machines to detect damage in composites. The algorithm locates the damage and evaluates its severity based on changes in dynamic responses. The results demonstrate that the proposed algorithm effectively detects a wide range of damage scenarios.

Gillespie *et al.* [114] studied the impact of delaminations on the transient heat conduction profile of carbon fiber-reinforced polymer laminates. They employed a supervised Support Vector Classification method to detect delaminations using temperature data collected from either the perimeter or the center of the defect during a 140-second ramping heating session up to 80 degrees Celsius. The findings show high accuracy in classifying delaminations or no delamination. Figure 2.16 shows the results for a studied sample.

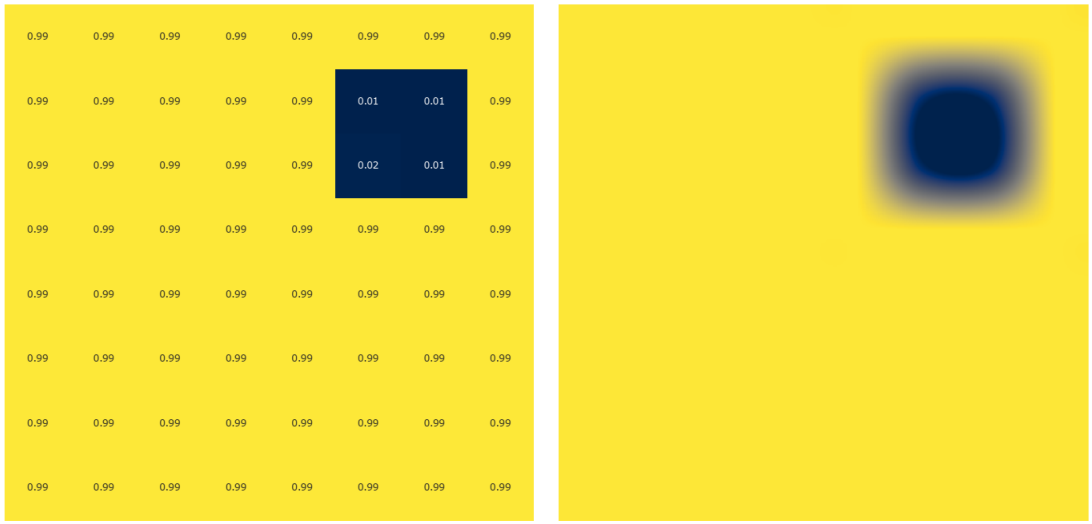

Figure 2.16: Display of overall percentage score (0–1) of the 140 time intervals for each RTD probes which classified as 'No Delamination' (a) Corresponding RTD probe locations, (b) Gaussian filter application to present images similar to traditional IR thermography methods (adapted from [114]).

Yue *et al.* [115] developed a constitutive model for plastic damage in steel fiber reinforced concrete. They conducted three-point bending tests on 27 concrete specimens with varying fiber volume fractions and concrete matrix strengths and monitored the acoustic emissions during fracture to analyze the released strain energy in the fracture process zone. They used SVM to classify acoustic emission data into tension-crack mode and shear-crack mode and established correlations between fiber volume fraction, characteristic length, and damage variables.

Xu *et al.* [116] proposed a method for determining the degree of damage in carbon fiber-reinforced polymer cables using a PSO-SVM algorithm based on nine parameters of acoustic emission signals. Acoustic emission signals were analyzed, and the trained support vector machine accurately predicted the damage degree. These findings indicate that acoustic emission combined with machine learning is a feasible approach to determining the damage degree in carbon fiber-reinforced polymer cables.

Sheng *et al.* [117] presented a novel approach for categorizing physical damage in carbon fiber-reinforced polymer. using AdaBoost and Support Vector Machine. The experimental results revealed that the modified AdaBoost methods with distance-based weighted least square support vector machine and filter factor performed better than traditional algorithms. The authors also discussed the impact of the new weighted update technique and filter factor on the algorithm.

Rajiv *et al.* [118] employed a multi-support vector machine for durability and damage classification of composite materials using filtered images. Experimental validation on various composite materials was conducted using real-time images, and the results demonstrate that the proposed approach achieves higher accuracy in image classification than other models. Additionally, the longevity of the material is assessed based on the material removal rate, wear resistance rate, and material strength.

Alhammad *et al.* [119] used pulsed thermography and machine learning for the automated detection of damage in composite materials. The classification findings varied

from 78.7% to 93.5%, opening the way for the development of an automated model to efficiently evaluate the damage to composite materials using the Non-Destructive Testing approach.

Support vector machines are non-probabilistic binary linear classifiers used to perform classifications and regressions. In this subsection, the analyzed studies generally combine SVM with mechanical failure tests, such as the three-point flexion test, cumulative energy test, fatigue test, and others. The SVM has a great advantage in analyzing complex datasets; however, if this dataset is very large, there may be a high computational cost.

Miscellaneous

This subsection provides a review of the machine learning frameworks that are developed from a combination of basic machine learning tools. These combinations occur mainly to combine the positive points of each technique and/or to supply any deficiency that some techniques have by incorporating a new one.

Pashmforoush *et al.* [120] explored acoustic emission monitoring to identify and categorize damage modes in glass/polyester composites. They used PCA and k-means algorithms to cluster acoustic data, successfully classifying three distinct damage processes.

Selva *et al.* [121] developed a system using electromechanical impedance technology for monitoring carbon fiber-reinforced plates. To simulate damage, numerical simulations based on finite element analysis are used. The input data for the ANNs are obtained from a principal component analysis of the damage measurements, and the ANN is shown to accurately predict the location of a single damaged patch in laminated composite plates.

Crivelli *et al.* [122] proposed a neural network-based approach for classifying acoustic emission signals during glass-fiber tensile testing. They trained a self-organizing map and used k-means clustering to accurately categorize specimens with different material layups and recognize signals from notched specimens. These findings suggest the potential of the proposed method for real-world structural health monitoring applications.

Mardanshahi *et al.* [123] developed a guided wave propagation-based method for detecting and classifying matrix cracking in composites. Glass/epoxy cross-ply laminated composites were fabricated, and matrix cracking of different densities was induced in 90° layers. Linear discriminant analysis was used to reduce the dimensions of the data, and support vector machines, linear vector quantization ANN, and MLP ANN were employed for classification. The results showed that SVM had the highest accuracy rate (91.7%), followed by linear vector quantization ANN (88.9%) and MLP ANN (77.8%). Figure 2.17 shows the estimation of the parameters of SCD damage obtained from the NN regression fitting on the validation experimental data in comparison with the actual values.

Chen *et al.* [124] compared the effectiveness of an artificial neural network (ANN) and a convolutional neural network in detecting defects in fiber-reinforced composite materials. They used micro-CT scanning and the binarized statistical image features approach, finding that CNNs outperformed ANNs in defect prediction.

Hamdi *et al.* [125] investigated compression damage in CFRP composites with different resins. They used CLC experiments and combined DIC, AE, and in-situ microscopy to track damage progression. K-means, KNN, and PCA clustering of AE signals identified primary clusters related to potential damage situations. The approach helped identify the onset of severe damage. Figure 2.18 shows acoustic activity in terms of Absolute Energy during CLC testing.

Dziendzikowski *et al.* [126] presented a method for impact damage detection in composite structures using PZT sensors and a Bayesian technique for data categorization. The

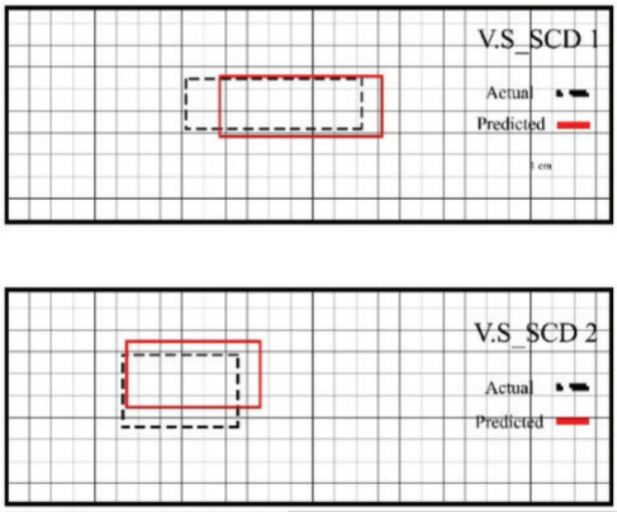

Figure 2.17: Estimation of the parameters of SCD damage obtained from the NN regression fitting on the validation experimental data in comparison with the actual values (adapted from [123]).

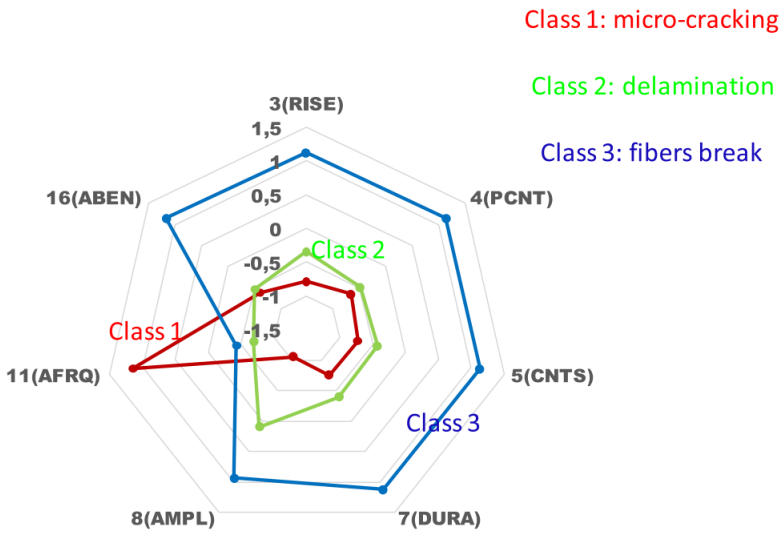

Figure 2.18: Normalized values radar chart for the R8 composites for each class and in terms of: CNTS = counts, AMPL = Amplitude, AFRQ = average frequency, PCNT = counts to peak, RISE = Risetime, DURA = Duration, ABEN = Absolute Energy.Class 1 (labeled as noise & matrix micro-cracking), Class 2 (labeled as delamination), and Class 3 (labeled as fibers break) (adapted from [125]).

method can differentiate between pathways responsive to the transmission mode of elastic wave interaction and those sensitive to the reflection mode. The proposed method showed better performance in detecting damage pathways and produced fewer false-positive indications compared to the KNN algorithm.

Scholz *et al.* [127] proposed a method for detecting and locating damage in composite rotors based on structural vibration analysis. They created a database of 720 simulated test cases in various damage conditions to generate several data sets and then used it to train a fully connected neural network and a CNN. They evaluated the trained models using k-fold cross-validation and measured their sensitivity, specificity, and accuracy. The convolutional neural networks showed considerably better performance, achieving up to 99.3% accuracy in damage localization and quantification.

Lee *et al.* [128] developed a system for monitoring the health of CFRP structures using electromechanical properties. They employed a non-destructive self-sensing approach and utilized k-means clustering and principal component analysis for damage identification. The system successfully detected various forms of damage in composite structures using only electromechanical activity.

2.4 Future Research Directions

Machine learning techniques are increasingly present in the damage assessment of composite structures. However, there are still several challenges and constraints for a full application of these techniques, and some of them will be discussed below:

- Noise signal: In industrial applications, an environment with a high level of noise is normally encountered. As most work is done on simulated data or in a controlled environment, it is hard to guarantee that the algorithms will perform well in industrial environments.

- Unbalanced data: In real applications, it is expected to have a greater amount of data in the healthy condition than in the defect condition, which can affect the training process and consequently the accuracy of ML algorithms.

- Generalization: Because most ML algorithms are purely data-oriented, they can work well for similar data sets; however, considering generalization, it still takes a long time for the algorithms to reach a reasonable behavior. Therefore, it is necessary to implement other training approaches that are not faithfully data-based.

- Interpretability: Although some methods already have some way of visualizing internal mechanisms, known as feature visualization and/or coarse localization maps, it is still not possible to associate this with physical phenomena. Being able to associate these internal controls with physical laws can help both in the interpretation of ML methods and in generalization.

ML approaches are still under development, requiring a larger refinement of the techniques, in general, to be fully applied to most real-world issues. Some recent studies evaluate the use of physics-informed neural networks (PINNs) to increase robustness and generalization; however, most studies are still in the early stages of development.

2.5 Chapter Conclusion

The use of composite structures is becoming increasingly frequent and in a greater number of applications, which demands a greater concern with the reliability of these materials. Consequently, this work reviewed the ML methods applied for damage assessment of composite structures, classifying them according to the type of ML technique used.

Despite the fact that there are numerous machine learning-based techniques, it is challenging to identify one that has high damage sensitivity, robustness, portability, and strong anti-interference properties due to the variety of structural forms, significant variations in service environments, damage types, sensor networks, and sensing signals. For instance, a regression or classification approach would work better with an AE methodology than an object recognition method. An object recognition tool, such as a CNN, would be advantageous for scanning methods like thermography. Therefore, it is extremely important to know the physics of the problem in order to choose the best method.

Another point is that most studies use either simulated data or test specimens, with few studies using real structures. In addition, as expected, studies that use real structures have lower accuracy compared to other types of studies. Therefore, the next step would be to implement ML techniques in real environments to improve their effectiveness and robustness. Also, with the review of the articles, it was noticed that the main programming languages used were Matlab® (mainly for ANN) and Python (mainly for CNN).

In addition, supervised learning methods showed the best results for damage detection tasks and consequently are the most used learning paradigm. Furthermore, important present challenges and constraints are discussed, providing research insights into the most recent ML approaches. The following is a summary of the reviewed articles:

- This study observed that publications became more frequent from 2019 forward.
- ANN, CNN, and PCA were the most commonly used techniques, accounting for nearly 62% of all studies. Selecting the most recent studies (from 2019 onwards), this dominance is even greater.
- To perform the training, the favorite inputs were acoustic emission, vibration, guided waves (lamb and ultrasonic), and signal images (thermal, strain, and time-frequency maps).
- In general, ML techniques do not require a large data set to reach a reasonable level of accuracy, making most of the algorithms have a low computational cost.
- ML models are still “black boxes”. Thus, future studies that allow the incorporation of physical laws in the models, thus increasing the interpretability and generalization of the methods, are very promising.

3 Damage Detection and Localization in Composite Sandwich Panels

In this chapter, a methodology that combines mode shapes and CNNs to identify, identify, and localize damage within sandwich panels is proposed. The methodology is validated using a finite element model with parameterized 2D (skin and interface) and 3D (core) damage. The results demonstrate that the proposed method achieves an accuracy of nearly 100% for undamaged and core damage conditions, and approximately 80% for skin and interface damage conditions. Additionally, the damage localization network exhibited an average MAE of 10-12 mm, corresponding to an error margin of 4-5%. Despite the high accuracy in identifying the position of the damage, the model faced challenges in accurately predicting other damage parameters such as orientation and size due to the high complexity of the problem.

The chapter is organized as follows: Section 3.1 presents the fundamental concepts of sandwich panels and convolutional neural networks. Section 3.2 presents the methodology adopted, from FEM modeling to aspects of the CNN adopted. Section 3.3 presents the main results for detection and damage localization. Finally, Section 3.4 concludes the chapter.

3.1 Theoretical background

3.1.1 Sandwich Panels

Sandwich composite structures constitute a specialized class of engineered materials designed to achieve high structural efficiency through an optimal balance between stiffness, strength, and weight. Owing to their outstanding stiffness-to-weight and strength-to-weight ratios, sandwich panels have been extensively adopted in aerospace, automotive, marine, civil, and renewable energy applications [129, 130]. A typical sandwich panel consists of two stiff and strong face sheets bonded to a lightweight core. In this configuration, the face sheets primarily resist in-plane and bending loads, while the core provides shear resistance, increases bending stiffness, and stabilizes the structure against buckling.

The core is generally manufactured from lightweight and rigid materials such as expanded polystyrene, polyurethane foam, aluminum honeycomb, or polymeric honeycomb structures. The face sheets are commonly made of high-strength materials, including aluminum, steel, glass fiber–reinforced polymers (GFRP), or carbon fiber–reinforced polymers (CFRP). This synergistic combination allows sandwich panels to deliver superior mechanical performance while maintaining low mass, making them particularly attractive for weight-sensitive and safety-critical structures.

In some structural configurations, particularly in thin or highly optimized designs, multilayer laminated composites without a distinct lightweight core are also employed. In such cases, the stacking sequence and fiber orientation play a crucial role in tailoring the stiffness, strength, and dynamic behavior of the structure. Quasi-isotropic layups, such as $[0/90/\pm 45]$, are often adopted to approximate isotropic behavior, whereas directional

layups are designed to maximize stiffness along preferred load paths [131]. These design choices significantly influence the mechanical response and vibration characteristics of the structure.

Despite their advantages, sandwich composite panels are susceptible to a wide range of damage mechanisms, which may occur in three primary regions: the face sheets (skins), the core, and the skin–core interface. Typical damage modes include matrix cracking, fiber breakage, interlaminar delamination, skin–core debonding, core shear failure, core crushing, porosity, and fiber misalignment. These defects may arise during manufacturing or develop during service as a result of impacts, cyclic loading, environmental exposure, or improper bonding [11, 132]. Many of these damage mechanisms are internal and may remain visually undetectable, particularly in the case of Barely Visible Impact Damage (BVID), where severe subsurface delamination can occur with minimal surface indication.

Among the most critical failure modes affecting sandwich panels is delamination, characterized by the separation of layers due to inadequate bonding, impact events, or excessive mechanical stress. Moisture ingress represents another major concern, as it may penetrate through surface damage or sealing failures, leading to core degradation, corrosion, and a reduction in structural stiffness and strength. Furthermore, excessive static or dynamic loading can induce core crushing or shear deformation, impairing the panel's ability to efficiently transfer loads and potentially resulting in catastrophic structural failure. Representative examples of these damage mechanisms observed in real composite sandwich structures are presented in Figure 3.1.

The detection and localization of damage in sandwich composite panels pose significant challenges, particularly due to the internal nature of many defects and the limited effectiveness of visual inspection. Conventional Non-Destructive Evaluation (NDE) techniques, such as ultrasonic testing, thermography, and X-ray inspection, often require localized access, specialized equipment, and offline inspection procedures. These constraints can increase inspection time, operational costs, and system downtime, limiting their applicability for continuous or in-service monitoring.

As a result, vibration-based approaches have gained increasing attention as complementary strategies for Structural Health Monitoring (SHM) of sandwich composite structures. Structural damage typically induces local stiffness degradation, which alters the dynamic characteristics of the structure, including natural frequencies, damping ratios, and, most notably, mode shapes [133]. Mode shapes provide spatially distributed information and are particularly sensitive to localized damage, making them a valuable source of data for damage localization. However, the high dimensionality and complexity of modal data in composite structures present challenges for traditional feature-based analysis methods.

These limitations have motivated the development of advanced data-driven and intelligent SHM frameworks that integrate vibration-based information with modern computational tools. In particular, artificial intelligence–based methods offer significant potential to enhance damage detection, localization, and characterization in sandwich composite panels by exploiting complex patterns in high-dimensional datasets. The inherent complexity of damage evolution in laminated and sandwich composites underscores the necessity of such advanced monitoring strategies to complement conventional inspection techniques and improve diagnostic reliability.

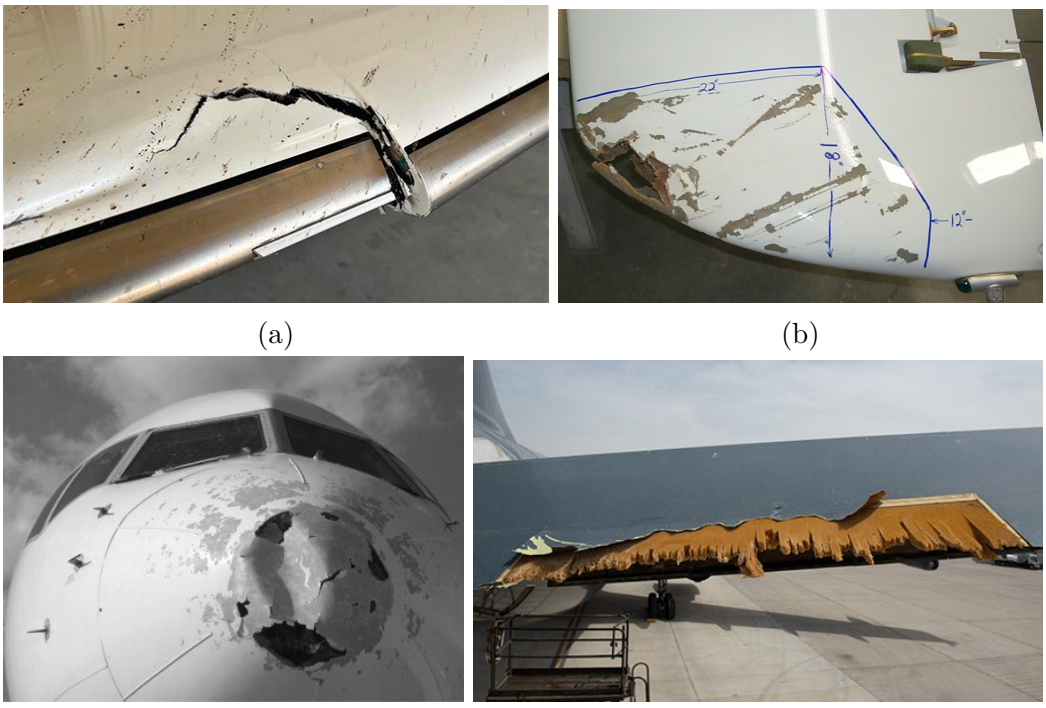

(a) (b)

(c) (d)

Figure 3.1: Several failure types in sandwich composites.

3.2 Methodology

In this section, the methodology adopted for simulating and analyzing the behavior of sandwich panels under various conditions is presented. The methodology encompasses the finite element modeling of sandwich panels and damage, the generation of contour plots from modal analysis data, and the implementation of Convolutional Neural Networks (CNNs) for detection and damage localization tasks (regression). Furthermore, Figure 3.2 presents a flowchart illustrating the sequence of steps. The following subsections will cover more detailed information on each part of the process.

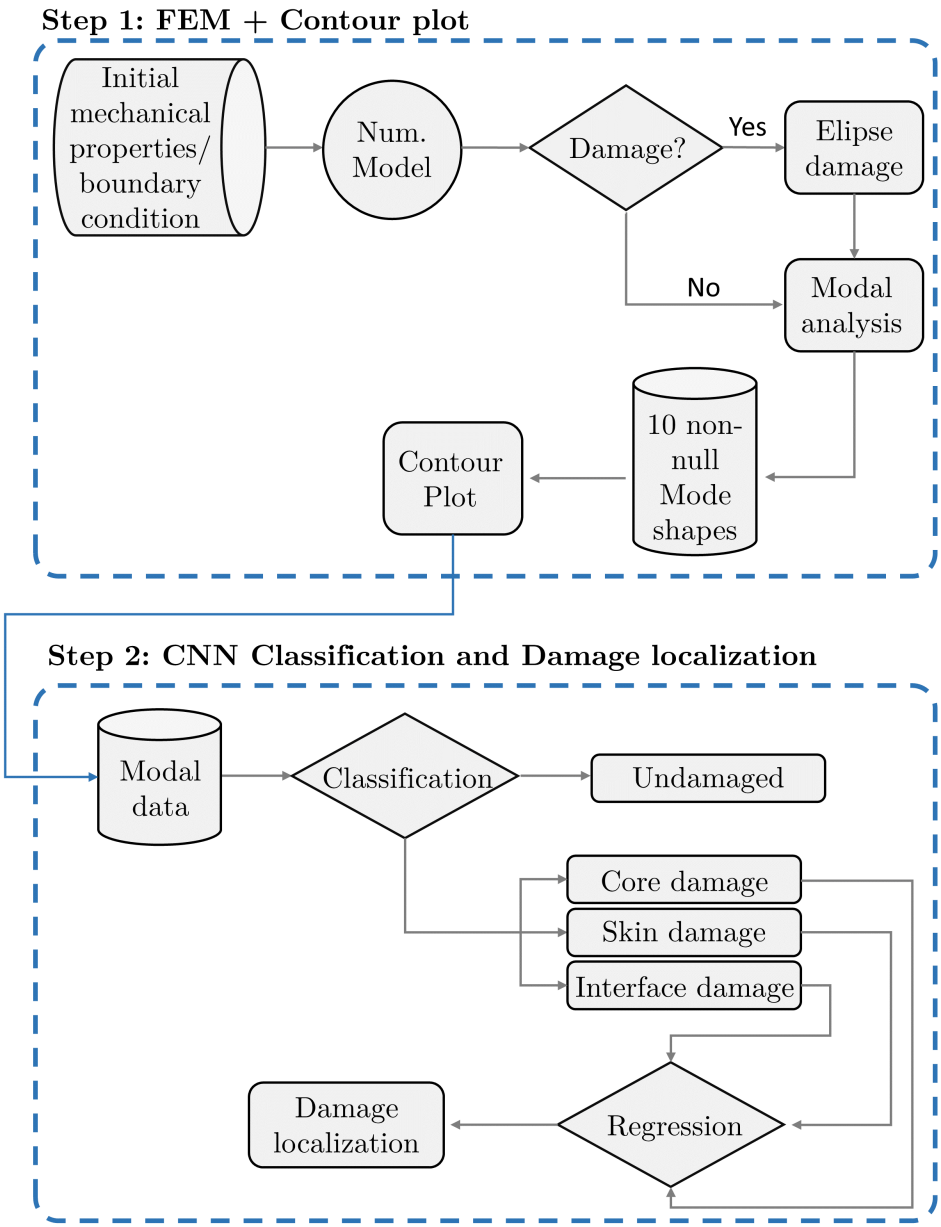

Figure 3.2: General flowchart for damage detection and localization.

3.2.1 Finite Element Model

The sandwich panel was simulated using the finite element method (FEM) in Ansys® Parametric Design Language (APDL). This software is well-known for its ability to accurately replicate the conditions of the proposed test through parametric simulations.

Afterward, four distinct models were developed for each condition: one representing the pristine state without any damage, and the remaining three simulating damage in different areas, including the core (3D damage), the skin (2D damage), and the interface (2D damage).

All models were constructed uniformly, utilizing the same type of elements throughout. The core was represented using 3D elements with 8 nodes and 3 degrees of freedom each (*solid185*), while the skin was modeled with 2D elements featuring 8 nodes and six degrees of freedom per node (*shell181*).

Moreover, the test is a modal analysis aimed at capturing the first 10 non-null mode shapes of the sandwich panel for each scenario (no damage, core damage, skin damage, and interface damage). Furthermore, four distinct tests were carried out: one with the panel completely unconstrained (FFFF), another with one side clamped while the remaining three sides were free (CFFF), a third with two opposite sides clamped and the other two sides free (CCFF), and finally, one with all four sides clamped (CCCC).

To further approximate real-world conditions, mechanical properties varied for each simulation. This variation was carefully adjusted to simulate glass fiber-reinforced polymer (GFRP) sandwich panel variations. Table 3.1 outlines this variation.

The simulation routines used Python with the PyAnsys library, particularly the Pymapdl module [134]. PyAnsys facilitates seamless interaction with Ansys® through Python, allowing for the automation of simulation tasks, analysis of results, and integration with diverse Python tools and libraries. 1250 simulations were executed for each boundary condition and scenario, ensuring a necessary amount for AI models.

Table 3.1: Lower and Upper bounds of mechanical properties.

Core		
Parameter	**Lower Bound**	**Upper Bound**
E [MPa]	110	120
ρ_{core} [kg/m^3]	70	80
Skin		
Parameter	**Lower Bound**	**Upper Bound**
$E_1 = E_2$ [GPa]	17	19
E_3 [GPa]	26	29
G_{12} [GPa]	5.7	6.3
ρ_{skin} [kg/m^3]	1600	1700

Undamaged model

The Undamaged model, which serves as the foundation for the subsequent damaged models, consists of a 250 × 250 mm^2 plate structure. The skins comprise four plates oriented either at 0° or 90° with a thickness of 0.33 mm each, while the core has a thickness of 15 mm. Alongside the properties selected for variation, certain properties were held constant, which is ν at 0.2 and ν_{12} at 0.2. Meshing was carefully executed to ensure result accuracy while avoiding unnecessary computational burden. Figure 3.3 shows the numerical model of the sandwich panel in finite elements.

Skin and Interface damage

The model that represents the Skin and Interface damage is derived from the Undamaged model by incorporating a 2D ellipse onto one layer to represent the damage. This ellipse is implemented by modifying the material's elastic properties, specifically reducing the skin's E_1, E_2, and G_{12} properties by 99%. Skin damage is identified when the ellipse appears in the first three layers, whereas if it appears in the fourth layer, it is identified as interface damage. Moreover, damage can be in the upper or lower plies, concerning the core.

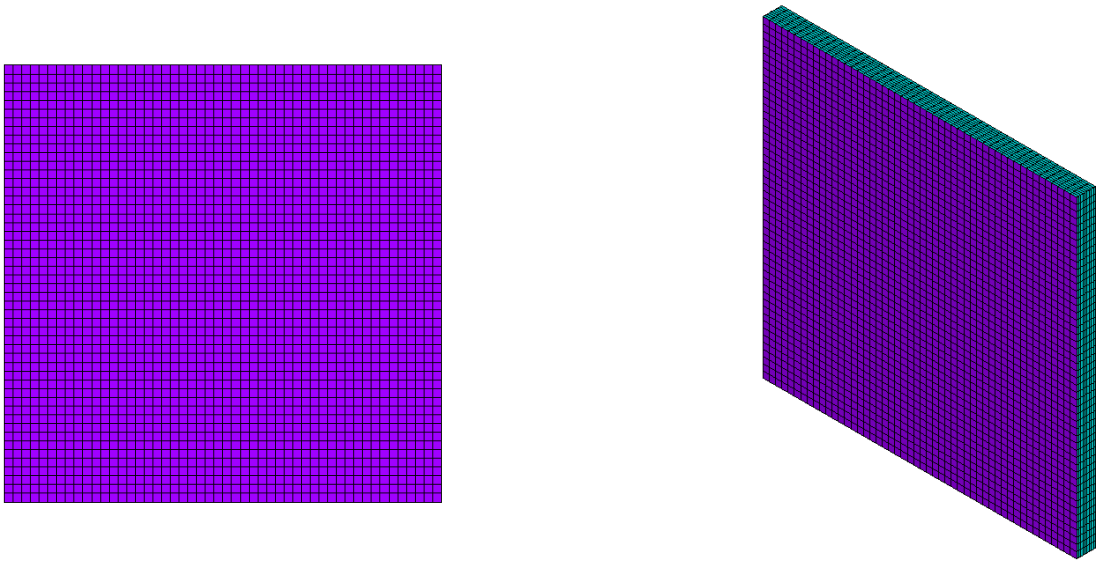

(a) (b)

Figure 3.3: Numerical model in finite elements: (a) front view, (b) isometric view.

The ellipse is parameterized with five variables (Figure 3.4), and Table 3.2 outlines the lower and upper bounds of each variable. These values were chosen randomly for each simulation.

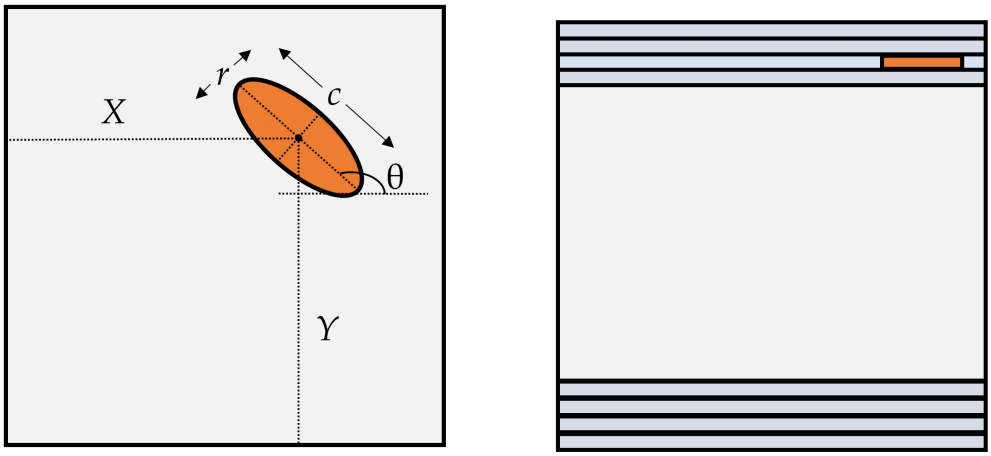

(a) (b)

Figure 3.4: Skin/Interface parameterized damage: (a) top view, (b) side view.

Core damage

The core damage model is derived from the undamaged model by introducing a 3D ellipse into the core to symbolize the damage. Similar to the skin and interface damage, this ellipse is parameterized with five variables and reduces the elastic property E by 99%. However, property reduction occurs over a specific height within the core in this

Table 3.2: Lower and Upper bounds of mechanical properties.

Parameter	Lower Bound	Upper Bound
X [mm]	0.05	0.20
Y [mm]	0.05	0.20
θ [°]	0	180
c [mm]	0.05	0.08
r [mm/mm]	0.2	0.6

case. The severity of the damage is categorized into three levels, determining the height of the ellipse: 2 mm, 5 mm, and 8 mm, as shown in Figure 3.5.

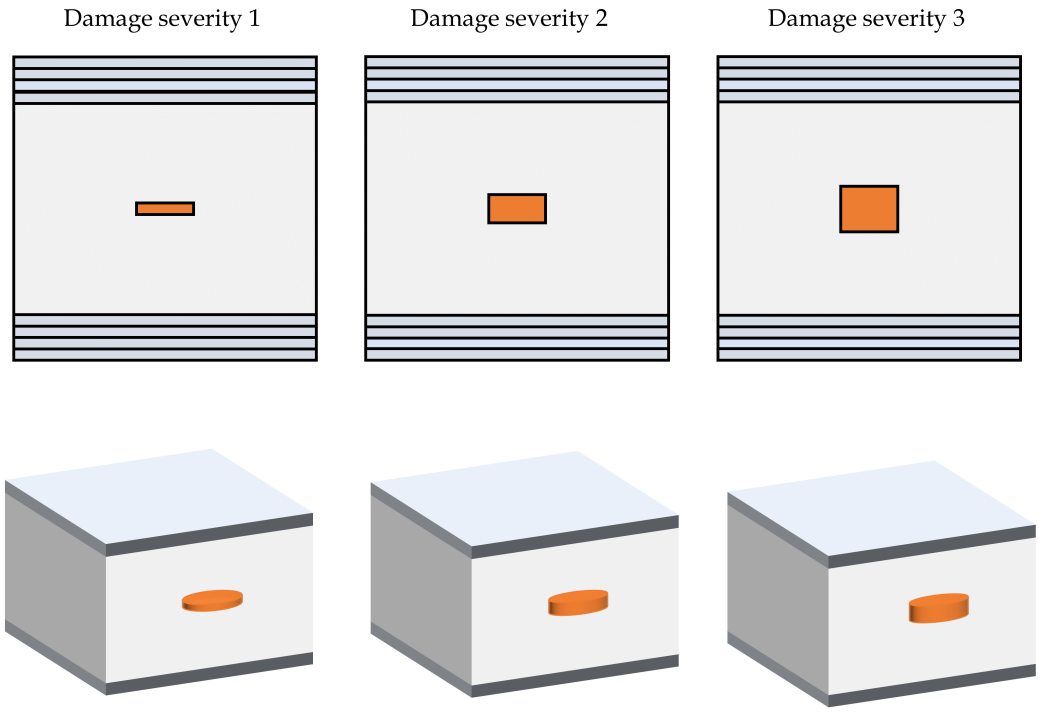

Figure 3.5: Height Core damage: Side view and 3D view.

Mesh Convergence

Mesh convergence is the process of refining the mesh until the variations in the natural frequency become insignificant as the number of elements increases. Achieving mesh convergence is crucial to ensure that the numerical solutions are as accurate as possible. Figure 3.6 illustrates the mesh convergence for the three models (considering an arbitrary damage condition) developed at the FFFF boundary condition. The graph indicates that beyond 12,500 elements, the results stabilize and remain constant. Therefore, using 12,500 elements is sufficient to guarantee the accuracy of the results without incurring additional computational costs.

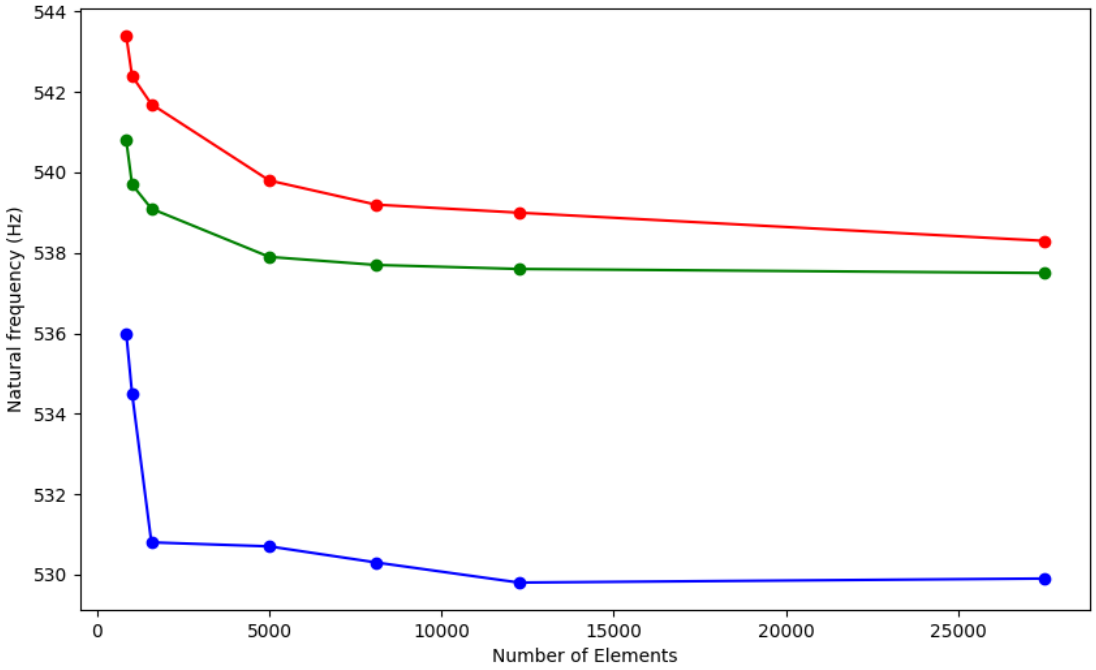

Figure 3.6: Mesh Convergence: • Undamaged, • Skin/Interface Damage, • Core Damage.

3.2.2 Contour Plot

The modal tests provided displacement data (x, y, z) at each node. However, for CNNs, which are more adept at processing image data, contour plots to transform the information of each mode shape into images are generated. A contour plot offers a graphical representation of a 3D surface on a 2D plane, with contours depicting lines of constant value representing the surface levels. To create these images, the node positions (x, y) and the vector sum of displacements (x, y, z) on the upper face of the sandwich panel are utilized. Table 3.3 presents the first 10 non-null mode shapes for the Undamaged condition of all boundary conditions.

Table 3.3: First 10 non-null mode shapes for the Undamaged condition of all boundary conditions.

Boundary Condition	Mode 1	Mode 2	Mode 3	Mode 4	Mode 5	Mode 6	Mode 7	Mode 8	Mode 9	Mode 10
FFFF	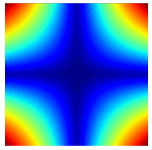	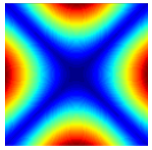	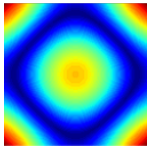	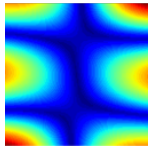	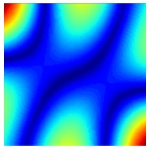	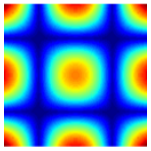	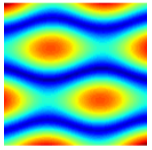	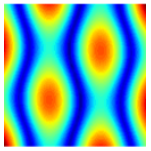	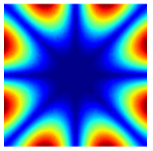	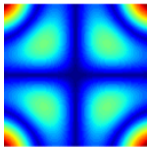
CFFF	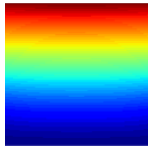	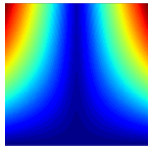	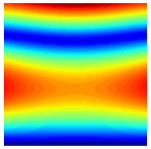	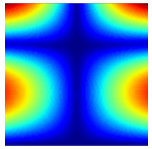	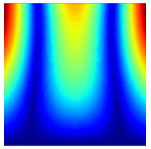		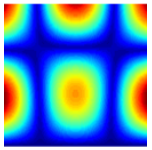	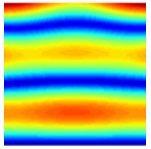	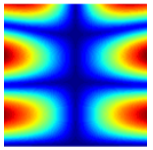	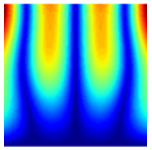
CCFF	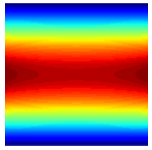	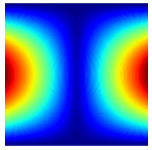	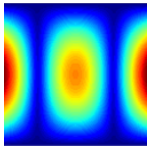	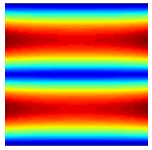	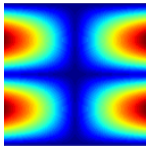	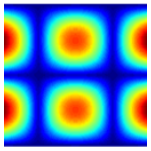	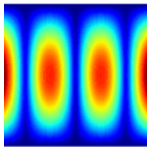	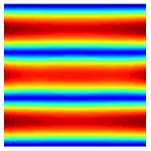	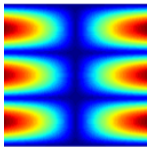	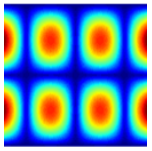
CCCC	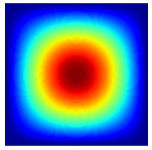	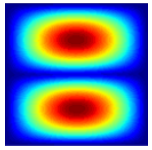	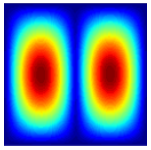	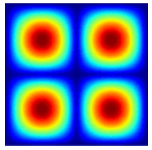	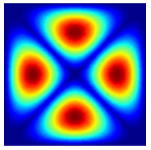	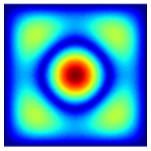	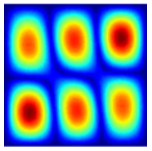	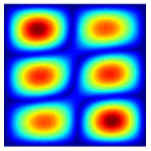	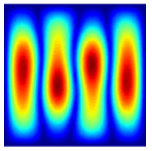	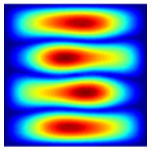

3.2.3 Convolutional Neural Network

After generating contour plots as described in Section 3.2.2, the next step involved leveraging Convolutional Neural Networks (CNNs). The images were randomly divided into two sets: 1000 for training and 250 for testing, for each damage condition and for each mode shape. This procedure was also repeated for each boundary condition.

Managing large datasets posed a primary challenge, with memory overflow a concern. Addressing this, the Keras data generator [135] is employed, facilitating real-time dataset generation across multiple cores, directly feeding into the CNN model.

The network architecture comprised three convolutional layers, three pooling layers, and three dropout layers. The dropout layer, a regularization technique, played a crucial role in preventing overfitting by introducing noise to the image data. Additionally, a multi-head CNN model was chosen, where each mode shape was treated individually by each head of the network. In the detection network, only one neural layer was integrated into the fully connected layer, whereas two layers were employed in the damage localization network. The network optimization utilized the Adam optimizer, whose selection significantly influences the convergence speed and stability during training.

To enhance training efficiency and prevent overfitting, the Early Stop algorithm are employed. This algorithm finishes training when a monitored metric stops improving, ensuring the model achieves optimal performance. For detection tasks, training halts if the validation accuracy remains within a 0.01 variation for 10 consecutive iterations. For damage localization tasks, training stops if the Mean Absolute Error (MAE) stays within a 0.005 variation for 15 consecutive iterations.

Bayesian optimization was employed to select the most suitable hyperparameters for each network. Bayesian optimization served as a powerful tool for selecting the most appropriate hyperparameters for each network. This approach intelligently explores the hyperparameter space, leveraging probabilistic models to refine and optimize hyperparameters iteratively. By balancing exploration and exploitation, Bayesian optimization efficiently navigates the search space, ultimately yielding optimal configurations [136]. Table 4.1 presents the search spaces for each variable chosen for Bayesian optimization.

Finally, the detection network will determine the damage label (undamaged, skin damage, interface damage, and core damage), while the damage localization network will predict the x and y positions of the damage.

Table 3.4: Detection search space for optimization.

Hyperparameter	**detection**	**Damage Localization**
1^{st} convolutional filter	4, 8, 16, 32, 64	4, 8, 16, 32, 64
2^{nd} convolutional filter	8, 16, 32, 64, 128	8, 16, 32, 64, 128
3^{rd} convolutional filter	16, 32, 64, 128, 256	16, 32, 64, 128, 256
Dropout	0.01, 0.025, 0.05, 0.075, 0.10	0.01, 0.025, 0.05, 0.075, 0.10
Neurons in dense layer	256, 512, 1024, 2048, 4096	256, 512, 1024, 2048, 4096
Neurons in 2^{nd} dense layer	-	256, 512, 1024, 2048, 4096
Learning rate ($\times 10^{-3}$)	0.01, 0.05, 0.1, 0.5, 1	0.01, 0.05, 0.1, 0.5, 1

3.3 Results and Discussion

In this section, the results obtained by the proposed method are discussed. Initially, an overview of the modal results obtained from the simulations, focusing on natural frequency and mode shapes are provided. Subsequently, the optimization process to select the most suitable hyperparameters for detection and damage localization are described. Next, the results obtained with the detection network for each boundary condition are compared. Finally, the same analysis is conducted, but this time for the damage localization network.

3.3.1 Natural frequency and mode shapes

In this subsection, the modal results of a representative case study are examined, with emphasis on the CCFF boundary condition. To ensure a consistent comparison, uniform elastic material properties are maintained across all models, thereby isolating the effect of the introduced damage and allowing for a more precise evaluation.

Table 3.5 displays the natural frequency results, indicating an average change of approximately 8.5% for the core damage condition, with extreme cases showing variations as high as 15%. Conversely, minimal deviations are observed in natural frequencies for both skin and interface conditions.

Similarly, a parallel observation is noted when analyzing mode shapes (Table 4.3). Mode shapes corresponding to core damage exhibit distinct variations, whereas those for skin and interface damage remain relatively unchanged compared to the pristine model.

This underscores the inherent challenge of the problem, as the network must effectively discern between subtly different models, except for the core damage, which presents a distinctive alteration.

Table 3.5: Natural frequency (in Hz) for each type of damage.

	Undamaged	**Core Damage**	**Skin damage**	**Interface Damage**
1^{st} mode	609.3	552.1	608.8	609.1
2^{nd} mode	702.8	672.0	701.9	702.4
3^{rd} mode	1200.5	1111.7	1200.1	1200.2
4^{th} mode	1240.0	1171.7	1239.8	1240.6
5^{th} mode	1360.3	1304.3	1360.0	1361.4
6^{th} mode	1721.5	1455.3	1721.4	1722.0
7^{th} mode	1860.1	1560.1	1859.7	1859.7
8^{th} mode	1952.0	1792.5	1953.0	1953.7
9^{th} mode	2046.6	1983.7	2048.4	2049.7
10^{th} mode	2248.3	2079.7	2247.7	2248.1

Table 3.6: First 10 non-null mode shapes for all types of damage at CCFF boundary condition.

Type of Damage	Mode 1	Mode 2	Mode 3	Mode 4	Mode 5	Mode 6	Mode 7	Mode 8	Mode 9	Mode 10
Undamaged	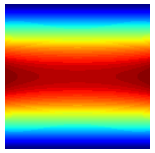	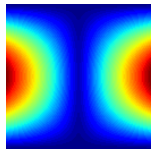	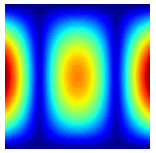	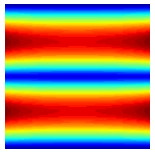	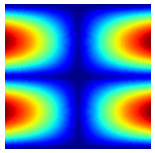	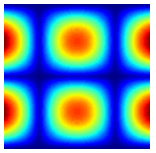	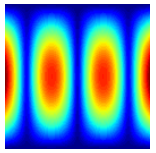	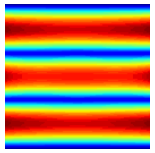	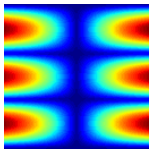	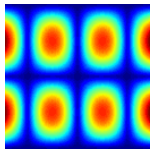
Core Damage	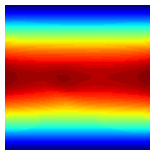	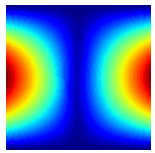	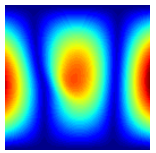	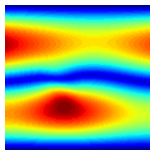	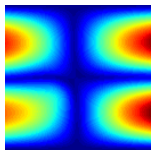	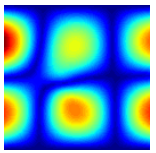	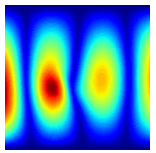	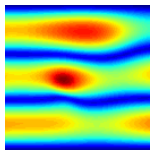	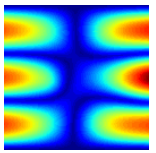	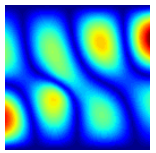
Skin Damage	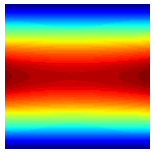	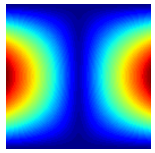	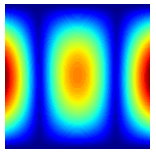	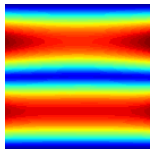	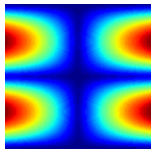	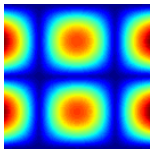	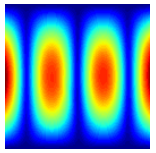	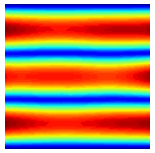	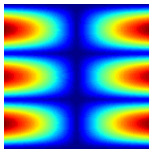	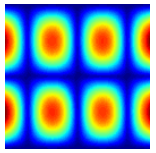
Interface Damage	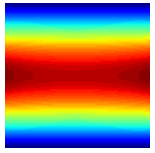	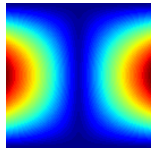	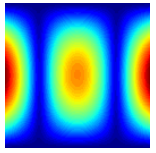	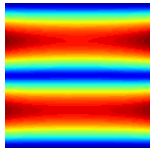	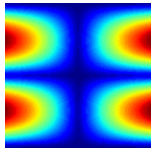	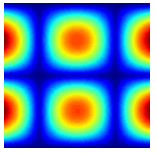	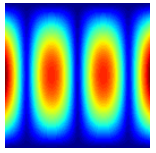	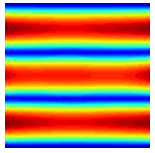	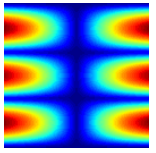	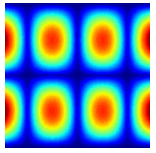

3.3.2 Hyperparameter Tuning

Hyperparameter tuning is a critical step in optimizing the performance of machine learning models. In this study, the Keras Tuner to systematically search for the optimal hyperparameters for the neural network are employed. The Keras Tuner allows for automated hyperparameter optimization by exploring a predefined search space and evaluating the model performance with different hyperparameter combinations.

The objective of hyperparameter tuning can be formulated as an optimization problem where aim to find the set of hyperparameters $\boldsymbol{\lambda}^* = \{\lambda_1, \lambda_2, \ldots, \lambda_n\}$ that minimizes the validation loss $L_{val}(\boldsymbol{\lambda})$:

$$\boldsymbol{\lambda}^* = \arg\min_{\boldsymbol{\lambda}} L_{val}(\boldsymbol{\lambda}), \tag{3.1}$$

where $\boldsymbol{\lambda}$ represents the hyperparameters such as learning rate, batch size, number of layers, number of units in each layer, and activation functions.

To efficiently explore the hyperparameter space, the Bayesian Optimization algorithm within the Keras Tuner is utilized. Bayesian Optimization constructs a probabilistic model of the objective function and uses it to select the most promising hyperparameters to evaluate in the actual objective function. The expected improvement (EI) criterion is often used to balance exploration and exploitation:

$$EI(\boldsymbol{\lambda}) = \mathbb{E}[\max(0, L^*_{val} - L_{val}(\boldsymbol{\lambda}))], \tag{3.2}$$

where L^*_{val} is the best observed value of the validation loss so far. This criterion suggests new hyperparameter values that are expected to yield improvement over the current best solution.

The process of hyperparameter tuning can be summarized in the following steps. First of all, by defining the search space: Specify the range and distribution of hyperparameters to explore. For instance, the learning rate η can be sampled from a logarithmic scale between 10^{-5} and 10^{-2}, and the number of units in each layer can be chosen from a set of discrete values, such as $\{32, 64, 128, 256\}$.

$$\eta \sim \log \mathcal{U}(10^{-5}, 10^{-2}), \tag{3.3}$$

$$\text{units} \in \{32, 64, 128, 256\}. \tag{3.4}$$

Then, by creating an instance of the Keras Tuner with the specified search space and the chosen optimization algorithm (e.g., Bayesian Optimization, Random Search) *kt.BayesianOptimization*.

By systematically tuning the hyperparameters, the generalization capability of the model and achieve better performance on unseen data can be improved. The final model configuration, determined through this tuning process, is then used for training on the entire training dataset and evaluation on the test dataset.

As previously outlined, the Hyperparameters selected for tuning in the study include the filters for the first three convolution layers ($f1, f2, f3$), the dropout rate ($drop$), the number of neurons in the fully connected layers ($dense1, dense2$), and the learning rate (lr). 100 trials using the Bayesian optimizer for the detection network are conducted, whereas, for the damage localization network, 200 trials are performed. This procedure was carried out for each boundary condition, including completely unconstrained (FFFF), one side clamped while the remaining three sides were free (CFFF), two opposite sides

clamped and the other two sides free (CCFF), and finally, all four sides clamped (CCCC). Table 3.7 presents the tuning results for the detection network and the tuning results for the damage location network.

The filters in the convolution layers exhibited significant variation in values, indicating the network's sensitivity to these Hyperparameters. However, a pattern can be discerned; for the initial layers of the network, smaller filter values were favored, while larger filter values were preferred for layers towards the end of the network.

Regarding the dropout layer, most networks found the optimal value to be the lowest (0.01). This outcome aligns with expectations, as the dropout layer serves to introduce noise into the processed image. Despite this, incorporating dropout is essential to mitigate overfitting and enhance the network's generalization capabilities.

Upon initial inspection, the number of neurons in the fully connected layers may appear to lack a discernible pattern. However, when analyzed alongside the learning rate, a relationship becomes apparent. Networks with lower learning rates tended to utilize a greater number of neurons, whereas those with higher learning rates favored fewer neurons. This observation suggests a direct relationship between the learning rate and the number of neurons.

Finally, the optimization yielded different values despite the dataset being similar for each case. This underscores the importance of Hyperparameter tuning to achieve a more precise and robust network. This fine-tuning of Hyperparameters enhances result accuracy and strengthens the network's ability to handle real-world variations and challenges.

Table 3.7: Detection and Damage localization optimization.

detection							
Boundary condition	f1	f2	f3	drop	dense1	dense2	lr ($\times 10^{-3}$)
FFFF	4	32	256	0.01	1024	-	0.5
CFFF	32	128	256	0.01	4096	-	0.1
CCFF	4	64	256	0.01	1024	-	0.5
CCCC	8	32	16	0.05	512	-	0.5
Core damage localization							
Boundary condition	f1	f2	f3	drop	dense1	dense2	lr ($\times 10^{-3}$)
FFFF	32	16	256	0.01	128	1024	0.1
CFFF	4	32	256	0.01	128	4096	0.1
CCFF	4	128	128	0.01	128	512	0.5
CCCC	4	8	32	0.025	256	256	1
Skin damage localization							
Boundary condition	f1	f2	f3	drop	dense1	dense2	lr ($\times 10^{-3}$)
FFFF	4	128	128	0.01	128	2048	0.1
CFFF	32	64	256	0.025	256	128	0.5
CCFF	4	128	128	0.05	128	128	1
CCCC	16	64	256	0.01	256	128	0.1
Interface damage localization							
Boundary condition	f1	f2	f3	drop	dense1	dense2	lr ($\times 10^{-3}$)
FFFF	64	32	32	0.025	128	1024	0.1
CFFF	8	64	256	0.05	1024	512	0.5
CCFF	4	16	128	0.05	256	512	0.5
CCCC	32	128	64	0.01	512	4096	1

3.3.3 Detection network results

Table 3.8 displays the detection report, providing detailed results of the detection process. This report includes three key metrics: Precision (defined by Equation 3.5), Recall (defined by Equation 3.6), and F1-score (defined by Equation 3.7).

$$Precission = \frac{TP}{TP + FP} \tag{3.5}$$

$$Recall = \frac{TP}{TP + FN} \tag{3.6}$$

$$f1 - score = 2 \times \frac{Precission \times Recall}{Precission + Recall} \tag{3.7}$$

where TP indicates true positive, TN indicates true negative, FP indicates false positive, and FN indicates false negative.

The F1 score is often a more reliable metric than precision, particularly when classes are unevenly distributed. Accuracy is preferable when the cost of false negatives equals that of false positives. However, if the costs associated with false positives and false negatives differ significantly, it's important to assess both precision and recall.

The performance of the model in identifying damage was positive, exhibiting near-perfect accuracy in distinguishing between undamaged cases and those with damage (core, skin, and interface). However, when tasked with differentiating between types of damage, particularly damage to the skin and interface, the model encountered more difficulty. In the best scenarios, accuracy hovered around 80%, contrasting with the approximately 100% accuracy achieved in identifying damage to the core.

Furthermore, an analysis of the boundary conditions revealed noteworthy insights. Specifically, conditions characterized by CFFF or CCFF configurations emerged as the most favorable. These conditions consistently yielded superior results compared to others, such as FFFF or CCCC conditions.

These findings underscore the nuanced challenges inherent in damage identification and highlight the influence of boundary conditions on model performance. While the model demonstrates remarkable proficiency overall, further refinement may be warranted to enhance its ability to accurately differentiate between different types of damage, particularly in scenarios involving skin and interface damage.

Confusion matrix plots were generated to gain deeper insights into the network's predictions (Figure 3.7). These visualizations revealed a notable challenge for the network in accurately distinguishing between skin and interface damage. This outcome was anticipated, given the intrinsic characteristics and positioning of the defects within the structure. Conversely, the model exhibited a high degree of accuracy in distinguishing between damage to the core and undamaged cases. Confusion with other types of defects was minimal, underscoring the model's effectiveness in precisely identifying core damage.

3.3.4 Damage localization network results

This study parameterized damage using multiple attributes, including position, size, orientation, and extension. Despite extensive efforts in the identification process, the complexity inherent in the problem posed significant challenges. While the identification of damage position was achieved with satisfactory accuracy, the artificial intelligence (AI)

Table 3.8: Detection test report.

Undamaged			
Boundary condition	Precision	Recall	f1-score
FFFF	0.98	1.00	0.99
CFFF	0.97	1.00	0.98
CCFF	**1.00**	**1.00**	**1.00**
CCCC	0.81	0.99	0.89
Core			
Boundary condition	Precision	Recall	f1-score
FFFF	0.97	0.93	0.95
CFFF	1.00	0.97	0.98
CCFF	**1.00**	**0.98**	**0.99**
CCCC	0.95	0.95	0.95
Skin			
Boundary condition	Precision	Recall	f1-score
FFFF	0.69	0.74	0.71
CFFF	**0.77**	**0.80**	**0.79**
CCFF	0.75	0.64	0.69
CCCC	0.61	0.46	0.53
Interface			
Boundary condition	Precision	Recall	f1-score
FFFF	0.73	0.69	0.71
CFFF	**0.79**	**0.77**	**0.78**
CCFF	0.69	0.79	0.73
CCCC	0.58	0.59	0.58

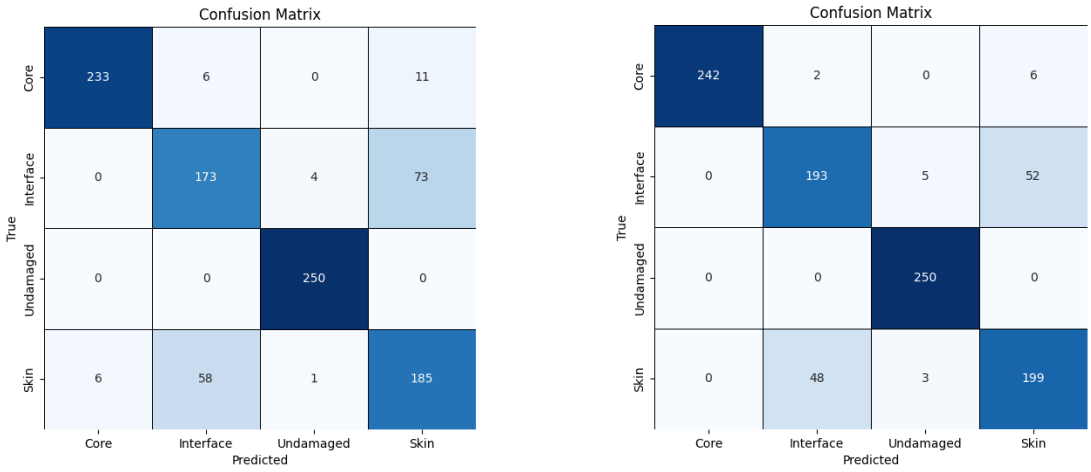

(a) (b)

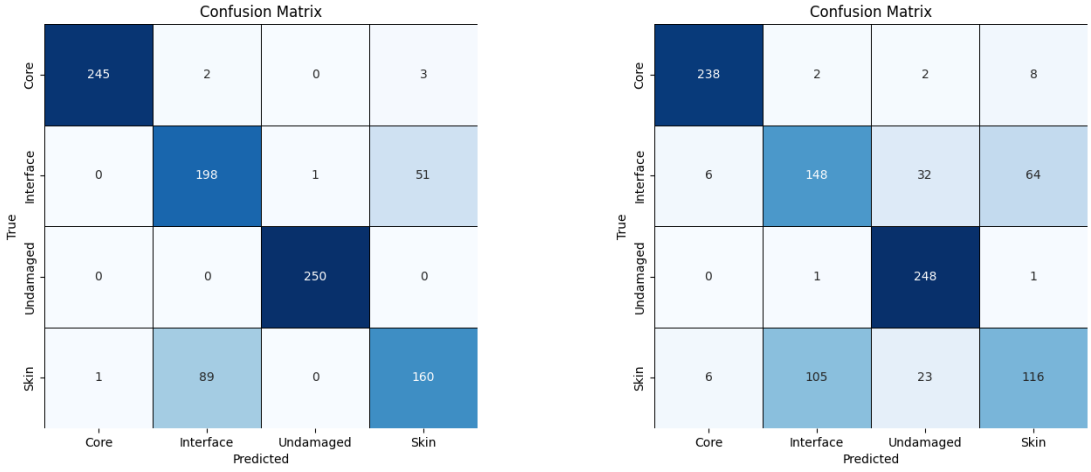

(c) (d)

Figure 3.7: Prediction confusion matrix: (a) FFFF, (b)CFFF, (c) CCFF, (d) CCCC.

model exhibited difficulties in predicting other critical parameters such as orientation and size, especially for 2D and 3D damage scenarios.

The AI model's performance in identifying these additional parameters was limited, resulting in predictions that often oscillated around a central average value without achieving precise accuracy. This behavior can be attributed to the high dimensionality and nonlinearity of the problem space, which exacerbates the difficulty of accurately mapping the relationship between the observed data and the underlying damage parameters.

It is important to emphasize that the successful identification of the damage position should be viewed as a significant accomplishment, given the inherent complexity of the problem. The limitations observed in predicting orientation, size, and other parameters underscore the need for further advancements in AI methodologies and the development of more sophisticated models capable of handling such intricate tasks.

Once we've identified the type of damage, we move forward with localizing it. The localization model is structured into three distinct categories: core, interface, and skin. This segmentation ensures that data is directed to the appropriate model based on its detection outcome. The results obtained by the damage localization network are presented in Table 4.7.

Overall, the damage localization process yielded satisfactory outcomes. An error margin averaging around 10-12 mm are observed. Considering the total size of the plate (250 mm), this equates to a percentage error of approximately 4-5%. Notably, in line with the detection results, the boundary conditions that exhibited the most accurate localization were CFFF and CCFF.

To enhance the understanding of the damage localization network, several plots are generated (Figures 3.8, 3.9, and 3.10). First, dispersion plots are constructed by comparing the norm of the real values, defined as $\sqrt{x^2 + y^2}$, with the corresponding predicted values. In parallel, the coefficient of determination (R^2) is computed to assess the goodness of fit of the model. Additionally, histograms of the residuals are analyzed to evaluate the model performance based on the residual distribution. A residual distribution closer to a normal distribution indicates a better capability of the model to capture the underlying relationship between the variables. Although the CFFF and CCFF boundary conditions presented the lowest MAE values, a more detailed analysis considering both the R^2 score and the residual histograms reveals that the CCFF condition consistently exhibits superior overall performance compared to the other boundary conditions.

Figures 3.11, 3.12, and 3.13 illustrate the localization of damage in the core, skin, and interface under each boundary condition in a stochastic manner. In these figures, the blue region indicates the original damage, the red dot represents the damage center predicted by the network, and the red area shows the 95% confidence interval. This confidence interval is based on the standard error of the residuals in both the x and y directions. As observed in the residual plots, all conditions exhibited a normal distribution pattern. Therefore, the normal distribution was used to create the confidence interval.

Table 3.9: Damage localization optimization.

Core		
Boundary condition	MAE X (mm)	MAE Y (mm)
FFFF	12.2	12.4
CFFF	11.0	12.4
CCFF	**8.2**	**7.2**
CCCC	14.8	14.1
Skin		
Boundary condition	MAE X (mm)	MAE Y (mm)
FFFF	12.1	14.3
CFFF	**9.9**	13.5
CCFF	12.5	**13.1**
CCCC	20.0	22.6
Interface		
Boundary condition	MAE X (mm)	MAE Y (mm)
FFFF	13.6	13.2
CFFF	11.3	10.8
CCFF	**9.5**	**8.5**
CCCC	14.4	13.0

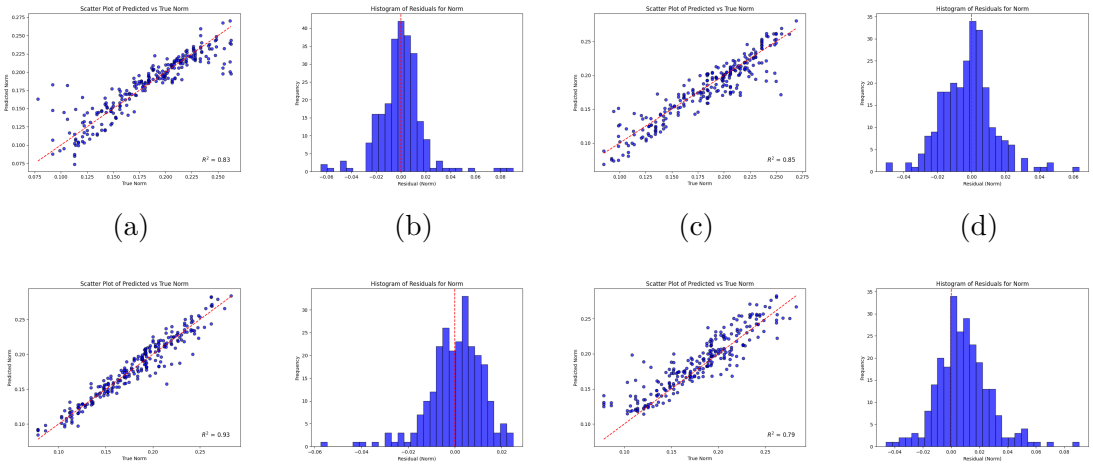

(a) (b) (c) (d)

(e) (f) (g) (h)

Figure 3.8: Core dispersion and histogram plot: (a) FFFF Dispersion plot, (b) FFFF residuals, (c) CFFF Dispersion plot, (d) CFFF residuals, (e) CCFF Dispersion plot, (f) CCFF residuals, (g) CCCC Dispersion plot, (h) CCCC residuals.

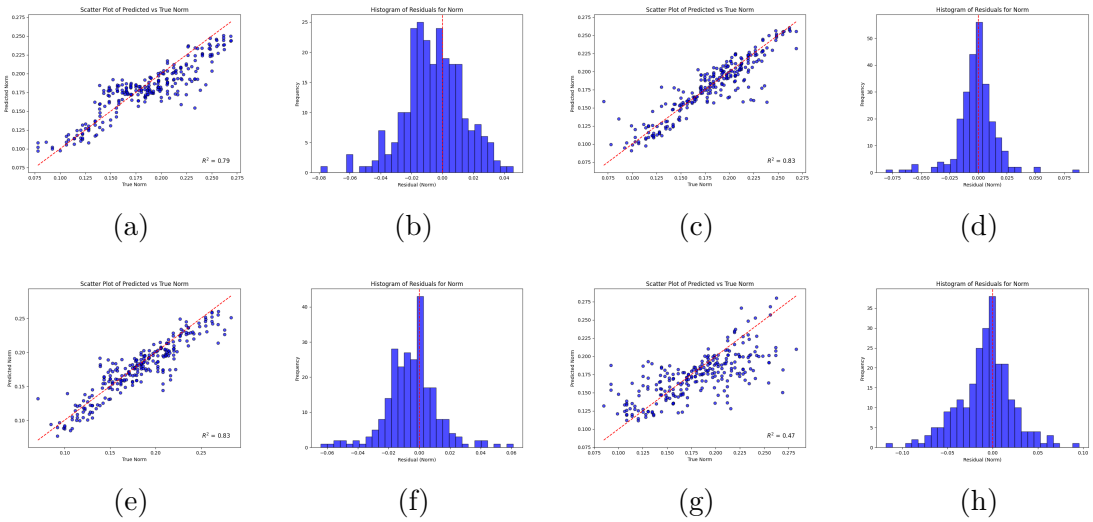

Figure 3.9: Skin dispersion and histogram plot: (a) FFFF Dispersion plot, (b) FFFF residuals, (c) CFFF Dispersion plot, (d) CFFF residuals, (e) CCFF Dispersion plot, (f) CCFF residuals, (g) CCCC Dispersion plot, (h) CCCC residuals.

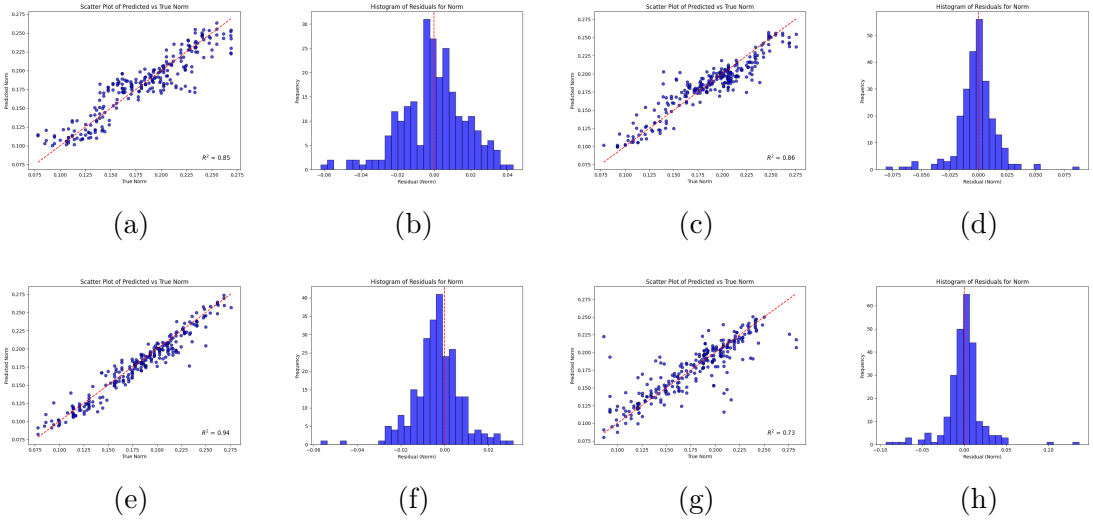

Figure 3.10: Interface dispersion and histogram plot: (a) FFFF Dispersion plot, (b) FFFF residuals, (c) CFFF Dispersion plot, (d) CFFF residuals, (e) CCFF Dispersion plot, (f) CCFF residuals, (g) CCCC Dispersion plot, (h) CCCC residuals.

To enhance the visualization of the damage prediction accuracy, confidence ellipses are introduced to represent the uncertainty associated with the predicted damage locations. These ellipses provide a more comprehensive assessment of the model performance by illustrating the 95% confidence interval of the predicted damage positions.

The confidence intervals were calculated based on the residuals and deviations of the predicted damage positions from the true damage positions. The residuals in the x and y directions are computed as shown in Equation 3.8 and Equation 3.9.

$$\text{residual}_x = \hat{x}_i - x_i \tag{3.8}$$

$$\text{residual}_y = \hat{y}_i - y_i \tag{3.9}$$

where $\hat{x}_i$ and $\hat{y}_i$ are the predicted coordinates, and x_i and y_i are the true coordinates of the damage.

The variances σ_{hx}^2 and σ_{hy}^2 of the residuals are then calculated as shown in Equation 3.10 and Equation 3.11.

$$\sigma_{hx}^2 = \text{Var}(\text{residual}_x) \tag{3.10}$$

$$\sigma_{hy}^2 = \text{Var}(\text{residual}_y) \tag{3.11}$$

The standard errors se_x and se_y are obtained by taking the square roots of the variances, as shown in Equation 3.12 and Equation 3.13.

$$se_x = \sqrt{\sigma_{hx}} \tag{3.12}$$

$$se_y = \sqrt{\sigma_{hy}} \tag{3.13}$$

To determine the 95% confidence interval, the Z-value corresponding to a confidence level of 95% is used. This Z-value is derived from the standard normal distribution as shown in Equation 3.14.

$$Z = \Phi^{-1}\left(1 - \frac{1 - \text{conf}}{2}\right) \tag{3.14}$$

where Φ^{-1} is the inverse of the cumulative distribution function (CDF) of the standard normal distribution. For a 95% confidence level, $Z \approx 1.96$.

The confidence radius $conf_{rx}$ and $conf_{ry}$ for the x and y directions are then calculated as shown in Equation 3.15 and Equation 3.16.

$$conf_{rx} = Z \cdot se_x \tag{3.15}$$

$$conf_{ry} = Z \cdot se_y \tag{3.16}$$

These confidence radii are used to define the width and height of the confidence ellipse. The ellipse is centered at the predicted damage position $(\hat{x}, \hat{y})$ with axes aligned to the coordinate directions, having a width of $2 \cdot conf_{rx}$ and a height of $2 \cdot conf_{ry}$.

In Figures 3.11, 3.12, and 3.13, the confidence ellipses (shaded in red) visually indicate the region within which the true damage location is expected to lie with 95% confidence. This additional layer of information highlights the precision of the position predictions while acknowledging the inherent uncertainties in the model's outputs.

Figure 3.11: Core Damage location: Line 1 - FFFF; Line 2 - CFFF; Line 3 - CCFF; Line 4 - CCCC. Legend: ◯ Real damage • Predicted position of the damage ⊙ 95% confidence interval.

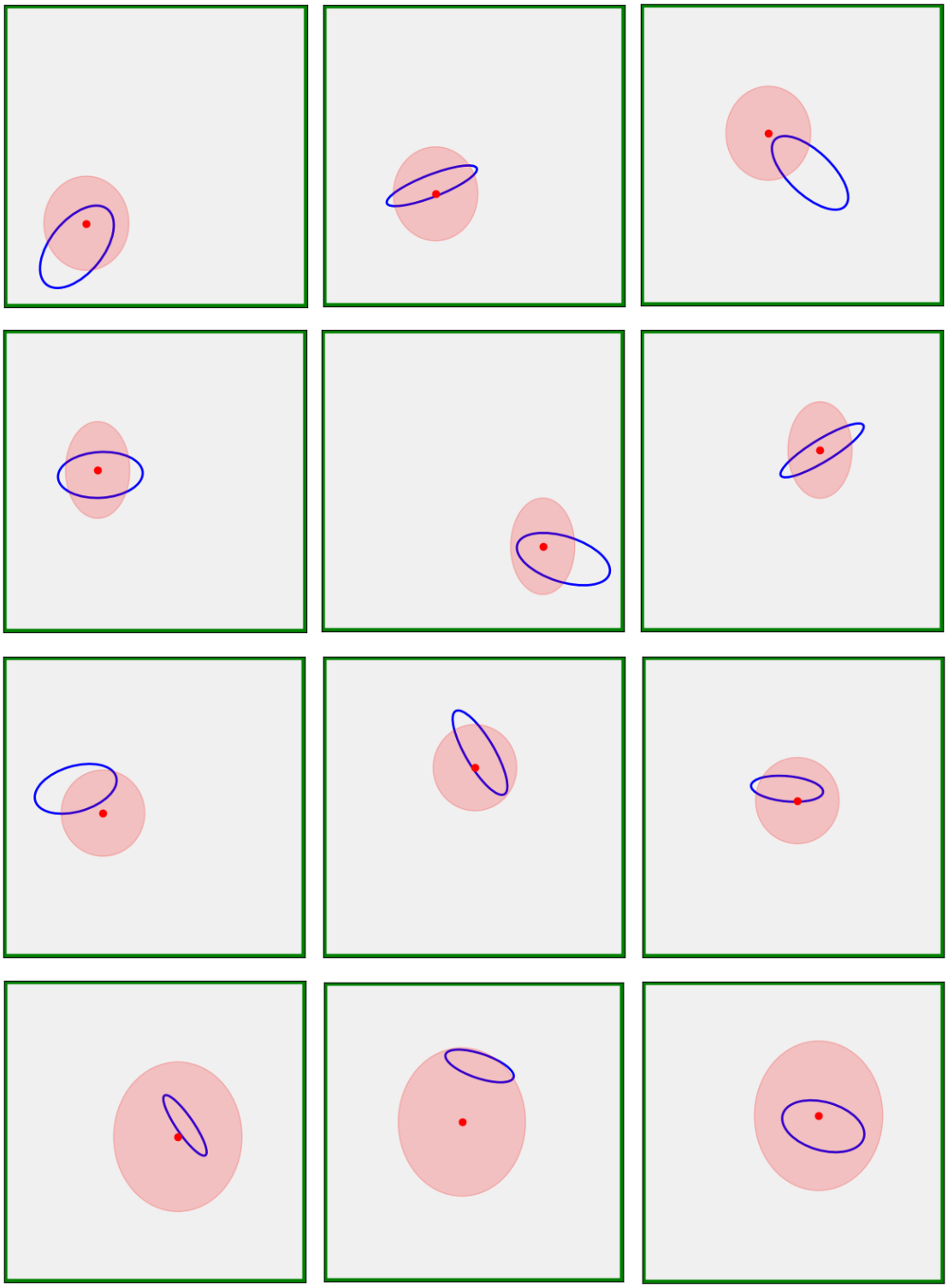

Figure 3.12: Skin Damage location:Line 1 - FFFF; Line 2 - CFFF; Line 3 - CCFF; Line 4 - CCCC. Legend: ◯ Real damage • Predicted position of the damage ⊙ 95% confidence interval.

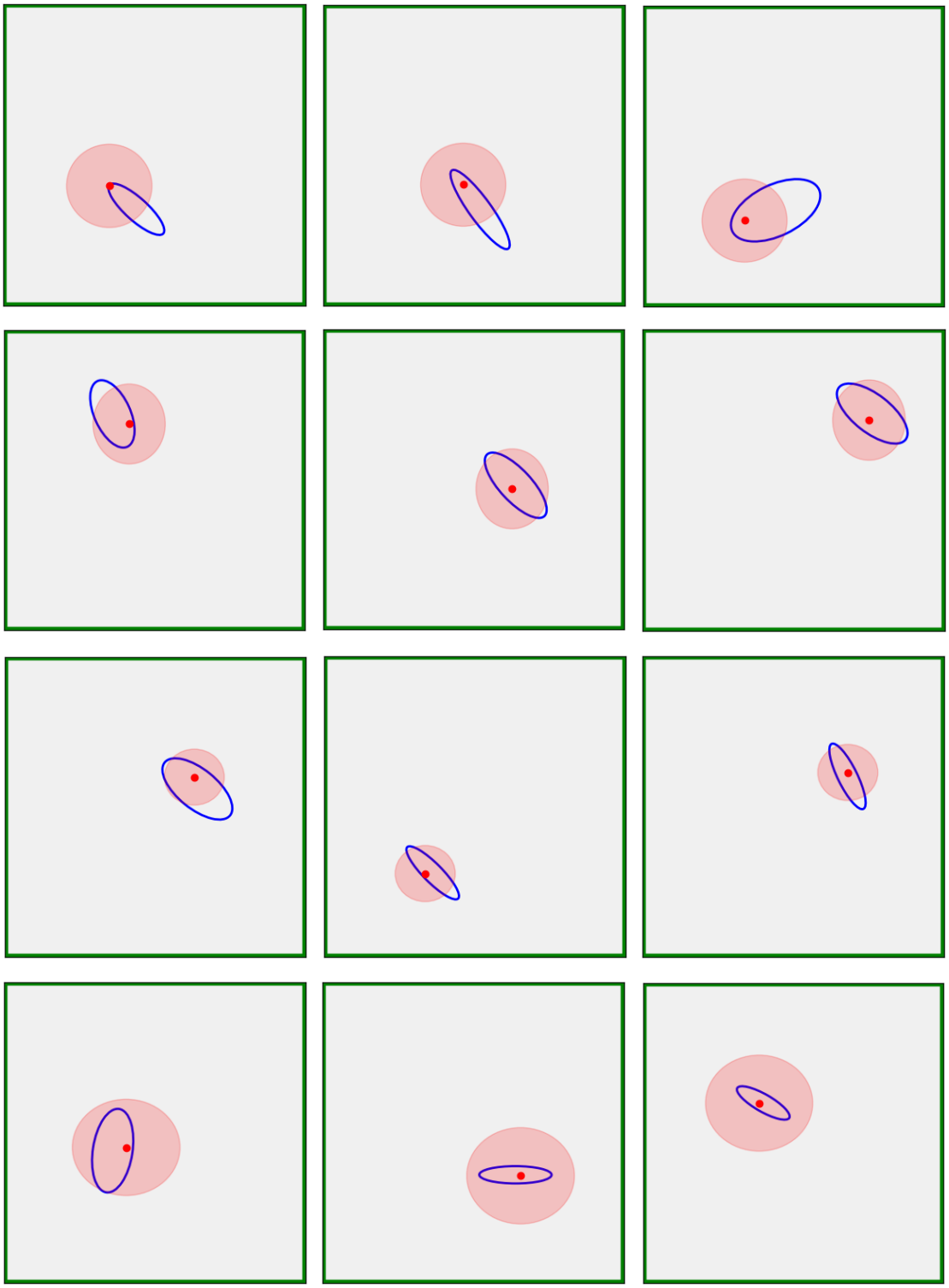

Figure 3.13: Interface Damage location: Line 1 - FFFF; Line 2 - CFFF; Line 3 - CCFF; Line 4 - CCCC. Legend: ◯ Real damage • Predicted position of the damage ⊙ 95% confidence interval.

The images show that for conditions where the network had worse accuracy, such as CCCC Skin damage, the confidence interval is quite large. In contrast, for CCFF Core damage, the confidence interval is small, highlighting the quality of the damage localization. From a global perspective, the CCFF condition exhibited the smallest confidence interval, indicating the best results for locating the damage. Moreover, in real-world

applications, where structures are generally larger and the extent of damage is not significantly greater, the proportional error is likely to be smaller. This, in turn, enhances the accuracy of the method.

In summary, combining detection and localization models offers a robust approach to damage assessment. By segmenting the damage into core, interface, and skin categories, ensuring that each type of damage is addressed with the appropriate model, enhances the overall precision of the predictions. The visual and statistical analyses validate the effectiveness of the models, particularly under the CCFF boundary condition, which consistently demonstrated superior performance. These findings are instrumental in advancing the application of damage localization networks in practical, real-world scenarios, paving the way for more accurate and reliable structural health monitoring systems.

3.4 Chapter Conclusion

This chapter developed and evaluated a vibration-based damage identification framework that combines mode shape information and Convolutional Neural Networks for the detection, detection, and localization of damage in composite sandwich panels. The proposed approach employed the first ten vibration mode shapes to identify damage into four categories—undamaged, core damage, skin damage, and interface damage—followed by a dedicated CNN to determine the spatial location of the identified damage. The methodology was systematically assessed under four distinct boundary conditions: FFFF, CFFF, CCFF, and CCCC.

The results demonstrated that mode shape–based representations contain sufficient spatial information to enable highly accurate damage detection and localization across different structural constraints. Nearly perfect detection accuracy was achieved for undamaged and core damage scenarios, while skin and interface damage cases were identified with accuracies of approximately 80%. Regarding damage localization, even under the most challenging conditions, the maximum error remained limited to approximately 5%, indicating a strong localization capability of the proposed framework.

From a methodological perspective, this chapter introduces a two-stage CNN-based strategy that decouples damage detection from localization, enhancing both interpretability and performance. The use of confidence ellipses to represent localization results provided an effective and intuitive visualization of prediction uncertainty, offering additional insight into the reliability of the estimated damage positions.

Despite the encouraging results, the proposed approach exhibited limitations in accurately estimating secondary damage parameters, such as damage orientation and size. The predictions for these parameters tended to converge toward average values, reflecting the inherent complexity of the problem and the limited sensitivity of mode shape data to such fine-grained damage characteristics. These limitations highlight the need for more advanced learning strategies capable of incorporating additional physical constraints and richer information.

Overall, the findings confirm the robustness and effectiveness of the proposed method for damage identification and localization in composite sandwich panels under varying boundary conditions. This chapter establishes a solid foundation for subsequent developments aimed at improving performance in skin and interface damage scenarios and extending the framework to predict a broader set of damage parameters using advanced deep learning techniques.

4 Enhanced Damage Detection and Localization in Composite Sandwich Structures Using Mode Shapes, Image Processing, and Convolutional Neural Networks

Building upon the methodology presented in Chapter 3, the present chapter follows the same fundamental framework that combines vibration-based mode shapes and Convolutional Neural Networks (CNNs) for damage identification and localization in sandwich panels. However, the proposed approach advances the previous methodology by significantly enhancing the image-processing stage and extending the damage characterization capabilities of the learning model. Several image-processing techniques were investigated to improve the quality and discriminative power of the input data, among which the residual-based technique demonstrated superior performance. Unlike the previous approach, which relied on a confidence region to indicate damage location, the current methodology employs a dedicated CNN to directly predict both the damage location and geometry. This prediction is performed using five parameters: two describing the spatial position of the damage and three defining its geometric characteristics, such as size and orientation. This extension represents a substantial evolution over the baseline model introduced in Chapter 3, enabling a more detailed and physically meaningful damage description. A comparative analysis between the proposed framework and the baseline model reveals significant improvements in localization accuracy, particularly with respect to spatial precision and geometric parameter estimation, thereby demonstrating the effectiveness of the enhanced image-processing strategy and the refined CNN architecture.

The chapter is organized as follows: Section 4.1 introduces the attention mechanism adopted in the proposed networks. Section 4.2 describes the image processing techniques applied to the mode shapes. Section 4.3 details the enhanced methodology combining image processing and CNNs. The results and comparative analysis are presented in Section 4.4. Finally, Section 4.5 summarizes the main conclusions of the chapter.

4.1 Squeeze-and-Excitation Block

To enhance the model's representational power, a Squeeze-and-Excitation (SE) block [137] was integrated into the CNN architecture. The SE mechanism adaptively recalibrates channel-wise feature responses by explicitly modeling interdependencies between feature channels. This enables the network to emphasize informative features and suppress less relevant ones.

Given an input feature map $\mathbf{U} \in \mathbb{R}^{H \times W \times C}$, where H, W, and C denote the height, width, and number of channels, respectively, the Squeeze-and-Excitation (SE) block operates in three main steps:

1. **Squeeze:** The spatial dimensions are aggregated using global average pooling to generate a channel descriptor $\mathbf{z} \in \mathbb{R}^C$, which encodes the global distribution of feature responses for each channel:

$$z_c = \frac{1}{H \times W} \sum_{i=1}^{H} \sum_{j=1}^{W} U_c(i, j), \quad c = 1, \ldots, C. \tag{4.1}$$

2. **Excitation:** The channel descriptor $\mathbf{z}$ is then passed through two fully connected layers with nonlinear activation (ReLU followed by sigmoid) to learn channel-wise dependencies and generate a set of modulation weights $\mathbf{s} \in [0, 1]^C$:

$$\mathbf{s} = \sigma\left(\mathbf{W}_2\, \delta(\mathbf{W}_1 \mathbf{z})\right), \tag{4.2}$$

   where $\delta(\cdot)$ denotes the ReLU activation, $\sigma(\cdot)$ is the sigmoid function, and $\mathbf{W}_1 \in \mathbb{R}^{\frac{C}{r} \times C}$ and $\mathbf{W}_2 \in \mathbb{R}^{C \times \frac{C}{r}}$ are learnable weight matrices. The reduction ratio r controls the capacity and computational cost of the excitation network.

3. **Recalibration:** Finally, the learned weights $\mathbf{s}$ are applied to the original feature maps via channel-wise multiplication to produce the recalibrated output $\tilde{\mathbf{U}}$:

$$\tilde{U}_c = s_c \cdot U_c. \tag{4.3}$$

Through this mechanism, the SE block enhances the network's ability to focus on the most discriminative features, improving both the detection and regression performance.

4.2 Image processing techniques

Various image processing techniques were applied to enhance the CNN's ability to extract meaningful and discriminative features from the mode shapes. These techniques emphasize different structural characteristics, such as edges, textures, and curvature variations, which can indicate the presence of damage. By transforming the original images into multiple representations, the CNN is exposed to richer information, possibly improving its performance in detection and localization tasks. The following preprocessing methods were utilized:

4.2.1 Canny Edge Detection

Canny edge detection is a multi-stage algorithm for identifying a wide range of edges in images [138]. It includes Gaussian smoothing, gradient computation, non-maximum suppression, and hysteresis thresholding. The gradient magnitude G and orientation θ are computed as:

$$G = \sqrt{G_x^2 + G_y^2} \tag{4.4}$$

$$\theta = \tan^{-1}\left(\frac{G_y}{G_x}\right) \tag{4.5}$$

where G_x and G_y are image gradients in the horizontal and vertical directions, respectively.

4.2.2 Curvature Enhancement

Curvature-based processing emphasizes structural deformations by enhancing second-order spatial variations in the mode shapes [139]. The curvature κ is approximated using the Laplacian of the displacement field $u(x, y)$:

$$\kappa(x, y) = \frac{\partial^2 u}{\partial x^2} + \frac{\partial^2 u}{\partial y^2} \tag{4.6}$$

This helps highlight regions with increased bending or deformation, often associated with damage.

4.2.3 Laplace Operator

The Laplace operator, a second-order differential operator, highlights regions of rapid intensity change and is useful for detecting edges and transitions in the image. It is defined as:

$$\nabla^2 f(x, y) = \frac{\partial^2 f}{\partial x^2} + \frac{\partial^2 f}{\partial y^2} \tag{4.7}$$

where $f(x, y)$ represents the image (mode shape).

4.2.4 Residual Image

Residual images emphasize details and variations by subtracting a reference image from a target image. In this work, the undamaged mode shape $f_u(x, y)$ is subtracted from the damaged one $f_d(x, y)$:

$$R(x, y) = f_d(x, y) - f_u(x, y) \tag{4.8}$$

This technique accentuates localized changes potentially related to structural damage.

4.2.5 Residual Curvature

This method combines the curvature approach with the residual concept by subtracting the curvature of the undamaged image from the curvature of the damaged one:

$$RC(x, y) = \kappa_d(x, y) - \kappa_u(x, y) \tag{4.9}$$

The resulting image enhances subtle curvature changes that are more prominent in damaged regions.

4.2.6 Sobel Filtering

Sobel operators estimate the gradient of the image intensity, emphasizing directional edges and transitions [140]. The horizontal and vertical gradients are obtained by convolving the image with the following kernels:

$$G_x = \begin{bmatrix} -1 & 0 & +1 \\ -2 & 0 & +2 \\ -1 & 0 & +1 \end{bmatrix}, \quad G_y = \begin{bmatrix} -1 & -2 & -1 \\ 0 & 0 & 0 \\ +1 & +2 & +1 \end{bmatrix} \tag{4.10}$$

The magnitude of the gradient is computed similarly to the Canny method:

$$G = \sqrt{G_x^2 + G_y^2} \tag{4.11}$$

4.2.7 Wavelet Transform

Wavelet transforms perform multiscale decomposition of images, allowing the analysis of both spatial and frequency components [141]. A 2D Discrete Wavelet Transform (DWT) decomposes the image into approximation and detail coefficients:

$$f(x, y) \rightarrow \{A_j, H_j, V_j, D_j\}_{j=1}^{N} \tag{4.12}$$

where A_j is the approximation (low-frequency) component, and H_j, V_j, and D_j are the horizontal, vertical, and diagonal detail coefficients at level j.

The application of these techniques allowed for the extraction of complementary features, enhancing the representation of mode shapes and improving CNN robustness in damage detection and localization. Figure 4.1 illustrates the processing results for the 1st mode shape in its original form and after applying each technique under the core damage condition.

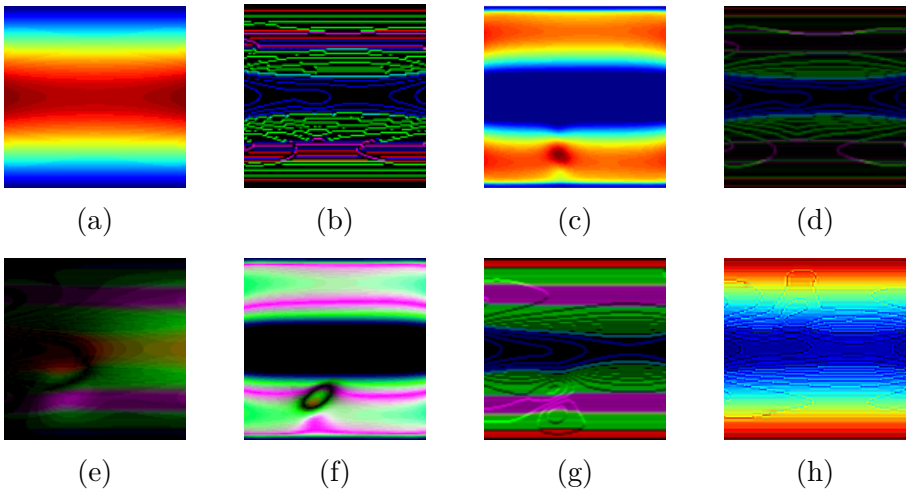

Figure 4.1: First mode shape for core damage condition: (a) Original, (b) Canny, (c) Curvature, (d) Laplace, (e) Residual, (f) Residual curvature, (g) Sobel, (h) Wavelet.

4.3 methodology

The methodology involved the application of Convolutional Neural Networks for damage detection and localization based on mode shape contour images. The modal simulation allowed us to generate contour plots of the mode shapes; however, before feeding them into the network, a processing step was applied to the images using the following techniques: Canny, Curvature, Laplace, Residual, Residual Curvature, Sobel, and Wavelet. For each technique and vibration mode, the dataset was randomly divided into two subsets, comprising 1,000 images for training and 250 images for testing.

Handling a large number of high-resolution images posed computational and memory-related challenges. To mitigate these issues, the Keras data generator [135] was employed,

enabling on-the-fly data loading and preprocessing. This approach allowed efficient utilization of system memory while leveraging parallel processing across multiple CPU cores, ensuring a continuous and scalable data pipeline during network training.

The adopted CNN architecture consists of three convolutional layers, each followed by a pooling layer and a dropout layer to progressively extract hierarchical features while controlling model complexity. Dropout was incorporated as a regularization mechanism to reduce overfitting by randomly deactivating a fraction of neurons during training, effectively introducing noise and improving the generalization capability of the network.

A multi-head CNN architecture was implemented, in which each head independently processes the contour plot corresponding to a specific vibration mode. This design enables the network to learn mode-specific features while preserving the complementary information contained across different modes. The extracted features from all heads are subsequently concatenated and fed into fully connected layers for decision-making. In the detection network, a single dense layer is employed before the output layer, whereas the damage localization (regression) network utilizes two dense layers to better capture the increased complexity associated with predicting continuous damage parameters.

The network weights were optimized using the Adam optimizer, selected for its adaptive learning rate strategy, fast convergence, and robustness when handling noisy gradients. To further enhance feature discrimination and improve model performance, Squeeze-and-Excitation (SE) blocks [137] were integrated into the convolutional layers. By adaptively reweighting feature channels, the SE blocks enable the network to emphasize damage-sensitive patterns in the mode shapes, thereby improving both detection accuracy and localization precision.

To prevent overfitting and reduce unnecessary training iterations, an Early Stopping strategy was adopted. For detection tasks, training was terminated when the validation accuracy exhibited a variation smaller than 0.01 over 10 consecutive epochs. For damage localization, training was stopped when the Mean Absolute Error (MAE) variation remained below 0.005 for 15 consecutive epochs. This criterion ensured convergence while maintaining computational efficiency.

Hyperparameter tuning was conducted using Bayesian optimization, which systematically explores the hyperparameter space by constructing probabilistic surrogate models and iteratively updating them based on observed performance [136]. This approach effectively balances exploration and exploitation, allowing the identification of near-optimal configurations with fewer evaluations than grid or random search. The search ranges for the optimized hyperparameters are summarized in Table 3.4.

Finally, the detection network outputs the predicted damage (undamaged, core damage, skin damage, or interface damage), while the damage localization network estimates five continuous parameters describing the defect: the spatial coordinates (x, y), the orientation angle (θ), and the geometric parameters (r, c). A schematic overview of the combined detection and localization framework is presented in Figure 4.2.

4.4 Results and Discussion

In this section, we present and analyze the results achieved by the proposed method. We begin with an overview of the results of the modal analysis, highlighting the natural frequencies and mode shapes obtained from the simulations. Next, we detail the optimization process used to determine the most effective hyperparameters for detection and damage localization. We then compare the detection performance across different image

Table 4.1: Detection and Damage localization search space for optimization.

Hyperparameter	**Detection**	**Damage Localization**
1^{st} convolutional filter	4, 8, 16, 32, 64	4, 8, 16, 32, 64
2^{nd} convolutional filter	8, 16, 32, 64, 128	8, 16, 32, 64, 128
3^{rd} convolutional filter	16, 32, 64, 128, 256	16, 32, 64, 128, 256
Dropout	0.010, 0.025, 0.050, 0.075, 0.100	0.010, 0.025, 0.050, 0.075, 0.100
Neurons in dense layer	256, 512, 1024, 2048, 4096	256, 512, 1024, 2048, 4096
Neurons in 2^{nd} dense layer	-	256, 512, 1024, 2048, 4096
Learning rate ($\times 10^{-3}$)	0.01, 0.05, 0.1, 0.5, 1	0.01, 0.05, 0.1, 0.5, 1

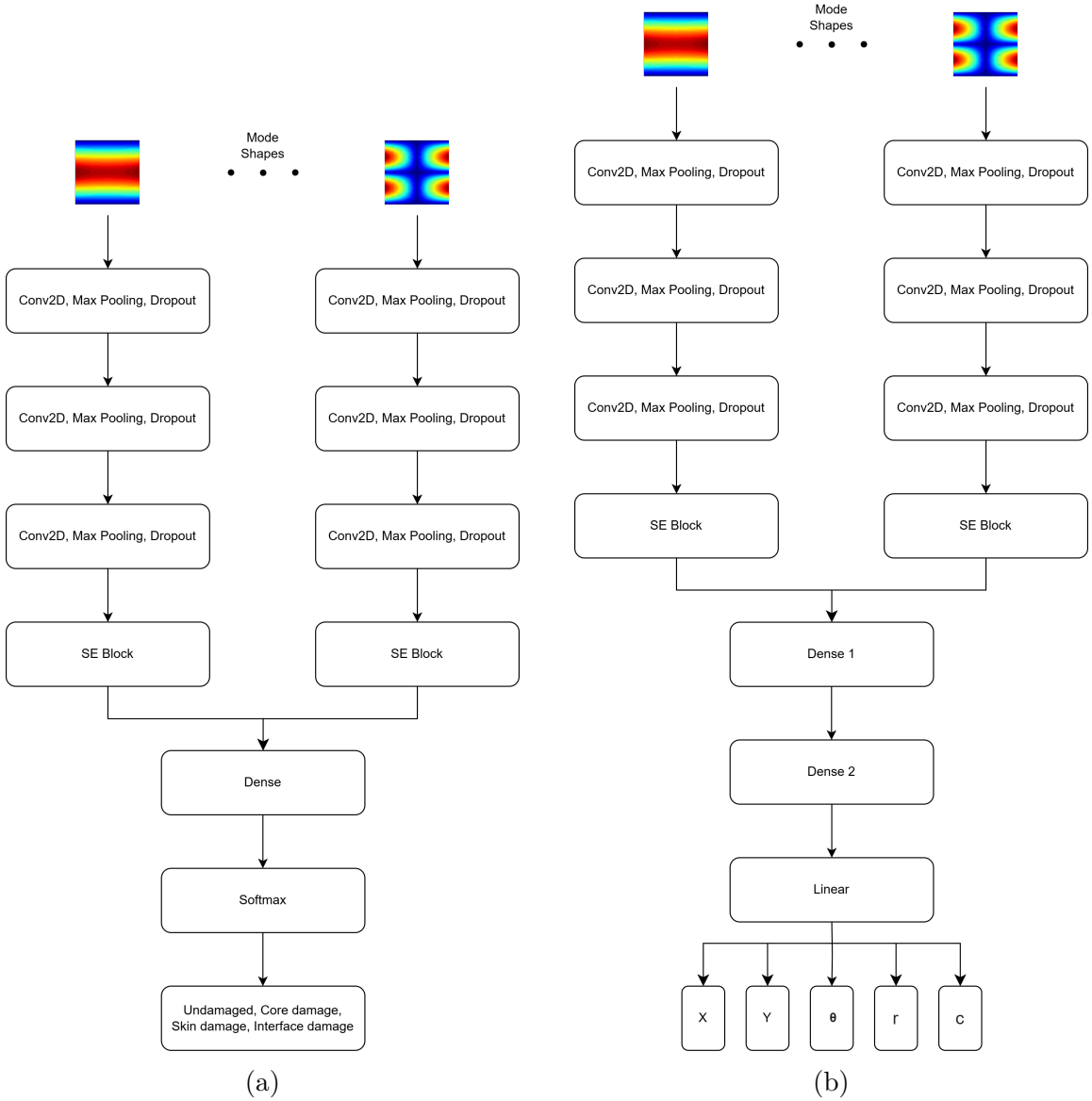

Figure 4.2: CNN architecture: (a) detection network, (b) Damage localization network.

processing techniques, including a baseline without image processing. Finally, we evaluate the damage localization results using the most effective detection approach.

4.4.1 Natural frequency and mode shapes

In this subsection, we analyze the results of the modal analysis, focusing on natural frequencies. To ensure consistency, we maintain uniform elastic material properties across all models. This approach guarantees that any observed variations result solely from the introduced damage, allowing for a clearer assessment of its impact.

Table 4.2 presents the results of the natural frequency, revealing an average reduction of approximately 6.16% in the presence of damage to the core, with extreme cases showing deviations of up to 9.39%. In contrast, changes in natural frequencies for skin and interface damage conditions are minimal.

A similar trend is observed in the analysis of mode shapes (Table 3.6). Core damage leads to noticeable variations in mode shapes, whereas those associated with skin and interface damage remain largely consistent with the undamaged model.

Table 4.2: Natural frequency (in Hz) and relative variation (%) compared to undamaged case.

	Undamaged	**Core Damage**	**Skin damage**	**Interface Damage**
1^{st} mode	609.3	552.1 (-9.39%)	608.8 (-0.10%)	609.1 (-0.03%)
2^{nd} mode	702.8	672.0 (-4.39%)	701.9 (-0.10%)	702.4 (-0.06%)
3^{rd} mode	1200.5	1111.7 (-7.40%)	1200.1 (-0.03%)	1200.2 (-0.02%)
4^{th} mode	1240.0	1171.7 (-5.50%)	1239.8 (-0.02%)	1240.6 (+0.05%)
5^{th} mode	1360.3	1304.3 (-4.12%)	1360.0 (-0.02%)	1361.4 (+0.08%)

Detecting damage in sandwich structures presents a significant challenge, particularly for skin and interface defects, as they cause only slight changes in modal parameters. These subtle variations are often indistinguishable from those resulting from environmental influences such as temperature and humidity, which similarly alter structural properties. Consequently, traditional vibration-based techniques struggle to accurately identify damage, leading to a high likelihood of false positives and negatives.

To overcome this limitation, this study leverages advanced image processing techniques in combination with artificial intelligence. Convolutional Neural Networks offer a key advantage by transforming mode shapes into contour plots, reframing damage detection as an image recognition problem. This enables CNNs to identify even the most subtle variations in mode shapes with exceptional sensitivity, detecting patterns that conventional methods might miss. As a result, the accuracy of damage identification is significantly enhanced, especially in cases where changes in modal parameters are minimal.

By training on large datasets, CNNs can effectively distinguish genuine structural damage from minor variations caused by environmental conditions, providing a more reliable and robust solution for real-world applications. This AI-powered, image-based approach is crucial for addressing the complexities of damage detection and localization in composite sandwich structures, offering a more precise and efficient strategy for structural health monitoring.

Table 4.3: First 5 non-null mode shapes for all types of damage.

Type of Damage	Mode 1	Mode 2	Mode 3	Mode 4	Mode 5
Undamaged	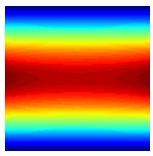	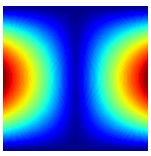	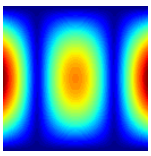	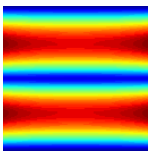	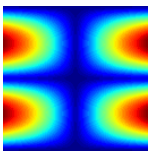
Core Damage	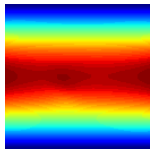	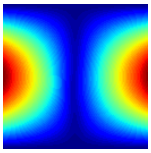	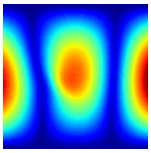	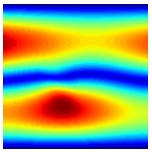	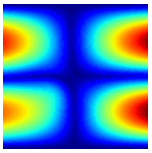
Skin Damage	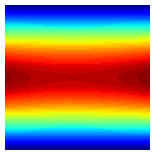	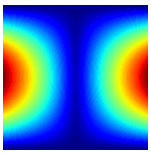	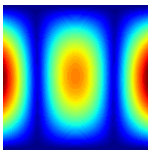	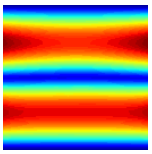	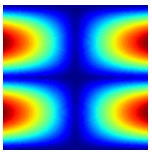
Interface Damage	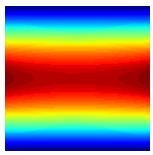	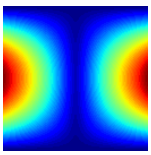	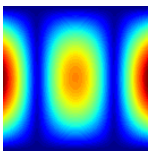	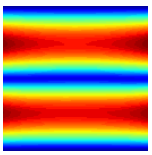	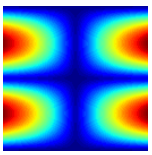

4.4.2 Detection network results

Table 4.4 presents the tuning results for the detection network. The filters in the convolutional layers showed substantial variation in values, highlighting the network's sensitivity to these hyperparameters. Similarly, the dropout layer exhibited significant variability, which is expected since it introduces noise into the processed image. Despite this, dropout remains crucial for preventing overfitting and improving the network's generalization capabilities.

Analyzing the learning rate and the number of neurons in the fully connected layers, we observe a preference for the values 256 and 10^{-4}, indicating that these parameters are probably globally optimized for this dataset. This observation suggests a direct relationship between the learning rate and the number of neurons, influencing the network's overall performance. Finally, the optimization yielded different values despite the dataset being similar for each case. This underscores the importance of Hyperparameter tuning to achieve a more precise and robust network. This fine-tuning of Hyperparameters enhances result accuracy and strengthens the network's ability to handle real-world variations and challenges.

Table 4.5 displays the detection report, providing detailed results of the detection process. This report includes three key metrics: Precision, Recall, and F1-score.

All methods exhibited strong performance in identifying patterns in both the undamaged model and the damaged model in the core. However, for damages in the skin and interface, the Wavelet method performed similarly to the original, while the Sobel and Laplace methods showed slight improvements. In contrast, the other methods performed

Table 4.4: Detection optimization

Detection						
Method	f1	f2	f3	drop	dense	lr ($\times 10^{-3}$)
Canny	64	64	128	0.075	256	0.5
Curvature	8	8	64	0.025	1024	1
Laplace	16	128	16	0.025	256	0.1
Residual	64	8	256	0.010	256	0.1
Residual Curvature	64	128	32	0.050	256	0.1
Sobel	16	32	32	0.010	256	0.1
Wavelet	8	32	32	0.010	256	0.1
Original	4	64	256	0.010	1024	0.5

poorly compared to the original model, with the residual method being the only one to achieve a significant enhancement. These findings highlight the complexities of damage identification, particularly in cases involving skin and interface damage.

To further analyze the detection results, a confusion matrix for the residual method was generated (Figure 4.3). The results indicate that the method performs almost perfectly for the core and undamaged cases. However, there remain some misidentification between the skin and interface defects.

Table 4.5: Detection test report for each method and damage type

Method	**Undamaged**			**Core**			**Skin**			**Interface**		
	Precision	Recall	F1-score	Precision	Recall	F1-score	Precision	Recall	F1-score	Precision	Recall	F1-score
Canny	0.97	1.00	0.98	0.97	0.96	0.97	0.64	0.44	0.52	0.61	0.79	0.69
Curvature	0.97	1.00	0.98	1.00	0.96	0.98	0.60	0.64	0.62	0.64	0.60	0.62
Laplace	0.97	1.00	0.97	0.99	0.97	0.98	0.76	0.76	0.76	0.79	0.79	0.79
Residual	0.99	1.00	0.99	1.00	0.99	0.99	0.84	0.91	0.87	0.92	0.84	0.87
Residual Curv.	0.97	1.00	0.99	0.99	0.98	0.98	0.80	0.32	0.46	0.58	0.92	0.71
Sobel	0.99	1.00	0.99	0.99	0.97	0.98	0.75	0.65	0.70	0.71	0.81	0.76
Wavelet	0.99	1.00	1.00	0.97	0.96	0.97	0.71	0.67	0.69	0.71	0.76	0.73
Original	0.97	1.00	0.98	1.00	0.97	0.98	0.75	0.64	0.69	0.69	0.79	0.73

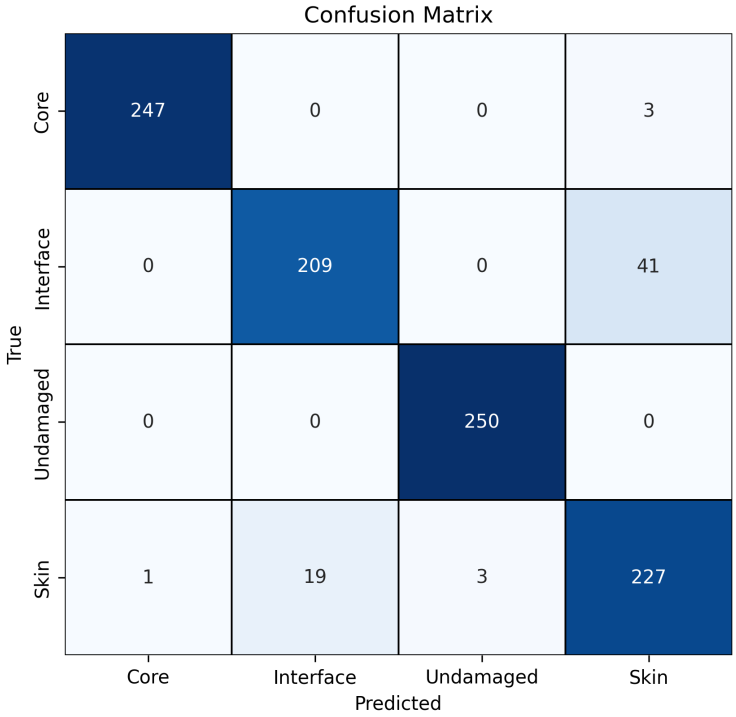

Figure 4.3: Residual Confusion Matrix

4.4.3 Damage localization network results

Our study defines damage through multiple parameters, including position, size, orientation, and extent. Despite rigorous identification efforts, the inherent complexity of the problem posed considerable challenges. Therefore, to determine the damage position, we rely exclusively on the residual model, which achieved the highest detection task performance.

After identifying the type of damage, we proceed with its localization. The localization model is divided into three distinct categories: core, interface, and skin. This segmentation ensures that data is routed to the appropriate model based on the detection results. To identify the damage, a customized optimization was performed for each parameter, with each head of the network handling a specific parameter (x, y, θ, r, and c). Additionally, a separate network was assigned to each type of damage (core, skin, and interface). As in the detection process, parameter optimization was conducted, but this time only for the residual method. The results of this optimization are presented in Table 4.6.

Analyzing the values, we observe that each parameter requires different configurations to achieve an optimized prediction. This highlights the importance of separating the parameters into distinct heads to obtain the best possible results.

The results obtained by the damage localization network are presented in Table 3.9. In general, the damage location process produced satisfactory results. We observed a mean absolute error maximum of 8.6 and 10.6 for the position parameters (x and y), considering the total size of the plate (250 mm), this equates to a percentage error of 3.4% and 4.2% respectively. Regarding shape parameters, the results are better for r and c but worse for θ. This underscores the need for further advances in AI methodologies and the development of more sophisticated models capable of handling such complex tasks.

Table 4.6: Damage localization optimization

Residual Core damage							
Parameter	f1	f2	f3	drop	d1	d2	lr ($\times 10^{-3}$)
X	16	16	256	0.025	128	512	0.1
Y	64	128	256	0.100	256	512	0.1
θ	8	32	128	0.010	32	32	0.5
r	32	64	32	0.025	512	512	1
c	4	8	16	0.010	32	32	0.5
Residual Skin damage							
Parameter	f1	f2	f3	drop	d1	d2	lr ($\times 10^{-3}$)
X	64	32	16	0.050	32	32	0.5
Y	64	8	256	0.075	64	32	0.5
θ	4	8	128	0.010	512	256	1
r	64	8	64	0.050	32	512	0.5
c	16	128	128	0.050	32	256	0.5
Residual Interface damage							
Parameter	f1	f2	f3	drop	d1	d2	lr ($\times 10^{-3}$)
X	64	128	128	0.050	128	256	0.1
Y	32	128	16	0.075	512	256	0.5
θ	4	8	64	0.010	256	256	1
r	4	128	64	0.010	32	256	0.5
c	8	128	256	0.075	64	32	0.5

Table 4.7: Damage localization optimization

Damage	X MAE	Y MAE	θ MAE	r MAE	c MAE
Core	5.3	6.3	35.0	0.065	6.8
Skin	8.6	10.6	46.0	0.075	7.1
Interface	6.1	8.8	41.4	0.074	7.6

To enhance our understanding of the damage localization network, we generated histograms of the residuals, allowing us to evaluate the model's performance based on the distribution of the residuals. The histogram of residuals shows that most residuals are concentrated around zero, indicating that the model generally makes accurate predictions. The high frequency at zero suggests many exact predictions. If the distribution is symmetric around zero, the model has little to no bias; otherwise, a skewed distribution could indicate a tendency to overestimate or underestimate. The presence of extreme residuals suggests occasional significant errors. Figure 4.4 shows the residual histograms for Core, Skin, and Interface damage localization.

To further contextualize the performance of our proposed damage localization network, we conducted a comparative analysis with a previously developed model, that is, a model without image processing (original mode shape image). This earlier study, based on a more traditional architecture and without the use of separate parameter heads or damage-specific networks, serves as a baseline for evaluating the improvements achieved in the current approach.

Table 4.8 presents the mean absolute errors for each parameter (x, y, θ, r, and c) across the three damage types: Core, Skin, and Interface. Overall, the residual-based

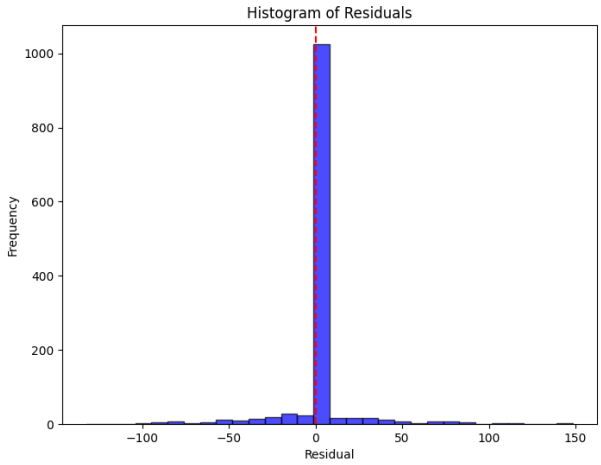

(a)

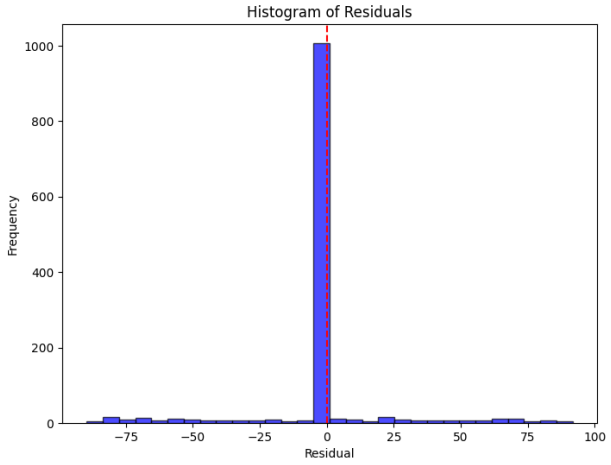

(b)

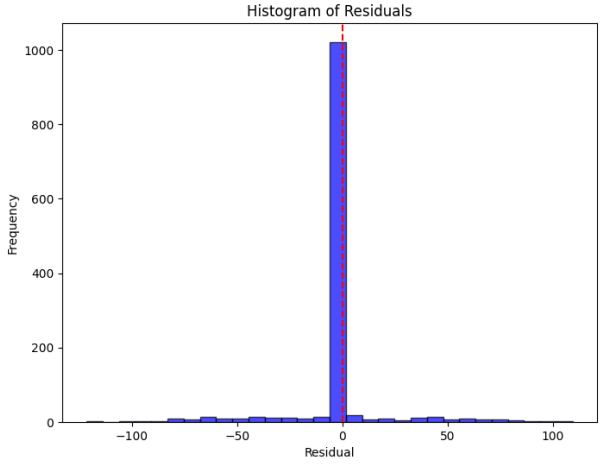

(c)

Figure 4.4: Residual histograms: (a) Core damage localization, (b) Skin damage localization, (c) Interface damage localization.

architecture consistently outperforms the Mode shape model across most parameters and damage types. The most notable improvements are observed in the spatial coordinates (x and y) and the component (r), where the new model shows reductions in error of over 30% in many cases. For instance, in Core damage localization, the x and r MAEs decreased by 35.4% and 29.4%, respectively, while y localization improved by 12.5%. In the case of Skin damage, improvements in x, y, and r were even more pronounced, reaching 31.2%, 19.1%, and 34.8%, respectively.

Table 4.8: Comparison of Residual-Based and Mode Shape Methods

Core damage localization					
Model	X MAE	Y MAE	θ MAE	r MAE	c MAE
Residual-based	5.3	6.3	35.0	0.065	6.8
Mode shape	8.2	7.2	32.8	0.092	6.9
Relative variation (%)	35.37%	12.5%	-6.71%	29.35%	1.45%
Skin damage localization					
Model	X MAE	Y MAE	θ MAE	r MAE	c MAE
Residual-based	8.6	10.6	46.0	0.075	7.1
Mode shape	12.5	13.1	45.9	0.115	8.8
Relative variation (%)	31.2%	19.08%	-0.22%	34.78%	19.32%
Interface damage localization					
Model	X MAE	Y MAE	θ MAE	r MAE	c MAE
Residual-based	6.1	8.8	41.4	0.074	7.6
Mode shape	9.5	8.5	46.2	0.189	11.0
Relative variation (%)	35.79%	-3.53%	10.39%	60.85%	30.91%

The benefits are even more evident in the Interface damage scenario, where the new model achieved a 60.9% reduction in the radial error (r), a 35.8% improvement in x, and 30.9% in the contact length (c). These results suggest that the tailored design of the model, with parameter-specific prediction heads, significantly enhances the accuracy in estimating geometrically sensitive components of damage localization.

In contrast, the angular parameter θ showed relatively small variations between the models across all damage types. In the Core and Skin cases, the difference was minimal (a relative variation of -6.7% and -0.2%, respectively), indicating that both architectures perform similarly in estimating this parameter. This suggests that θ may be less sensitive to architectural refinements, or that it is inherently more challenging to improve using the current strategy.

Interestingly, for the Interface damage case, the y parameter showed a slight increase in error in the new model (-3.5%), indicating a potential trade-off in certain conditions. However, this is outweighed by the substantial improvements in the other parameters.

Finally, Figures 4.5, 4.6, and 4.7 present a set of randomly selected damage localization predictions obtained using the Residual-based model and the Mode Shape model. The blue ellipses indicate the actual damage locations, while the red ellipses correspond to the predictions generated by the Residual-based model. The green circles represent the 95% confidence intervals associated with the expected damage positions predicted by the Mode Shape model. This visual comparison highlights the accuracy of the predicted damage locations while explicitly accounting for the inherent uncertainties in the model outputs, thereby providing a clearer assessment of the performance improvements achieved with respect to the previous model.

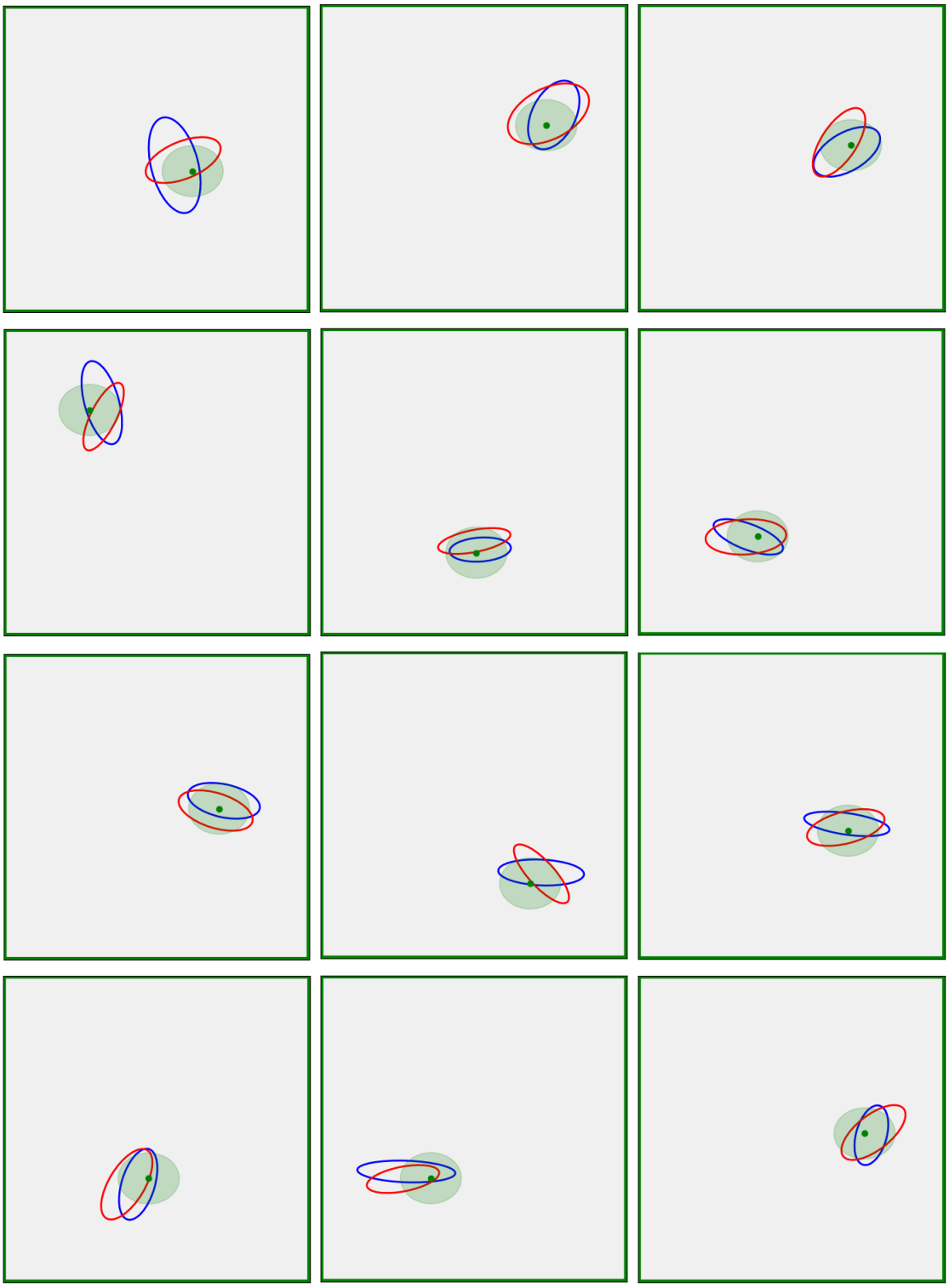

Figure 4.5: Core Damage location: Legend: ◯ Real damage ◯ Predicted damage (Residual-based) • Predicted position of the damage (Mode shape) ⊙ 95% confidence interval (Mode shape).

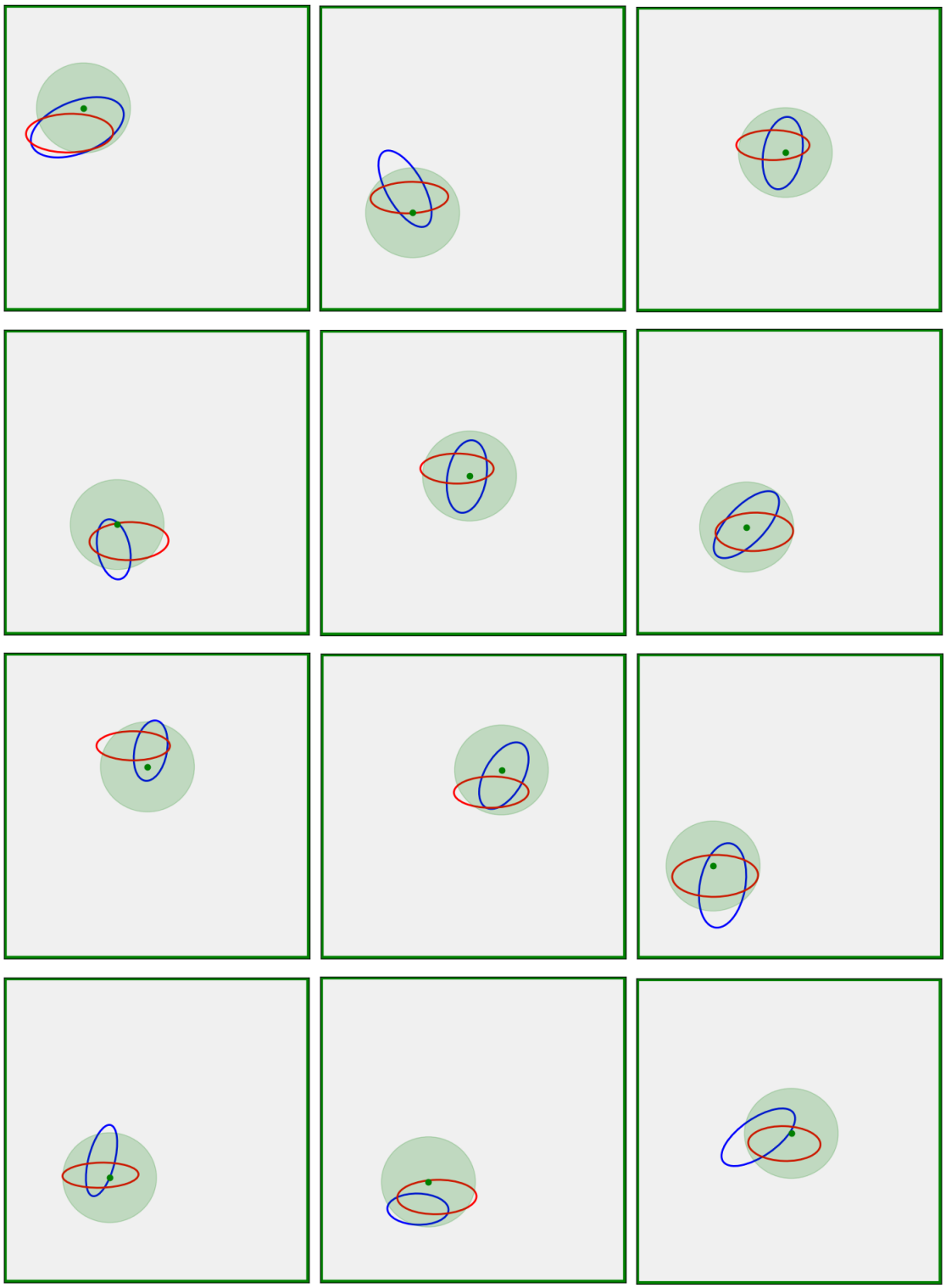

Figure 4.6: Skin Damage location: Legend: ◯ Real damage ◯ Predicted damage (Residual-based) • Predicted position of the damage (Mode shape) ⊙ 95% confidence interval (Mode shape).

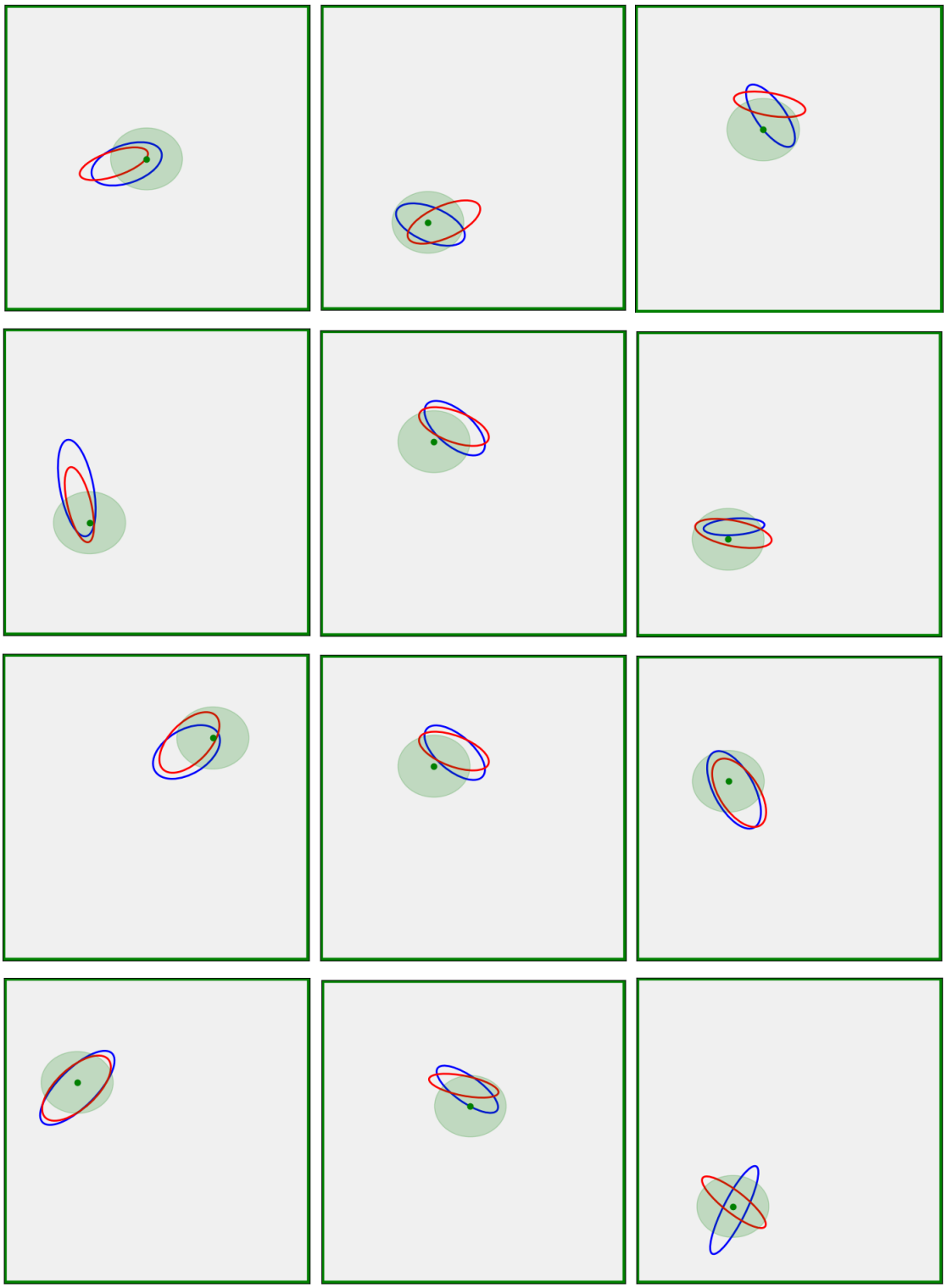

Figure 4.7: Inter Damage location: Legend: ◯ Real damage ◯ Predicted damage (Residual-based) • Predicted position of the damage (Mode shape) ⊙ 95% confidence interval (Mode shape).

4.5 Chapter Conclusion

This chapter proposed and evaluated an enhanced vibration-based damage identification framework that combines mode shape representations, image processing techniques, and Convolutional Neural Networks for damage detection and localization in composite sandwich structures. The approach employed the first five vibration mode shapes to identify damage into four categories—undamaged, core damage, skin damage, and interface damage—and a dedicated CNN for damage localization, predicting five parameters related to position (x, y) and shape (θ, r, and c).

The results demonstrated that the integration of image processing techniques significantly improves the performance of CNN-based damage identification models. Among the investigated methods, the residual technique consistently provided the highest accuracy for both damage detection and localization tasks. High detection accuracy was achieved for undamaged and core damage scenarios across all methods, while skin and interface damage remained more challenging to distinguish. Nevertheless, the residual-based approach exhibited superior performance in these cases, highlighting its ability to enhance damage-sensitive features in mode shape images.

Regarding damage localization, the proposed framework achieved low prediction errors for spatial parameters, with average errors of approximately 4% for the position coordinates (x, y). In contrast, the accurate estimation of the angular parameter θ proved to be more challenging, indicating a reduced sensitivity of the available modal information to damage orientation. This limitation reflects the inherent complexity of the problem and suggests the need for more advanced learning strategies capable of capturing subtle geometric variations.

A comparative analysis with a baseline damage localization model further confirmed the effectiveness of the proposed framework. By introducing parameter-specific prediction heads and damage-type specialization, the new architecture significantly reduced the mean absolute error for most predicted parameters, particularly for spatial localization (x, y) and radial extent (r), with improvements exceeding 30% in several cases. Although the prediction of the angular parameter θ remained relatively unchanged, the overall performance gains validate the benefits of architectural optimization guided by the physical characteristics of the damage.

Overall, the findings presented in this chapter demonstrate that combining mode shape information with residual-based image processing and tailored CNN architectures substantially enhances damage detection and localization capabilities in composite sandwich structures.

5 Damage Detection and Localization in Composite Plates Using Mode Shapes and Artificial Intelligence: From Numerical Models to Experimental Validation

This chapter builds upon the damage detection and localization framework developed in the previous chapters, while introducing a revised numerical methodology specifically adapted to the plate employed in the experimental campaign. Although the overall strategy continues to rely on vibration-based mode shapes and Convolutional Neural Networks, the numerical model was modified to accurately reproduce the geometry, boundary conditions, and material characteristics of the experimentally tested structure.

In contrast to earlier chapters, where the investigation was exclusively numerical, this chapter combines both numerical and experimental analyses. The numerical simulations are aligned with the experimental setup, enabling a consistent comparison between simulated and measured responses. The analysis is restricted to the fully clamped boundary condition and to the first five non-zero vibration modes, as these configurations proved to be the most reliable in previous studies and are also more representative of practical experimental limitations.

Furthermore, the learning framework is extended through refinements in the CNN architecture, supporting a more detailed characterization of damage. By integrating experimentally acquired data with an adapted numerical model, this chapter represents a critical step toward validating the proposed methodology under realistic testing conditions.

The chapter is organized as follows: Section 5.1 describes the experimental methodology, including the finite element model, experimental setup, and data acquisition using Digital Image Correlation. Section 5.2 presents and discusses the experimental results for both damage detection and localization tasks. Finally, Section 5.3 concludes the chapter by highlighting the main outcomes of the experimental validation.

5.1 Methodology

This section presents the methodology adopted in this study, which integrates numerical simulations and experimental validation with Convolutional Neural Networks for damage detection and localization in composite sandwich panels. Finite element models were developed to generate mode shape data under different damage scenarios and boundary conditions, which were used for network training. The trained models were subsequently validated using experimental vibration measurements obtained via Digital Image Correlation (DIC) on a corresponding composite panel. The methodology comprises data generation, preprocessing, CNN training, and performance evaluation, as summarized in

the flowchart shown in Figure 5.1.

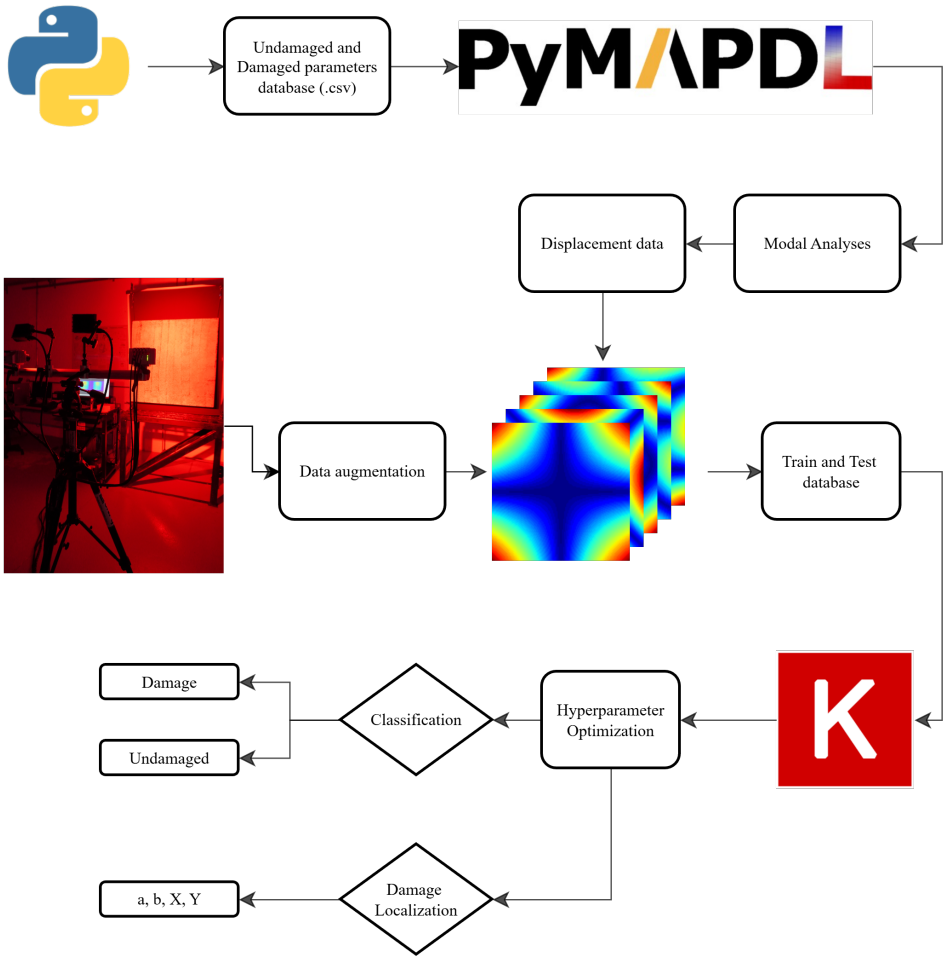

Figure 5.1: General methodology flowchart.

5.1.1 Finite Element Model

The composite plate was modeled using the SHELL181 element, which is suitable for laminated composite structures and allows accurate representation of bending and membrane behavior through layered shell sections. A symmetric quasi-isotropic laminate configuration was adopted, with individual plies defined by their thickness, material properties, and fiber orientations. Damage was numerically introduced by locally reducing the elastic properties of selected plies to represent Teflon inserts, simulating localized stiffness degradation while preserving the global structural configuration.

The plate was discretized using a structured quadrilateral mesh with a uniform element size of 10 mm, previously verified to provide stable modal characteristics within the frequency range of interest. Modal analysis was performed using the Block Lanczos algorithm to extract natural frequencies and mode shapes, with a consistent mass formulation. Although 20 modes were initially computed, only the first five non-null vibration modes were retained for analysis to ensure consistency with the experimental measurements obtained via Digital Image Correlation (DIC), which are limited in accuracy at

higher frequencies.

Two boundary condition scenarios were considered: a fully clamped configuration and a free–free configuration. These cases were selected to evaluate the influence of boundary conditions on the modal response and to maintain consistency with the experimental setups investigated in this study.

To better approximate real-world variability, stochastic variations in the material properties of the carbon fiber laminates and in the defect characteristics associated with the Teflon inserts are incorporated into the simulations. The ranges of the material parameters considered are summarized in Table 5.1. This strategy ensures that the training dataset captures realistic variability, thereby enhancing the robustness and generalization capability of the proposed deep learning framework.

All simulation routines were automated using Python through the PyAnsys ecosystem, specifically the PyMAPDL interface [134]. This integration enabled efficient model generation, batch execution, and post-processing of modal data, facilitating the generation of large datasets required for training the CNN models. In total, 500 simulations were performed for each damage scenario and boundary condition, resulting in a comprehensive dataset for the proposed methodology.

Table 5.1: Ranges of mechanical properties used for material modeling in simulations.

Material	**Property**	**Lower bound**	**Upper bound**
Carbon fiber	E_1 [GPa]	23	26
	E_2 [GPa]	7	10
	G_{12} [GPa]	4	5
	ρ_{CF} [kg/m^3]	1600	1700
Teflon (PTFE)	E [GPa]	0.40	0.80
	G [GPa]	0.15	0.30
	ρ_{PTFE} [kg/m^3]	2100	2200

Undamaged model

The undamaged model consists of a square composite plate with dimensions of 1×1 m^2, composed of sixteen unidirectional carbon fiber layers. The stacking sequence adopted for the laminate was $[0/45/-45/90]_4$, as illustrated in Figure 5.2. Each ply has a nominal thickness of 0.19 mm, resulting in a total laminate thickness of 3.04 mm.

In addition to the parameters varied in the parametric study, several properties were kept constant to ensure model consistency. In particular, Poisson's ratio (ν) was fixed at 0.2 for all simulations. The finite element mesh was refined to achieve an appropriate balance between numerical accuracy and computational efficiency, ensuring the convergence of the first five natural frequencies. Furthermore, the boundary conditions were defined to replicate the experimental configurations (fully clamped and free-free) adopted in the digital image correlation tests, thereby guaranteeing a direct comparison between numerical and experimental mode shapes.

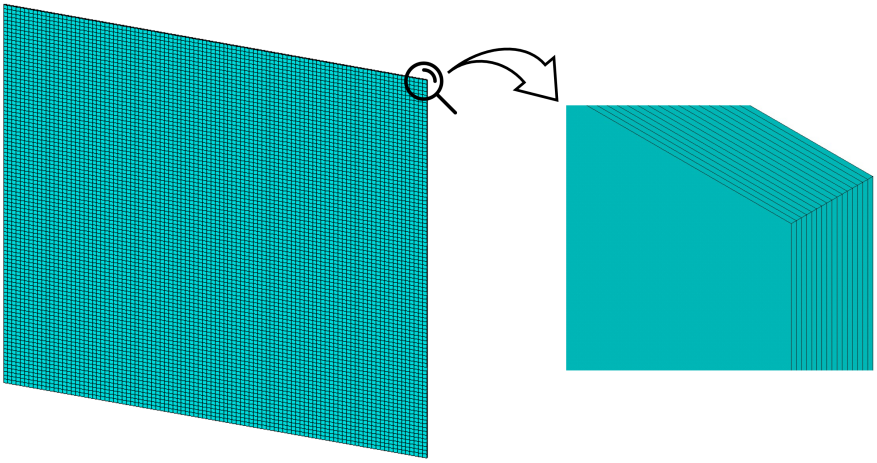

Figure 5.2: Numerical model in finite elements.

Damaged model

The damaged model was derived directly from the undamaged configuration, maintaining the same geometric and material setup. Four square defects were introduced in both the fourth and eighth plies, symmetrically distributed across the plate area. To emulate the experimental procedure, the material within each damaged area was replaced by polytetrafluoroethylene (PTFE), commonly known as Teflon, simulating the delamination effect observed in real composite structures.

The damage characteristics, including position and size, were parametrically varied for each simulation within predefined ranges, as summarized in Table 5.2. This systematic variation aimed to generate a representative dataset encompassing multiple damage scenarios for subsequent model training and validation. Figure 5.3 illustrates the main parameters of the damage configuration for clarity.

To illustrate the diversity of the simulated defect configurations used during the training stage, Figure 5.4 presents four examples of randomly generated damage layouts. These samples were obtained by independently sampling the geometric and positional parameters listed in Table 5.2, ensuring a wide variability in the shape, size, and distribution of the defect in the plate domain. Such variability is essential to promote generalization in data-driven models, enabling the CNN to learn representative patterns of delamination-like behavior rather than overfitting to specific defect arrangements.

Table 5.2: Ranges of damage design variables used to parameterize defect geometry and position.

Parameter	**Description**	**Lower bound [mm]**	**Upper bound [mm]**
a	Defect width	6.35	25.4
b	Defect height	6.35	25.4
$X_{1,5}$	X coordinate of defects 1 and 5	150	250
$X_{2,6}$	X coordinate of defects 2 and 6	350	450
$X_{3,7}$	X coordinate of defects 3 and 7	550	650
$X_{4,8}$	X coordinate of defects 4 and 8	750	850
$Y_{1–4}$	Y coordinate of defects 1–4	150	250
$Y_{5–8}$	Y coordinate of defects 5–8	750	850

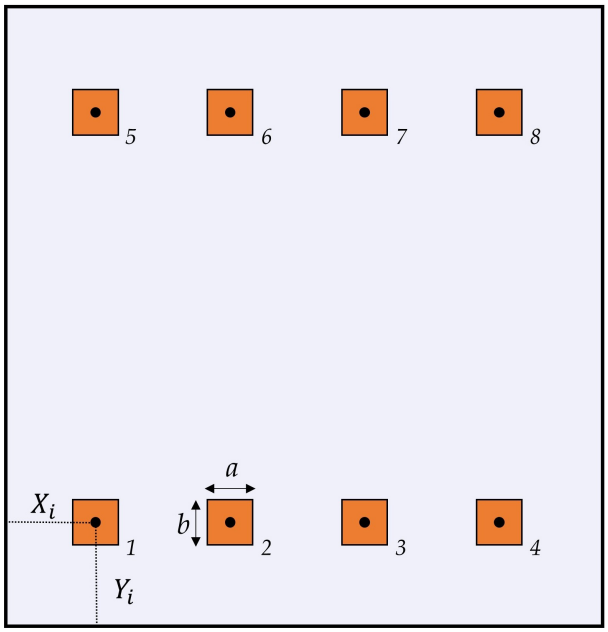

Figure 5.3: Damage defect geometry and position parametrization.

5.1.2 Experimental Procedure

The experimental plate was manufactured with the same geometry, material system, and stacking sequence as those adopted in the numerical model. Artificial defects were introduced in the form of Teflon (PTFE) inserts embedded between selected laminate layers to emulate interlaminar delamination. This approach provides a controlled and repeatable representation of internal damage commonly observed in composite structures.

The size and spatial distribution of the embedded defects were defined a priori and carefully controlled during the manufacturing process. A total of eight rectangular defects with dimensions $a \times b$ were introduced at specific in-plane coordinates (X, Y) measured from the lower-left corner of the plate. The detailed geometric characteristics and locations of the artificial defects are summarized in Table 5.3. The defect sizes were systematically increased along the X direction and symmetrically distributed along two horizontal lines at $Y = 200$ mm and $Y = 800$ mm, allowing the experimental assessment of damage detectability and localization performance over a wide range of defect dimensions and positions. The relative size and in-plane location of the embedded defects can also be visually identified in Figure 5.5(a).

To measure the displacement fields, a Digital Image Correlation system was employed. This non-contact optical technique provides full-field deformation measurements by tracking the motion of a random speckle pattern applied to the specimen surface. Before testing, the plate surface was coated with a uniform matte white base layer and subsequently sprayed with a fine black speckle pattern to produce the high-contrast random texture required for accurate DIC correlation. Figures 5.5(a) and 5.5(b) show the plate before and after speckle pattern application, respectively.

Two distinct boundary condition configurations were experimentally investigated, in direct correspondence with the numerical simulations: a free–free configuration and a fully clamped configuration. The adoption of both setups allowed the evaluation of the influence of boundary conditions on the modal response and ensured consistency between numerical and experimental analyses.

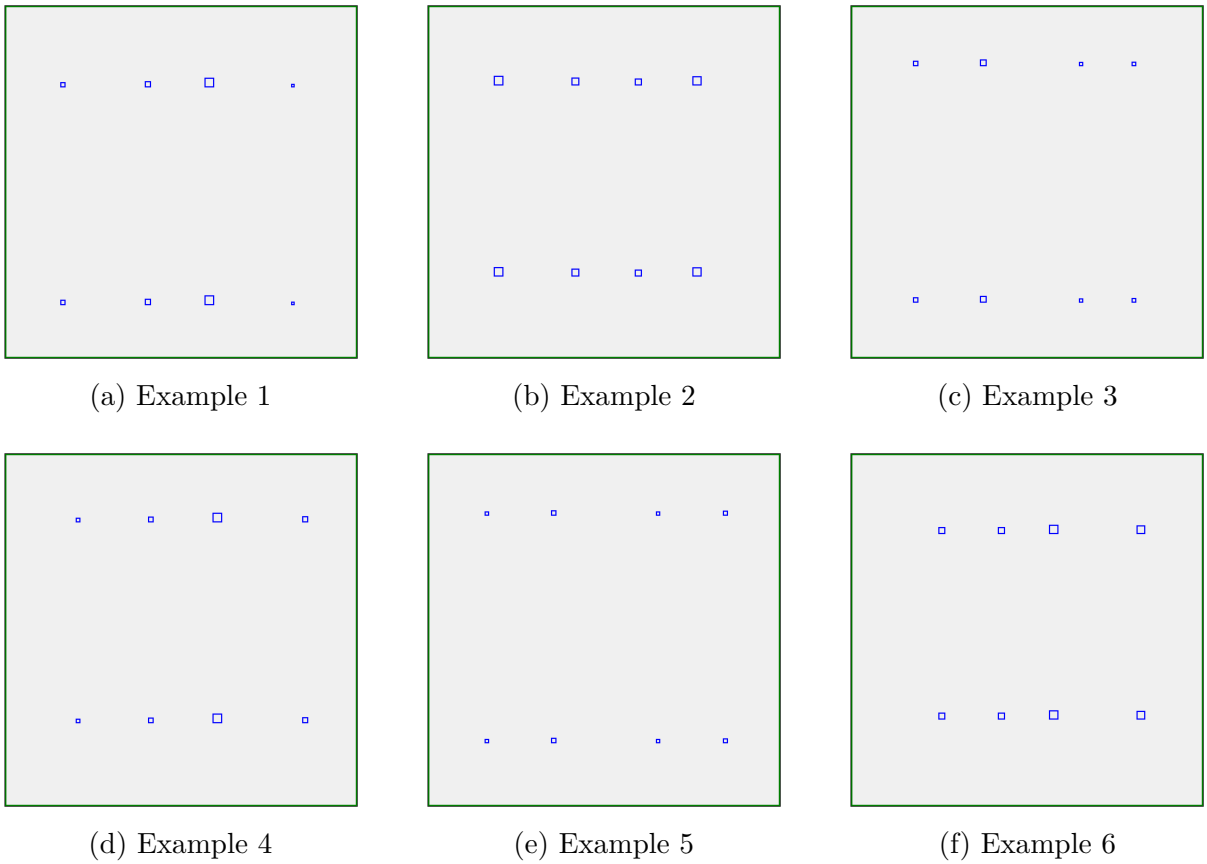

(a) Example 1 (b) Example 2 (c) Example 3

(d) Example 4 (e) Example 5 (f) Example 6

Figure 5.4: Examples of randomly sampled damage configurations used during the training stage. Each subplot corresponds to a combination obtained by sampling the parameters listed in Table 5.2.

Table 5.3: Geometric characteristics and in-plane coordinates of the artificial defects embedded in the experimental composite plate.

Damage ID	X **[mm]**	Y **[mm]**	a **[mm]**	b **[mm]**
1	200	200	6.35	6.35
2	400	200	12.70	12.70
3	600	200	19.05	19.05
4	800	200	25.40	25.40
5	200	800	6.35	6.35
6	400	800	12.70	12.70
7	600	800	19.05	19.05
8	800	800	25.40	25.40

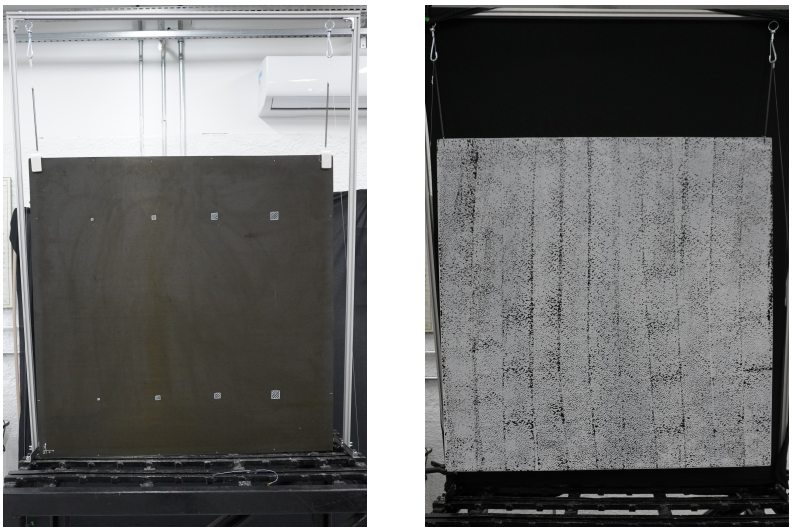

(a) Plate before speckle pattern application.

(b) Plate after speckle pattern application for DIC.

Figure 5.5: Surface preparation for Digital Image Correlation.

In the free–free configuration, the plate was suspended using a system of elastic springs combined with counterweights, designed to approximate unconstrained boundary conditions. This arrangement minimized stiffness and damping effects introduced by the supports, allowing the plate to vibrate with negligible external constraints within the frequency range of interest. Figure 5.6(a) illustrates the experimental setup used to achieve the free–free condition.

In the fully clamped configuration, the plate was rigidly fixed along the edges using a specially designed mechanical support that provided a fully constrained boundary condition. All translational and rotational degrees of freedom were suppressed at the clamped region, closely reproducing the idealized clamped condition adopted in the finite element model. The clamping device was designed to ensure uniform pressure distribution and to prevent local slippage or partial constraint effects. The experimental arrangement for the clamped condition is shown in Figure 5.6(b).

The DIC system consisted of a pair of synchronized high-speed cameras configured for stereoscopic acquisition, enabling three-dimensional displacement field reconstruction. The cameras were calibrated using a precision checkerboard target to determine intrinsic and extrinsic parameters, ensuring sub-pixel accuracy in the correlation process. Image acquisition was performed at 637 frames per second (fps), which, according to the Nyquist theorem, allows reliable measurement of dynamic responses up to approximately 318 Hz. This frequency range adequately covers the first several natural frequencies of the composite plate. Each frame was recorded at a spatial resolution sufficient to capture the entire plate surface with a high density of correlation points.

The excitation was applied using a Rigol DG822 Pro function generator driving an electrodynamic shaker through a swept-sine signal ranging from 1 Hz to 300 Hz. The excitation signal was continuously monitored using a digital oscilloscope (Rigol DS924) to ensure amplitude consistency and waveform quality. Figure 5.7(b) presents the time-domain representation of the applied swept-sine signal, illustrating the progressive frequency increase used to excite the structural modes within the frequency range of interest. This excitation strategy ensured adequate energy input across the entire bandwidth

(a) Free–free boundary condition detail.

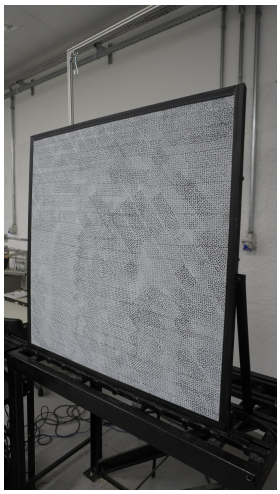

(b) Fully clamped boundary condition detail.

Figure 5.6: Experimental setups used to reproduce the boundary conditions adopted in the numerical model.

while avoiding bias toward specific frequency bands, which is essential for reliable modal identification using DIC measurements.

Additionally, two structural configurations were considered: an undamaged plate and a plate with artificially introduced defects, positioned identically to those adopted in the numerical model. For the free–free boundary condition, both intact and damaged configurations were experimentally tested, allowing a direct comparison of their modal responses. In contrast, for the fully clamped boundary condition, only the damaged configuration was experimentally investigated.

For all tested cases, the DIC system provided nodal coordinates (x, y, z) and displacement components (u, v, w) associated with the extracted vibration modes. The overall experimental configuration, including the DIC-based measurement system, the electrodynamic shaker, and the applied excitation signal, is shown in Figure 5.7.

5.1.3 Contour Plot and Comparative Analysis

The displacement data obtained both numerically and experimentally were converted into visual representations through contour plots. These plots provide two-dimensional projections of the mode shapes, where contour lines connect points of equal displacement magnitude. The nodal coordinates (x, y) were combined with the displacement vector magnitude computed from the three components (u, v, w) on the upper surface of the plate. Linear interpolation was applied between grid points to generate smooth and continuous color maps. All images were standardized in resolution and scale to ensure uniform comparison during CNN processing.

Figures 5.8 and 5.9 present the first five non-zero mode shapes obtained from the numerical model and experimental measurements, respectively, for the free–free boundary condition. A clear correlation is observed between the simulated and measured mode shapes, indicating that the finite element model accurately reproduces the dynamic behavior of the composite plate under unconstrained conditions.

For the fully clamped boundary condition, the corresponding numerical and experi-

(a) Experimental setup for modal testing using DIC and electrodynamic shaker.

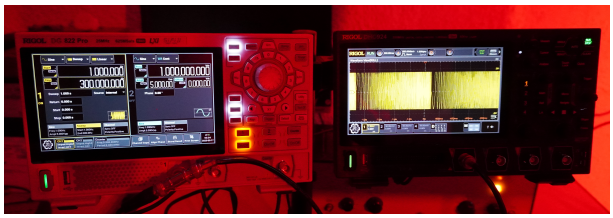

(b) Time-domain representation of the swept-sine excitation signal monitored using a digital oscilloscope.

Figure 5.7: Experimental configuration adopted in the modal tests: (a) DIC-based measurement system combined with an electrodynamic shaker, and (b) swept-sine excitation signal applied during the experiments.

mental mode shapes were processed following the same visualization and normalization procedures. The resulting contour plots, shown in Figure 5.10 and Figure 5.11, illustrate the first non-zero vibration modes of the plate under clamped constraints, highlighting the influence of boundary conditions on the spatial distribution and curvature of the modal shapes.

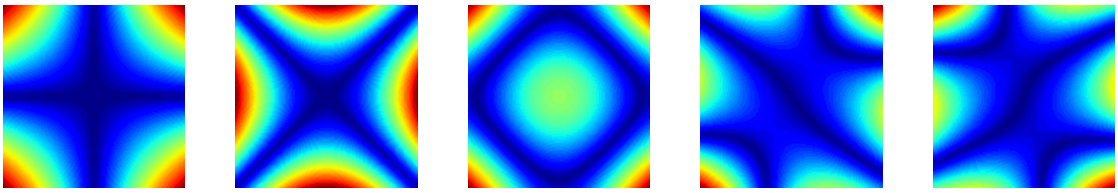

(a) 1st (b) 2nd (c) 3rd (d) 4th (e) 5th

Figure 5.8: First five non-zero mode shapes obtained from the numerical model (free-free).

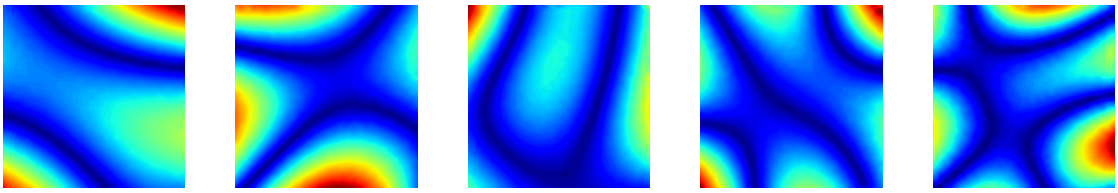

(a) 1st (b) 2nd (c) 3rd (d) 4th (e) 5th

Figure 5.9: First five non-zero experimental mode shapes (free-free).

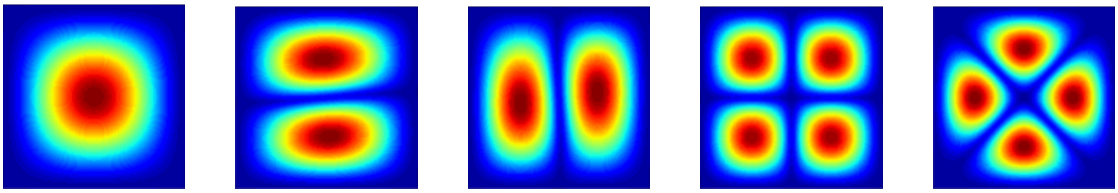

(a) 1st (b) 2nd (c) 3rd (d) 4th (e) 5th

Figure 5.10: First five non-zero mode shapes obtained from the numerical model (fully clamped).

A quantitative and qualitative comparison between the numerical and experimental mode shapes reveals a strong overall agreement, as summarized in Tables 5.4 and 5.5. For the free–free boundary condition, the first vibration mode exhibits the largest discrepancy, with an error of approximately 19%. This deviation is primarily attributed to experimental factors, including slight imperfections in the realization of the boundary condition, minor variations in plate positioning, and inherent limitations of the DIC system in accurately capturing very low-frequency responses.

Apart from this initial discrepancy, the remaining free–free modes exhibit substantially improved agreement. Modes 2 and 3 present errors below 8%, while modes 4 and 5 show an excellent match in terms of both natural frequencies and spatial mode shape distributions, as illustrated in Figures 5.8 and 5.9. These results confirm that the finite element model accurately reproduces the dynamic behavior of the composite plate under unconstrained conditions.

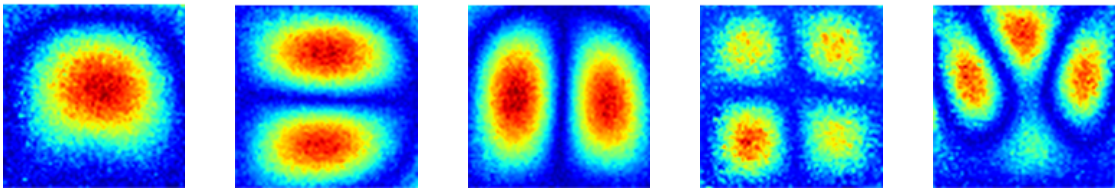

(a) 1st (b) 2nd (c) 3rd (d) 4th (e) 5th

Figure 5.11: First five non-zero experimental mode shapes (fully clamped).

For the fully clamped boundary condition, the numerical and experimental results also demonstrate good agreement across all evaluated vibration modes. Frequency discrepancies remain below 15% in all cases and below 8% for most modes, indicating that the numerical model effectively captures the increased stiffness imposed by the clamped constraint. Additionally, the experimental mode shapes obtained under fully clamped conditions exhibit higher noise levels compared to those measured in the free-free configuration. This behavior is primarily attributed to experimental constraints at the clamping interface and to the higher natural frequencies involved, which lead to reduced vibration amplitudes and, consequently, a lower signal-to-noise ratio in the DIC measurements. As a result, although the overall modal patterns remain consistent with the numerical predictions, the experimental contour maps for the clamped condition appear less smooth.

Overall, the combined analysis of natural frequencies and mode shape distributions demonstrates that the numerical model provides a reliable representation of the experimental configurations for both boundary conditions, supporting its suitability for subsequent analyses and neural network training.

Table 5.4: Comparison between numerical and experimental natural frequencies for the free–free boundary condition.

Mode	**Numerical (Hz)**	**Experimental (Hz)**	**Difference (%)**
1	11.05	13.69	19.3
2	21.16	22.82	7.3
3	30.74	29.20	5.3
4	37.33	36.50	2.3
5	69.18	69.36	0.3

Table 5.5: Comparison between numerical and experimental natural frequencies for the fully clamped boundary condition.

Mode	**Numerical (Hz)**	**Experimental (Hz)**	**Difference (%)**
1	30.42	26.63	14.2
2	44.22	41.54	6.5
3	55.71	54.33	2.5
4	67.87	72.43	6.3
5	90.70	84.15	7.8

5.1.4 Data Augmentation

Since each experimental condition provided only a single displacement field per vibration mode, a data augmentation procedure was implemented to increase dataset variability and improve the robustness of the convolutional neural network (CNN). The augmentation was applied directly to the displacement field obtained from the Digital Image Correlation (DIC) system.

For each measured point on the plate surface, the DIC acquisition provides the spatial coordinates (x_i, y_i) together with the corresponding displacement components in the in-plane and out-of-plane directions, namely $u_x(x_i, y_i)$, $u_y(x_i, y_i)$, and $u_z(x_i, y_i)$. Thus, the displacement vector at each location is defined as

$$u(x_i, y_i) = \Big(u_x(x_i, y_i),\, u_y(x_i, y_i),\, u_z(x_i, y_i)\Big) \tag{5.1}$$

The scalar displacement magnitude is obtained from the Euclidean norm of this vector,

$$u_{\text{mag}} = \sqrt{u_x^2 + u_y^2 + u_z^2} \tag{5.2}$$

To normalize the displacement field to the interval $[-1, 1]$, the following transformation is applied:

$$\tilde{u} = 2\,\frac{u_{\text{mag}} - u_{\min}}{u_{\max} - u_{\min}} - 1 \tag{5.3}$$

To emulate variability in excitation intensity and boundary conditions, the normalized field is multiplied by a random scale factor

$$\alpha \sim \mathcal{U}(0.8,\, 1.2) \tag{5.4}$$

resulting in the perturbed displacement field

$$u_\alpha = \alpha\,\tilde{u} \tag{5.5}$$

Measurement uncertainty, typically observed in DIC systems, is reproduced by adding uncorrelated Gaussian noise,

$$\eta(x_i, y_i) \sim \mathcal{N}(0,\, \sigma^2), \qquad \sigma = 0.05 \tag{5.6}$$

leading to the augmented displacement field

$$u_{\text{aug}} = u_\alpha + \eta(x_i, y_i). \tag{5.7}$$

The augmented data are then interpolated onto a regular rectangular grid using a Radial Basis Function (RBF) interpolator with smoothing parameter $s = 0.01$. The resulting continuous displacement field is expressed as

$$\hat{u}(x, y) = \sum_{i=1}^{N} w_i\,\phi(\|(x, y) - (x_i, y_i)\|) \tag{5.8}$$

where $\phi(\cdot)$ denotes the radial basis kernel and w_i are the coefficients determined from the augmented samples.

Finally, the interpolated field $\hat{u}(x, y)$ is rendered as a contour map. For each original displacement measurement, 25 augmented images are generated for each condition, forming the dataset used for CNN evaluation.

Data augmentation techniques were applied to improve model robustness and reduce overfitting, including small spatial perturbations, amplitude normalization, and controlled noise injection. These transformations were carefully selected to preserve the physical characteristics of the mode shapes while introducing variability consistent with experimental measurements. This augmentation strategy was designed to mimic realistic measurement uncertainty rather than artificially inflate the dataset.

5.1.5 Convolutional Neural Network Model

Convolutional Neural Networks were developed to analyze mode shape images for damage detection and localization in composite plates. For each vibration mode, 500 numerically generated images were used for training and 25 experimentally acquired images for testing, resulting in 2,500 training images and 125 testing images per scenario and boundary condition, considering five vibration modes.

Two CNN models were implemented: one for binary damage detection (damaged or undamaged) and another for damage localization, formulated as a regression task to predict the spatial coordinates and size of the defect. Both models shared the same base architecture, differing only in their output layers and loss functions. For damage localization, separate networks were trained for the free–free and fully clamped boundary conditions to account for differences in modal behavior.

The network architecture consists of three convolutional layers, each followed by pooling and dropout layers for feature extraction and regularization, followed by two fully connected dense layers. ReLU activation was used throughout the network, while Softmax and linear activations were applied to the output layers for detection and regression tasks, respectively. Training was performed using the Adam optimizer with an early stopping strategy to ensure efficient convergence.

A multi-head CNN architecture was adopted, with each head independently processing the mode shape image of a specific vibration mode. The features extracted from all heads were concatenated and used for the final prediction, allowing the network to jointly exploit complementary information from multiple vibration modes and improving robustness to noise and experimental variability.

5.2 Results and Discussion

This section presents and discusses the results obtained from the proposed convolutional neural network models. The outcomes of the Bayesian-based hyperparameter optimization are reported within the respective subsections for detection and regression analyses. The first part examines the performance of the binary detection model, which distinguishes between damaged and undamaged conditions using mode shape images. The subsequent part evaluates the regression-based damage localization model by comparing the predicted and actual damage positions and sizes, with the analysis conducted separately for the free–free and fully clamped boundary conditions.

5.2.1 Detection Network Results

The detection model was initially trained using the optimal hyperparameters identified through Bayesian optimization. These included 256 filters in the first convolutional layer, 64 filters in the second convolutional layer, 8 filters in the third convolutional layer, a dropout rate of 0.01, 32 neurons in the first dense layer, 256 neurons in the second dense layer, and a learning rate of 1×10^{-2}. The Adam optimizer was used for training, with an early stopping criterion based on validation accuracy, terminating training after 25 epochs without improvement to prevent overfitting.

The training and evaluation procedure consisted of two sequential stages. In the first stage, the network was trained exclusively on simulated data. The dataset was divided into training (80%) and validation (20%) subsets to assess the network's performance on

unseen samples. Table 5.6 summarizes the detection metrics obtained on the validation subset of simulated data. The network achieved perfect scores across Precision, Recall, and F1-score, confirming that it successfully captured the distinguishing patterns present in the simulated dataset. Nevertheless, it should be noted that simulated data do not fully represent the variability and imperfections observed in experimental measurements.

Table 5.6: Report for damage detection using simulated data.

Class	**Precision**	**Recall**	**F1-score**	**Support**
Undamaged	1.00	1.00	1.00	100
Damaged	1.00	1.00	1.00	100
Accuracy			1.00	200
Macro Avg	1.00	1.00	1.00	200
Weighted Avg	1.00	1.00	1.00	200

In the second stage, the trained model was evaluated using experimental data, which were augmented to increase variability and enhance robustness. Table 5.7 presents the corresponding classification report, and Figure 5.12 illustrates the confusion matrix for this experimental validation.

Table 5.7: Report for damage detection using experimental data.

Class	**Precision**	**Recall**	**F1-score**	**Support**
Undamaged	0.83	1.00	0.91	25
Damaged	1.00	0.80	0.89	25
Accuracy			0.90	50
Macro Avg	0.92	0.90	0.90	50
Weighted Avg	0.92	0.90	0.90	50

From Table 5.7, it can be observed that the network achieved high performance on the experimental dataset, with an overall accuracy of 90%. The small discrepancies among Precision, Recall, and F1-score arise from the uneven distribution of predictions across the two classes. Precision represents the proportion of correct positive predictions among all positive predictions, Recall measures the proportion of correctly identified positives among all actual positives, and F1-score is the harmonic mean of Precision and Recall. The slightly lower Recall for the Damaged class (0.80) indicates that a few damaged samples were misidentified as undamaged, while the perfect Precision (1.00) shows that every predicted damaged sample was indeed correct. This implies that, although the model may miss some damage instances, its positive predictions are highly reliable.

Overall, these results demonstrate that the CNN model generalizes well from simulated to experimental data. Despite the inherent variability in real-world measurements, the network maintained strong detection performance, achieving over 90% accuracy. This highlights the robustness and practical applicability of the proposed architecture for damage detection in composite sandwich structures.

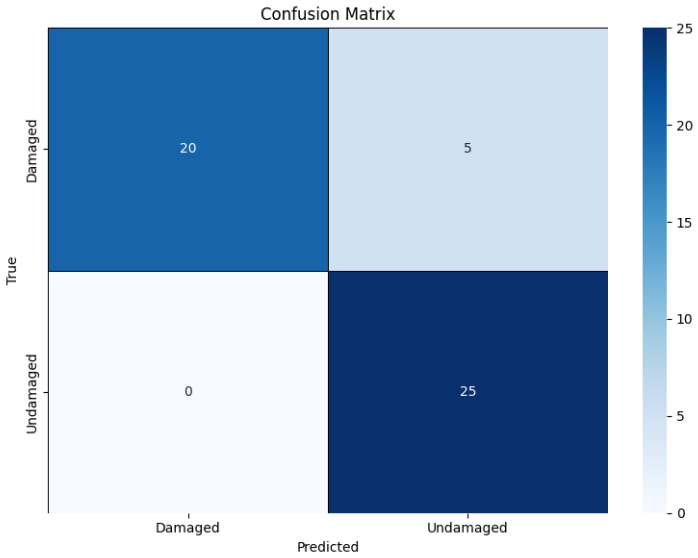

Figure 5.12: Confusion matrix for experimental validation with data augmentation.

5.2.2 Damage Localization Network Results

The damage localization models were trained using optimal hyperparameters obtained through Bayesian optimization, which was performed independently for each boundary condition. Consequently, distinct network configurations were selected for the free–free and fully clamped cases, reflecting the different dynamic characteristics associated with each structural constraint.

For the free–free boundary condition, the optimal architecture consisted of 128 filters in the first convolutional layer, 128 filters in the second convolutional layer, and 4 filters in the third convolutional layer. A dropout rate of 0.1 was applied, and the network was trained using a learning rate of 1×10^{-3}. The fully connected stage comprised 1024 neurons in the first dense layer and 256 neurons in the second dense layer.

In contrast, the fully clamped boundary condition required a deeper and more expressive network to adequately capture the increased modal complexity induced by the boundary constraints. Bayesian optimization selected an architecture with 512 filters in the first convolutional layer, 128 filters in the second convolutional layer, and 256 filters in the third convolutional layer. The dropout rate was maintained at 0.1; however, a higher learning rate of 1×10^{-2} was found to be optimal. The dense layers were expanded to 2048 and 512 neurons, respectively, enabling improved feature abstraction and representation capacity.

Similar to the detection task, the evaluation of the damage localization models was conducted in two stages. First, the models were trained using numerically simulated data, adopting an 80/20 split between training and validation subsets. The Adam optimizer was employed, and early stopping based on the Mean Absolute Error (MAE) was applied to prevent overfitting.

Table 5.8 presents the MAE values for the predicted damage parameters under the free–free boundary condition. The results demonstrate that the network accurately predicts the damage location, as evidenced by the consistently low errors in the X and Y coordinates across most damage scenarios. The estimation of damage size parameters (a and b) exhibits comparatively higher errors, particularly for smaller defects. This behavior suggests a reduced sensitivity of low-frequency free–free modes to subtle variations in

damage extent, which primarily affects size-related predictions rather than localization accuracy.

The corresponding results for the fully clamped boundary condition are summarized in Table 5.9. Despite the increased stiffness and altered modal distribution introduced by the clamped constraint, the model maintains a strong capability to localize damage, with low position errors observed across the evaluated cases. A slightly higher variability is observed in the estimation of the damage size parameters when compared to the free–free case. This behavior is attributed not only to the higher modal frequencies and increased mode shape complexity associated with the clamped configuration, but also to the presence of noise in the vibration modes, which can affect the stability and spatial resolution of the extracted features. Such factors may mildly reduce the robustness of damage extent estimation.

In the second stage, the trained damage localization models were applied to experimental data containing real defects, allowing an assessment of their generalization capability from numerically simulated data to real measurements. The analysis was conducted separately for the free–free and fully clamped boundary conditions, in direct correspondence with the numerical and experimental setups previously described.

For the free–free configuration, Table 5.10 and Figure 5.13(a) present the comparison between the true and predicted damage parameters. The results indicate that the network accurately estimates the damage location for all tested cases, with very small deviations in the predicted X and Y coordinates. The prediction of damage size parameters (a and b) shows increased variability for smaller defects, which is consistent with the reduced sensitivity of low-frequency free–free modes to subtle changes in damage extent.

The corresponding results for the fully clamped boundary condition are reported in Table 5.11 and Figure 5.13(b). Despite the higher modal frequencies and increased complexity of the mode shapes associated with the clamped constraint, the model maintains a reliable capability to localize damage. While size estimation exhibits slightly larger deviations compared to the free–free case, the predicted parameters remain physically consistent with the true defect characteristics.

While Tables 5.10 and 5.11 provide a detailed, case-by-case comparison between true and predicted damage parameters, a more compact and normalized assessment is required to directly compare the overall performance of the proposed framework under different boundary conditions. For this purpose, Table 5.12 summarizes the mean absolute errors of the predicted damage parameters obtained from experimental data for both free–free and fully clamped configurations.

The consolidated results indicate that damage localization accuracy remains consistently high for both boundary conditions, with comparable mean errors in the X direction. The free–free configuration exhibits lower overall errors, particularly in the Y coordinate and in the estimation of damage size parameters (a and b). In contrast, the fully clamped condition presents increased uncertainty in both spatial localization and size estimation, which is attributed to higher modal frequencies, increased mode shape complexity, and reduced displacement amplitudes. Nevertheless, the observed errors remain limited and correspond to less than 1% of the plate characteristic length, confirming the robustness of the proposed approach under varying boundary constraints.

Overall, the results indicate that tailoring the network architecture to the boundary condition is essential for achieving optimal performance. While both configurations exhibit high accuracy in damage localization, the fully clamped condition demands a more expressive model to compensate for its more complex dynamic response. These findings highlight the importance of boundary-condition-aware model design in data-driven

structural health monitoring frameworks.

Table 5.8: Mean Absolute Error for predicted damage parameters under free–free boundary condition.

Targets	**MAE x**	**MAE a**	**MAE b**	**MAE y**	**MAE global**
x_1, a_1, b_1, y_1	7.924	8.929	1.219	1.802	4.969
x_2, a_2, b_2, y_1	0.104	4.174	2.084	0.593	1.739
x_3, a_3, b_3, y_1	1.446	2.313	2.268	0.242	1.567
x_4, a_4, b_4, y_1	0.020	8.833	9.270	1.017	4.785
x_1, a_1, b_1, y_2	1.351	8.992	8.825	0.675	4.961
x_2, a_2, b_2, y_2	0.823	2.977	2.138	0.211	1.537
x_3, a_3, b_3, y_2	0.252	2.461	2.571	0.231	1.379
x_4, a_4, b_4, y_2	0.628	7.883	8.922	0.398	4.458

Table 5.9: Mean Absolute Error for predicted damage parameters under fully clamped boundary condition.

Targets	**MAE x**	**MAE a**	**MAE b**	**MAE y**	**MAE global**
x_1, a_1, b_1, y_1	3.389	7.896	8.983	4.674	6.235
x_2, a_2, b_2, y_2	0.643	2.945	2.512	7.546	3.411
x_3, a_3, b_3, y_3	0.646	4.916	4.992	4.795	3.837
x_4, a_4, b_4, y_4	3.015	7.640	5.499	0.915	4.267
x_5, a_5, b_5, y_5	1.574	10.164	10.473	5.415	6.907
x_6, a_6, b_6, y_6	2.496	1.524	4.331	3.306	2.914
x_7, a_7, b_7, y_7	0.520	2.862	5.523	1.063	2.375
x_8, a_8, b_8, y_8	4.561	1.909	0.130	2.396	2.220

In the second stage, the trained damage localization models were applied to experimental data containing real defects, allowing an assessment of their generalization capability from numerically simulated data to real measurements. The analysis was conducted separately for the free–free and fully clamped boundary conditions, in direct correspondence with the numerical and experimental setups previously described.

For the free–free configuration, Table 5.10 and Figure 5.13(a) present the comparison between the true and predicted damage parameters. The results indicate that the network accurately estimates the damage location for all tested cases, with very small deviations in the predicted X and Y coordinates. The prediction of damage size parameters (a and b) shows increased variability for smaller defects, which is consistent with the reduced sensitivity of low-frequency free–free modes to subtle changes in damage extent.

The corresponding results for the fully clamped boundary condition are reported in Table 5.11 and Figure 5.13(b). Despite the higher modal frequencies and increased complexity of the mode shapes associated with the clamped constraint, the model maintains a reliable capability to localize damage. While size estimation exhibits slightly larger

deviations compared to the free–free case, the predicted parameters remain physically consistent with the true defect characteristics.

Overall, the strong agreement between predicted and actual damage locations for both boundary conditions confirms the robustness of the proposed approach and demonstrates its ability to transfer knowledge from numerical simulations to experimental measurements under different structural constraints.

Table 5.10: Comparison between real and predicted damage parameters using experimental data under free–free boundary conditions.

Defect	**X true**	**a true**	**b true**	**Y true**	**X pred**	**a pred**	**b pred**	**Y pred**
1	200.000	6.350	6.350	200.000	206.583	9.141	7.354	200.619
2	400.000	12.700	12.700	200.000	400.710	12.549	12.383	201.280
3	600.000	19.050	19.050	200.000	599.625	19.942	17.138	200.238
4	800.000	25.400	25.400	200.000	803.015	17.760	19.901	200.915
5	200.000	6.350	6.350	800.000	201.880	11.787	12.275	801.035
6	400.000	12.700	12.700	800.000	399.865	14.865	13.563	800.396
7	600.000	19.050	19.050	800.000	599.674	20.025	18.449	800.223
8	800.000	25.400	25.400	800.000	795.439	23.491	25.387	802.396

Table 5.11: Comparison between real and predicted damage parameters using experimental data under fully clamped boundary conditions.

Defect	**X true**	**a true**	**b true**	**Y true**	**X pred**	**a pred**	**b pred**	**Y pred**
1	200.000	6.350	6.350	200.000	196.610	14.250	15.330	204.670
2	400.000	12.700	12.700	200.000	400.640	15.640	15.210	207.550
3	600.000	19.050	19.050	200.000	600.650	14.130	14.060	204.800
4	800.000	25.400	25.400	200.000	803.020	17.760	19.900	200.920
5	200.000	6.350	6.350	800.000	201.570	16.510	16.820	794.580
6	400.000	12.700	12.700	800.000	397.500	14.220	17.030	796.690
7	600.000	19.050	19.050	800.000	599.950	16.190	13.530	798.940
8	800.000	25.400	25.400	800.000	795.440	23.490	25.390	802.400

In summary, these findings indicate that the CNN model trained solely on simulated data can accurately predict both the position and size of real damages. While the estimation of small defect sizes remains less precise, the model consistently captures the correct damage location and general magnitude across all cases. This demonstrates the proposed network's capability to transfer learned spatial features from simulation to real-world conditions, reinforcing its potential for practical structural health monitoring applications in composite sandwich structures.

Table 5.12: Mean Absolute Error (MAE) of predicted damage parameters obtained from experimental data for different boundary conditions.

Boundary condition	**MAE X**	**MAE Y**	**MAE a**	**MAE b**
Free-Free	2.80	0.89	4.79	4.51
Clamped	2.30	4.33	6.40	6.28

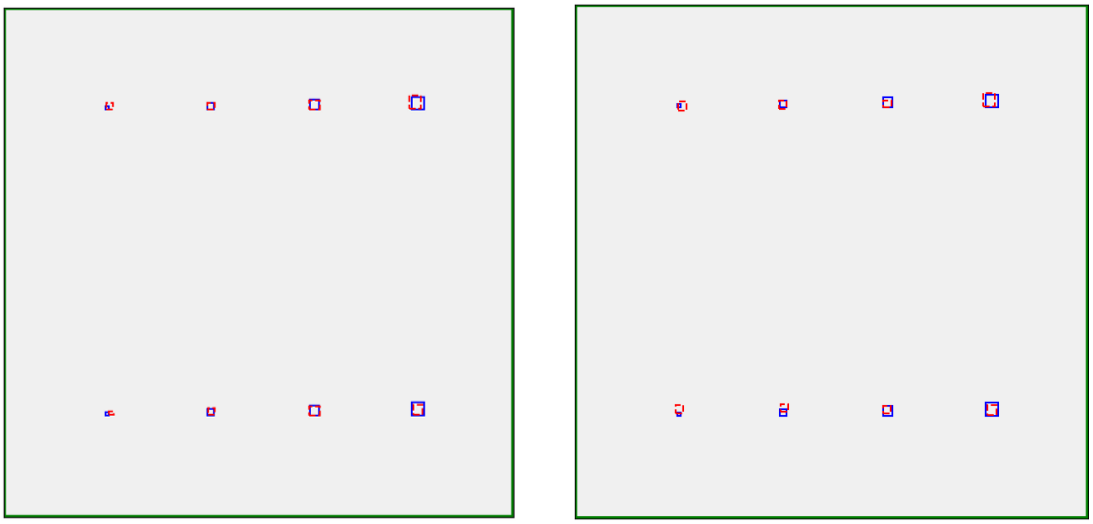

(a) Damage localization results using experimental data under free–free boundary conditions.

(b) Damage localization results using experimental data under fully clamped boundary conditions.

Figure 5.13: Comparison between predicted and actual damage parameters obtained from experimental measurements for different boundary conditions. Predicted values are shown in red, while actual values are shown in blue.

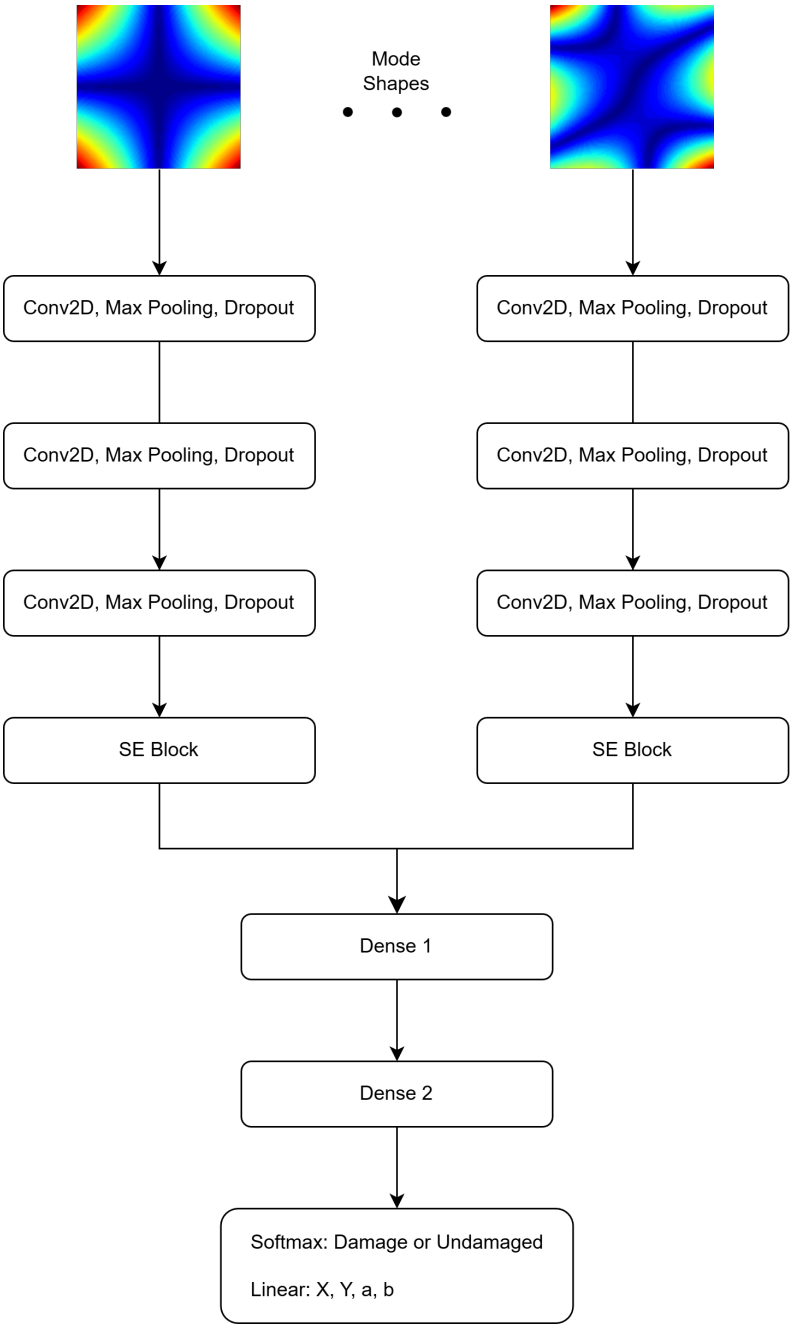

Figure 5.14: Schematic representation of the proposed multi-head CNN architecture. Each vibration mode shape image is processed by an independent convolutional head. The extracted features are concatenated and fed into fully connected layers for damage detection or localization.

5.3 Chapter Conclusion

This chapter presented a simulation-driven deep learning framework for vibration-based damage detection and localization in composite sandwich structures using mode shape images. Convolutional Neural Networks were trained exclusively on numerically generated data and subsequently validated using experimental measurements obtained through Digital Image Correlation, to bridge the gap between numerical modeling and real-world structural behavior.

The proposed methodology demonstrated strong performance in both damage detection and localization tasks. The detection model successfully distinguished between damaged and undamaged structural conditions, while the regression-based models accurately estimated damage location and size, even when evaluated using experimental data not included in the training process. These results confirm that mode shape images contain rich spatial information that can be effectively exploited by CNNs to capture damage-induced stiffness variations in composite sandwich structures.

A key contribution of this study lies in the explicit assessment of model generalization under different boundary condition scenarios, namely free-free and fully clamped configurations. Despite the significant influence of boundary conditions on the modal response, the proposed framework exhibited robust performance across both cases, demonstrating its ability to handle variability in structural constraints commonly encountered in experimental and operational environments.

The analysis was intentionally restricted to the first five vibration modes to ensure consistency between numerical and experimental datasets, reflecting practical limitations associated with DIC-based measurements at higher frequencies. Although this constraint limits the available modal information, the selected modes proved sufficient to achieve reliable damage localization, reinforcing the effectiveness of the proposed approach under realistic measurement conditions.

Overall, the findings presented in this chapter demonstrate that deep learning models trained exclusively on simulated data can be successfully transferred to experimental applications, provided that appropriate data representations and preprocessing strategies are employed. This significantly reduces the dependence on large experimental datasets, which are often costly and difficult to obtain for composite structures, and represents an important step toward the practical deployment of data-driven SHM systems.

6 General Conclusion

This thesis proposed and validated a comprehensive and intelligent Structural Health Monitoring framework for the detection, localization, and sizing of damage in composite sandwich structures. By integrating vibration-based mode shape analysis, advanced image processing techniques, Digital Image Correlation, and Convolutional Neural Networks, the proposed methodology addressed key challenges associated with composite materials, whose damage mechanisms are often internal, barely visible, and difficult to detect using conventional inspection techniques.

A systematic review of machine learning approaches applied to damage assessment in composite structures was conducted, enabling the identification of prevailing trends, methodological limitations, and open research challenges. This analysis revealed a notable lack of methodologies capable of simultaneously identifying multiple damage mechanisms while accurately localizing their spatial position and estimating their dimensions under varying boundary conditions. These gaps directly motivated the development of the proposed framework and strongly influenced its methodological design.

Numerical investigations demonstrated that vibration mode shapes contain rich spatial information that is highly sensitive to localized stiffness variations associated with damage occurring in skins, cores, and interfaces. By transforming mode shape data into image-based representations and coupling them with Convolutional Neural Networks, the proposed approach successfully learned complex damage-related patterns without the need for handcrafted feature extraction. The use of simulation-driven datasets proved to be an effective strategy, significantly reducing the dependence on extensive experimental campaigns while maintaining high predictive accuracy.

Several image processing strategies were investigated to further enhance damage sensitivity and robustness, including residual-based representations, curvature enhancement, edge detection, and wavelet transforms. The results demonstrated that appropriate preprocessing can substantially improve both identification performance and localization accuracy, particularly in cases involving small or barely perceptible damage. In addition, the incorporation of attention mechanisms contributed to improved feature discrimination and enhanced the generalization capability of the learning models.

Experimental validation using Digital Image Correlation confirmed the practical applicability of the proposed framework. The investigated damage was introduced in a controlled and repeatable manner by inserting a lower-stiffness material within the laminate, creating a localized stiffness-reduction region representative of internal debonding or delamination-type defects. Despite the presence of measurement noise, experimental uncertainty, and discrepancies between numerical simulations and experimental data, the models demonstrated strong generalization capability. Accurate damage detection, precise spatial localization, and reliable estimation of damage size were achieved under different boundary conditions.

It is important to emphasize that acquiring high-quality experimental datasets for vibration-based SHM in composite structures is inherently challenging. Digital Image Correlation requires careful surface preparation, speckle pattern optimization, high-resolution cameras, controlled illumination, and precise synchronization with excitation systems. Furthermore, validating multiple damage scenarios demanded the manufacturing and

testing of several specimens with controlled stiffness-reduction regions, significantly increasing experimental time, complexity, and cost. These practical constraints reinforce the relevance of simulation-driven learning strategies and highlight the importance of methodologies capable of generalizing from limited experimental data.

From a physical perspective, the effectiveness of the proposed framework can be explained by the way damage alters the local stiffness distribution of composite structures. While global modal parameters are primarily governed by the overall balance between mass and stiffness, localized defects manifest as spatial irregularities in displacement fields and strain energy distribution. These local perturbations are more accurately captured by vibration mode shapes, which explains the superior performance of mode shape-based approaches for damage localization and sizing.

The transformation of mode shapes into image-based representations allowed the damage identification problem to be reformulated as a spatial pattern recognition task. In this context, Convolutional Neural Networks act not merely as numerical identifiers, but as hierarchical feature extractors capable of capturing subtle spatial correlations, symmetry losses, and localized gradients associated with structural damage. Image processing techniques such as residual representations and curvature enhancement further amplified these physically meaningful features by suppressing dominant global deformation patterns and emphasizing local stiffness discontinuities.

Conversely, the limited performance observed for certain preprocessing strategies highlights that not all transformations preserve physically relevant damage information. Methods that excessively amplify noise or rely solely on edge-based features were shown to be less robust under experimental conditions, particularly in the presence of measurement uncertainty. This finding underscores the importance of combining data-driven learning with physically informed data representations, rather than relying exclusively on either paradigm in isolation.

Overall, the results obtained in this thesis demonstrate that the integration of vibration-based mode shape analysis, physically informed image processing techniques, and deep learning constitutes a powerful and flexible solution for damage assessment in composite sandwich structures. The main scientific advancement of this work lies in demonstrating that internal stiffness-reduction damage can be not only detected and identified, but also accurately localized and dimensioned under real experimental conditions using vibration-based measurements. This contribution bridges the gap between simulation-driven learning strategies and practical SHM implementation, representing a significant step toward intelligent, automated, and reliable Structural Health Monitoring systems capable of supporting condition-based maintenance strategies and enhancing the safety, durability, and operational efficiency of composite structures in engineering applications.

The main scientific contributions of this doctoral research can be summarized as follows:

- Development of a unified vibration-based Structural Health Monitoring framework capable of detecting, identifying, localizing, and estimating the size of controlled stiffness-reduction damage in composite sandwich structures using mode shape images and deep learning.

- Experimental demonstration that simulation-trained Convolutional Neural Networks can successfully generalize to full-field Digital Image Correlation measurements, enabling accurate localization and dimensioning of internal damage despite measurement noise and domain discrepancies.

- Introduction of a controlled experimental damage methodology based on the insertion of lower-stiffness material to simulate internal debonding, providing a repeatable and physically representative benchmark for SHM validation.
- Systematic evaluation of image processing techniques and attention mechanisms to enhance damage-sensitive features and improve the robustness and accuracy of deep learning-based damage identification models under varying boundary conditions.

Although the proposed methodology demonstrated promising results, several directions for future research remain. These include extending the framework to more complex geometries and loading conditions, incorporating environmental and operational variability, and exploring physics-informed or hybrid learning strategies to further enhance robustness and interpretability. In addition, real-time implementation and scalability to large-scale structures represent important challenges and opportunities for future investigation.

Bibliography

[1] Ribeiro Junior, R. F. and Gomes, G. F., "On the use of machine learning for damage assessment in composite structures: A review," *Applied Composite Materials*, vol. 31, no. 1, pp. 1–37, 2024.

[2] Barile, C., Casavola, C., Pappalettera, G., and Kannan, V. P., "Damage monitoring of carbon fibre reinforced polymer composites using acoustic emission technique and deep learning," *Composite Structures*, vol. 292, p. 115 629, 2022.

[3] Chung, D. D., *Composite materials: science and applications*. Springer Science & Business Media, 2010.

[4] Khan, A., Ko, D.-K., Lim, S. C., and Kim, H. S., "Structural vibration-based classification and prediction of delamination in smart composite laminates using deep learning neural network," *Composites Part B: Engineering*, vol. 161, pp. 586–594, 2019.

[5] Bortoluzzi, D. B., Diniz, C. A., Pereira, J. L. J., Junior, R. F. R., Gomes, G. F., and Junior, A. C. A., "On the influence of rectangular z-pins parameters on mode ii delamination resistance of through the thickness reinforced composites," *Composite Structures*, vol. 305, p. 116 509, 2023.

[6] Demircan, G., Ozen, M., Kisa, M., Acikgoz, A., and Işıker, Y., "The effect of nano-gelcoat on freeze-thaw resistance of glass fiber-reinforced polymer composite for marine applications," *Ocean Engineering*, vol. 269, p. 113 589, 2023.

[7] Elmarakbi, A., *Advanced composite materials for automotive applications: Structural integrity and crashworthiness*. John Wiley & Sons, 2013.

[8] Uddin, N., *Developments in fiber-reinforced polymer (FRP) composites for civil engineering*. Elsevier, 2013.

[9] Jafari-Talookolaei, R.-A., "Analytical solution for the free vibration characteristics of the rotating composite beams with a delamination," *Aerospace Science and Technology*, vol. 45, pp. 346–358, 2015.

[10] Zhang, Z. et al., "Vibration-based assessment of delaminations in frp composite plates," *Composites Part B: Engineering*, vol. 144, pp. 254–266, 2018.

[11] Gomes, G. F., Junior, R. F. R., Pereira, J. L. J., and Francisco, M. B., "An efficient deep learning model to predict the structural response of cfrp isogrid tubes," *Composite Structures*, vol. 316, p. 117 043, 2023.

[12] Sun, G., Wang, Y., Luo, Q., and Li, Q., "Vibration-based damage identification in composite plates using 3d-dic and wavelet analysis," *Mechanical Systems and Signal Processing*, vol. 173, p. 108 890, 2022.

[13] Meruane, V., Aichele, D., Ruiz, R., and López Droguett, E., "A deep learning framework for damage assessment of composite sandwich structures," *Shock and Vibration*, vol. 2021, no. 1, p. 1 483 594, 2021.

[14] Miller, B. and Ziemiański, L., "Detection of material degradation of a composite cylinder using mode shapes and convolutional neural networks," *Materials*, vol. 14, no. 21, p. 6686, 2021.

[15] Zhong, K., Teng, S., Liu, G., Chen, G., and Cui, F., "Structural damage features extracted by convolutional neural networks from mode shapes," *Applied Sciences*, vol. 10, no. 12, p. 4247, 2020.

[16] Polimeno, U., Meo, M., Almond, D., and Angioni, S., "Detecting low velocity impact damage in composite plate using nonlinear acoustic/ultrasound methods," *Applied Composite Materials*, vol. 17, no. 5, pp. 481–488, 2010.

[17] Yu, B., Blanc, R., Soutis, C., and Withers, P., "Evolution of damage during the fatigue of 3d woven glass-fibre reinforced composites subjected to tension–tension loading observed by time-lapse x-ray tomography," *Composites Part A: Applied Science and Manufacturing*, vol. 82, pp. 279–290, 2016.

[18] Saeedifar, M. and Zarouchas, D., "Damage characterization of laminated composites using acoustic emission: A review," *Composites Part B: Engineering*, vol. 195, p. 108 039, 2020.

[19] Leng, J. and Asundi, A., "Structural health monitoring of smart composite materials by using efpi and fbg sensors," *Sensors and Actuators A: Physical*, vol. 103, no. 3, pp. 330–340, 2003.

[20] De Luca, A., Perfetto, D., De Fenza, A., Petrone, G., and Caputo, F., "Guided wave shm system for damage detection in complex composite structure," *Theoretical and Applied Fracture Mechanics*, vol. 105, p. 102 408, 2020.

[21] Bandara, S., Herath, M., and Epaarachchi, J., "Sensory methods and machine learning based damage identification of fibre-reinforced composite structures: An introductory review," *Journal of Reinforced Plastics and Composites*, vol. 42, no. 21-22, pp. 1119–1146, 2023.

[22] Nasiri, S. and Khosravani, M. R., "Applications of data-driven approaches in prediction of fatigue and fracture," *Materials Today Communications*, vol. 33, p. 104 437, 2022.

[23] Goyal, D. and Pabla, B., "The vibration monitoring methods and signal processing techniques for structural health monitoring: A review," *Archives of Computational Methods in Engineering*, vol. 23, pp. 585–594, 2016.

[24] Miller, B. and Ziemiański, L., "Identification of mode shapes of a composite cylinder using convolutional neural networks," *Materials*, vol. 14, no. 11, p. 2801, 2021.

[25] Ozdagli, A. I. and Koutsoukos, X., "Machine learning based novelty detection using modal analysis," *Computer-Aided Civil and Infrastructure Engineering*, vol. 34, no. 12, pp. 1119–1140, 2019.

[26] Hou, R. and Xia, Y., "Review on the new development of vibration-based damage identification for civil engineering structures: 2010–2019," *Journal of Sound and Vibration*, vol. 491, p. 115 741, 2021.

[27] Tabian, I., Fu, H., and Sharif Khodaei, Z., "A convolutional neural network for impact detection and characterization of complex composite structures," *Sensors*, vol. 19, no. 22, p. 4933, 2019.

[28] Azuara, G., Ruiz, M., and Barrera, E., "Damage localization in composite plates using wavelet transform and 2-d convolutional neural networks," *Sensors*, vol. 21, no. 17, p. 5825, 2021.

[29] Wang, Y., Luo, Q., Xie, H., Li, Q., and Sun, G., "Digital image correlation (dic) based damage detection for cfrp laminates by using machine learning based image semantic segmentation," *International Journal of Mechanical Sciences*, vol. 230, p. 107 529, 2022.

[30] Maghami, A., Salehi, M., and Khoshdarregi, M., "Automated vision-based inspection of drilled cfrp composites using multi-light imaging and deep learning," *CIRP Journal of Manufacturing Science and Technology*, vol. 35, pp. 441–453, 2021.

[31] Azimi, M., Eslamlou, A. D., and Pekcan, G., "Data-driven structural health monitoring and damage detection through deep learning: State-of-the-art review," *Sensors*, vol. 20, no. 10, p. 2778, 2020.

[32] Nasiri, S. and Khosravani, M. R., "Machine learning in predicting mechanical behavior of additively manufactured parts," *Journal of materials research and technology*, vol. 14, pp. 1137–1153, 2021.

[33] Sutton, R. S. and Barto, A. G., *Reinforcement learning: An introduction*. MIT press, 2018.

[34] Khan, A., Kim, N., Shin, J. K., Kim, H. S., and Youn, B. D., "Damage assessment of smart composite structures via machine learning: A review," *JMST Advances*, vol. 1, no. 1, pp. 107–124, 2019.

[35] Avci, O., Abdeljaber, O., Kiranyaz, S., Hussein, M., Gabbouj, M., and Inman, D. J., "A review of vibration-based damage detection in civil structures: From traditional methods to machine learning and deep learning applications," *Mechanical systems and signal processing*, vol. 147, p. 107 077, 2021.

[36] Dayhoff, J. E. and DeLeo, J. M., "Artificial neural networks: Opening the black box," *Cancer: Interdisciplinary International Journal of the American Cancer Society*, vol. 91, no. S8, pp. 1615–1635, 2001.

[37] Ribeiro Junior, R. F., Almeida, F. A. de, and Gomes, G. F., "Fault classification in three-phase motors based on vibration signal analysis and artificial neural networks," *Neural Computing and Applications*, vol. 32, no. 18, pp. 15 171–15 189, 2020.

[38] Wang, X. and Makis, V., "Autoregressive model-based gear shaft fault diagnosis using the kolmogorov–smirnov test," *Journal of Sound and Vibration*, vol. 327, no. 3-5, pp. 413–423, 2009.

[39] Akaike, H., "Autoregressive model fitting for control," in *Selected Papers of Hirotugu Akaike*, Springer, 1998, pp. 153–170.

[40] Regis, M., Serra, P., and Heuvel, E. R. van den, "Random autoregressive models: A structured overview," *Econometric Reviews*, vol. 41, no. 2, pp. 207–230, 2022.

[41] John, G. H. and Langley, P., "Estimating continuous distributions in bayesian classifiers," *arXiv preprint arXiv:1302.4964*, 2013.

[42] Keogh, E. J. and Pazzani, M. J., "Learning the structure of augmented bayesian classifiers," *International Journal on Artificial Intelligence Tools*, vol. 11, no. 04, pp. 587–601, 2002.

[43] Langley, P. and Sage, S., "Induction of selective bayesian classifiers," in *Uncertainty Proceedings 1994*, Elsevier, 1994, pp. 399–406.

[44] Bielza, C. and Larranaga, P., "Discrete bayesian network classifiers: A survey," *ACM Computing Surveys (CSUR)*, vol. 47, no. 1, pp. 1–43, 2014.

[45] LeCun, Y., Bengio, Y., et al., "Convolutional networks for images, speech, and time series," *The handbook of brain theory and neural networks*, vol. 3361, no. 10, p. 1995, 1995.

[46] Li, Z., Liu, F., Yang, W., Peng, S., and Zhou, J., "A survey of convolutional neural networks: Analysis, applications, and prospects," *IEEE transactions on neural networks and learning systems*, 2021.

[47] Ribeiro Junior, R. F., Santos Areias, I. A. dos, Campos, M. M., Teixeira, C. E., Silva, L. E. B. da, and Gomes, G. F., "Fault detection and diagnosis in electric motors using convolution neural network and short-time fourier transform," *Journal of Vibration Engineering & Technologies*, vol. 10, no. 7, pp. 2531–2542, 2022.

[48] Junior, R. F. R., Santos Areias, I. A. dos, Campos, M. M., Teixeira, C. E., Silva, L. E. B. da, and Gomes, G. F., "Fault detection and diagnosis in electric motors using 1d convolutional neural networks with multi-channel vibration signals," *Measurement*, vol. 190, p. 110 759, 2022.

[49] Gangwar, A. K., Mahela, O. P., Rathore, B., Khan, B., Alhelou, H. H., and Siano, P., "A novel k-means clustering and weighted k-nn-regression-based fast transmission line protection," *IEEE Transactions on Industrial Informatics*, vol. 17, no. 9, pp. 6034–6043, 2020.

[50] Kumar, D. and Fet, D., "Performance analysis of various data mining algorithms: A review," *International Journal of Computer Applications*, vol. 32, no. 6, pp. 9–16, 2011.

[51] Karegowda, A. G., Jayaram, M., and Manjunath, A., "Cascading k-means clustering and k-nearest neighbor classifier for categorization of diabetic patients," *International Journal of Engineering and Advanced Technology*, vol. 1, no. 3, pp. 147–151, 2012.

[52] Richardson, M., "Principal component analysis," *URL: http://people. maths. ox. ac. uk/richardsonm/SignalProcPCA. pdf (last access: 3.5. 2013). Aleš Hladnik Dr., Ass. Prof., Chair of Information and Graphic Arts Technology, Faculty of Natural Sciences and Engineering, University of Ljubljana, Slovenia ales. hladnik@ ntf. uni-lj. si*, vol. 6, p. 16, 2009.

[53] Abdi, H. and Williams, L. J., "Principal component analysis," *Wiley interdisciplinary reviews: computational statistics*, vol. 2, no. 4, pp. 433–459, 2010.

[54] Teixeira, C. E. et al., "An ultrasound-based water-cut meter for heavy fuel oil," *Measurement*, vol. 148, p. 106 907, 2019.

[55] Mammone, A., Turchi, M., and Cristianini, N., "Support vector machines," *Wiley Interdisciplinary Reviews: Computational Statistics*, vol. 1, no. 3, pp. 283–289, 2009.

[56] Wang, L., *Support vector machines: theory and applications*. Springer Science & Business Media, 2005, vol. 177.

[57] Dioşan, L., Rogozan, A., and Pecuchet, J.-P., "Improving classification performance of support vector machine by genetically optimising kernel shape and hyperparameters," *Applied Intelligence*, vol. 36, no. 2, pp. 280–294, 2012.

[58] García-Gonzalo, E., Fernández-Muñiz, Z., García Nieto, P. J., Bernardo Sánchez, A., and Menéndez Fernández, M., "Hard-rock stability analysis for span design in entry-type excavations with learning classifiers," *Materials*, vol. 9, no. 7, p. 531, 2016.

[59] Qing, X., Liao, Y., Wang, Y., Chen, B., Zhang, F., and Wang, Y., "Machine learning based quantitative damage monitoring of composite structure," *International Journal of Smart and Nano Materials*, vol. 13, no. 2, pp. 167–202, 2022.

[60] Ramasamy, P. and Sampathkumar, S., "Prediction of impact damage tolerance of drop impacted wgfrp composite by artificial neural network using acoustic emission parameters," *Composites Part B: Engineering*, vol. 60, pp. 457–462, 2014.

[61] Ramasamy, P. and Sampathkumar, S., "Offline and online investigation of drop impact damage on gfrp composite using non-destructive data by artificial neural network," *Iranian Journal of Science and Technology. Transactions of Mechanical Engineering*, vol. 39, no. M1, p. 29, 2015.

[62] Khatir, S., Tiachacht, S., Thanh, C.-L., Bui, T. Q., and Wahab, M. A., "Damage assessment in composite laminates using ann-pso-iga and cornwell indicator," *Composite Structures*, vol. 230, p. 111 509, 2019.

[63] Qian, C. et al., "Application of artificial neural networks for quantitative damage detection in unidirectional composite structures based on lamb waves," *Advances in Mechanical Engineering*, vol. 12, no. 3, p. 1 687 814 020 914 732, 2020.

[64] Califano, A., Chandarana, N., Grassia, L., D'Amore, A., and Soutis, C., "Damage detection in composites by artificial neural networks trained by using in situ distributed strains," *Applied Composite Materials*, vol. 27, no. 5, pp. 657–671, 2020.

[65] Zenzen, R., Khatir, S., Belaidi, I., Le Thanh, C., and Wahab, M. A., "A modified transmissibility indicator and artificial neural network for damage identification and quantification in laminated composite structures," *Composite Structures*, vol. 248, p. 112 497, 2020.

[66] Mardanshahi, A., Mardanshahi, M., and Izadi, A., "Damage quantification in foam core sandwich composites via finite element model updating and artificial neural networks," *Proceedings of the Institution of Mechanical Engineers, Part C: Journal of Mechanical Engineering Science*, vol. 234, no. 21, pp. 4288–4304, 2020.

[67] Tan, Z. X., Thambiratnam, D. P., Chan, T. H., Gordan, M., and Abdul Razak, H., "Damage detection in steel-concrete composite bridge using vibration characteristics and artificial neural network," *Structure and Infrastructure Engineering*, vol. 16, no. 9, pp. 1247–1261, 2020.

[68] Jang, Y.-J., Kim, H.-J., Kim, H.-G., and Kang, K.-W., "Identification of debonding damage at spar cap-shear web joints by artificial neural network using natural frequency relevant key features of composite wind turbine blades," *Applied Sciences*, vol. 11, no. 12, p. 5327, 2021.

[69] Khatir, S., Tiachacht, S., Le Thanh, C., Ghandourah, E., Mirjalili, S., and Wahab, M. A., "An improved artificial neural network using arithmetic optimization algorithm for damage assessment in fgm composite plates," *Composite Structures*, vol. 273, p. 114 287, 2021.

[70] Tran-Ngoc, H., Khatir, S., Ho-Khac, H., De Roeck, G., Bui-Tien, T., and Wahab, M. A., "Efficient artificial neural networks based on a hybrid metaheuristic optimization algorithm for damage detection in laminated composite structures," *Composite Structures*, vol. 262, p. 113 339, 2021.

[71] Nasser, J., Groo, L., and Sodano, H., "Artificial neural networks and phenomenological degradation models for fatigue damage tracking and life prediction in laser induced graphene interlayered fiberglass composites," *Smart materials and structures*, vol. 30, no. 8, p. 085 010, 2021.

[72] Al-Athel, K. S., Alhasan, M. M., Alomari, A. S., and Arif, A. F. M., "Damage characterization of embedded defects in composites using a hybrid thermography, computational, and artificial neural networks approach," *Heliyon*, vol. 8, no. 8, e10063, 2022.

[73] Feng, B., Ribeiro, A. L., Pasadas, D. J., and Ramos, H. G., "Locating low velocity impacts on a composite plate using multi-frequency image fusion and artificial neural network," *Journal of Nondestructive Evaluation*, vol. 41, no. 2, pp. 1–9, 2022.

[74] Saadatmorad, M., Jafari-Talookolaei, R.-A., Pashaei, M.-H., and Khatir, S., "Damage detection in rectangular laminated composite plate structures using a combination of wavelet transforms and artificial neural networks," *Journal of Vibration Engineering & Technologies*, pp. 1–18, 2022.

[75] Reis, P. A., Iwasaki, K. M., Voltz, L. R., Cardoso, E. L., and Medeiros, R. D., "Damage detection of composite beams using vibration response and artificial neural networks," *Proceedings of the Institution of Mechanical Engineers, Part L: Journal of Materials: Design and Applications*, vol. 236, no. 7, pp. 1419–1430, 2022.

[76] Mouzakis, D. E., Dimogianopoulos, D. G., and Zaoutsos, S., "Damage assessment of carbon fiber reinforced composites under accelerated aging and validation via stochastic model-based analysis," *International journal of damage mechanics*, vol. 23, no. 5, pp. 702–726, 2014.

[77] Nardi, D., Lampani, L., Pasquali, M., and Gaudenzi, P., "Detection of low-velocity impact-induced delaminations in composite laminates using auto-regressive models," *Composite Structures*, vol. 151, pp. 108–113, 2016.

[78] Silva, S. da, Paixão, J., Rébillat, M., and Mechbal, N., "Extrapolation of ar models using cubic splines for damage progression evaluation in composite structures," *Journal of Intelligent Material Systems and Structures*, vol. 32, no. 3, pp. 284–295, 2021.

[79] Paixão, J., Silva, S. da, Figueiredo, E., Radu, L., and Park, G., "Delamination area quantification in composite structures using gaussian process regression and auto-regressive models," *Journal of Vibration and Control*, vol. 27, no. 23-24, pp. 2778–2792, 2021.

[80] Peng, T., Saxena, A., Goebel, K., Xiang, Y., Sankararaman, S., and Liu, Y., "A novel bayesian imaging method for probabilistic delamination detection of composite materials," *Smart materials and structures*, vol. 22, no. 12, p. 125 019, 2013.

[81] Fendzi, C., Mechbal, N., Rebillat, M., Guskov, M., and Coffignal, G., "A general bayesian framework for ellipse-based and hyperbola-based damage localization in anisotropic composite plates," *Journal of Intelligent Material Systems and Structures*, vol. 27, no. 3, pp. 350–374, 2016.

[82] Cantero-Chinchilla, S., Malik, M. K., Chronopoulos, D., and Chiachio, J., "Bayesian damage localization and identification based on a transient wave propagation model for composite beam structures," *Composite Structures*, vol. 267, p. 113 849, 2021.

[83] Huo, H., He, J., and Guan, X., "A bayesian fusion method for composite damage identification using lamb wave," *Structural Health Monitoring*, p. 1 475 921 720 945 000, 2020.

[84] Guo, Y. et al., "Fully convolutional neural network with gru for 3d braided composite material flaw detection," *IEEE Access*, vol. 7, pp. 151 180–151 188, 2019.

[85] Nasiri, A., Bao, J., Mccleeary, D., Louis, S.-Y. M., Huang, X., and Hu, J., "Online damage monitoring of sicf-sicm composite materials using acoustic emission and deep learning," *IEEE Access*, vol. 7, pp. 140 534–140 541, 2019.

[86] Salehzadeh Nobari, A. E. and Aliabadi, M. F., "A multilevel isolation forrest and convolutional neural network algorithm for impact characterization on composite structures," *Sensors*, vol. 20, no. 20, p. 5896, 2020.

[87] Das, A. K., Leung, C. K., and Wan, K. T., "Application of deep convolutional neural networks for automated and rapid identification and computation of crack statistics of thin cracks in strain hardening cementitious composites (shccs)," *Cement and Concrete Composites*, vol. 122, p. 104 159, 2021.

[88] Saadatmorad, M., Jafari-Talookolaei, R.-A., Pashaei, M.-H., and Khatir, S., "Damage detection on rectangular laminated composite plates using wavelet based convolutional neural network technique," *Composite Structures*, vol. 278, p. 114 656, 2021.

[89] Wu, J., Xu, X., Liu, C., Deng, C., and Shao, X., "Lamb wave-based damage detection of composite structures using deep convolutional neural network and continuous wavelet transform," *Composite Structures*, vol. 276, p. 114 590, 2021.

[90] Djavadifar, A., Graham-Knight, J. B., Korber, M., Lasserre, P., and Najjaran, H., "Automated visual detection of geometrical defects in composite manufacturing processes using deep convolutional neural networks," *Journal of Intelligent Manufacturing*, pp. 1–19, 2021.

[91] Augustin, M., Ramesh, V., Prasad, R. K., Gupta, N., and Kumar, M. R., "Detection of inclusion by using 3d laser scanner in composite prepreg manufacturing technique using convolutional neural networks," *Machine Vision and Applications*, vol. 32, no. 6, pp. 1–10, 2021.

[92] Machado, J. M., Tavares, J. M. R., Camanho, P. P., and Correia, N., "Automatic void content assessment of composite laminates using a machine-learning approach," *Composite Structures*, vol. 288, p. 115 383, 2022.

[93] Cui, R., Azuara, G., Lanza di Scalea, F., and Barrera, E., "Damage imaging in skin-stringer composite aircraft panel by ultrasonic-guided waves using deep learning with convolutional neural network," *Structural Health Monitoring*, vol. 21, no. 3, pp. 1123–1138, 2022.

[94] Yang, J., Su, Y., He, Y., Zhou, P., Xu, L., and Su, Z., "Machine learning-enabled resolution-lossless tomography for composite structures with a restricted sensing capability," *Ultrasonics*, vol. 125, p. 106 801, 2022.

[95] Helwing, R., Hülsbusch, D., and Walther, F., "Deep learning method for analysis and segmentation of fatigue damage in x-ray computed tomography data for fiber-reinforced polymers," *Composites Science and Technology*, vol. 230, p. 109 781, 2022.

[96] Barile, C., Casavola, C., Pappalettera, G., and Kannan, V. P., "Laplacian score and k-means data clustering for damage characterization of adhesively bonded cfrp composites by means of acoustic emission technique," *Applied Acoustics*, vol. 185, p. 108 425, 2022.

[97] Pashmforoush, F., Khamedi, R., Fotouhi, M., Hajikhani, M., and Ahmadi, M., "Damage classification of sandwich composites using acoustic emission technique and k-means genetic algorithm," *Journal of Nondestructive Evaluation*, vol. 33, no. 4, pp. 481–492, 2014.

[98] Liu, P. et al., "Damage mode identification of composite wind turbine blade under accelerated fatigue loads using acoustic emission and machine learning," *Structural Health Monitoring*, vol. 19, no. 4, pp. 1092–1103, 2020.

[99] Shrifan, N. H., Jawad, G. N., Isa, N. A. M., and Akbar, M. F., "Microwave non-destructive testing for defect detection in composites based on k-means clustering algorithm," *IEEE Access*, vol. 9, pp. 4820–4828, 2020.

[100] Ech-Choudany, Y., Assarar, M., Scida, D., Morain-Nicolier, F., and Bellach, B., "Unsupervised clustering for building a learning database of acoustic emission signals to identify damage mechanisms in unidirectional laminates," *Applied Acoustics*, vol. 123, pp. 123–132, 2017.

[101] Zeng, X. et al., "Real-time damage analysis of 2d c/sic composite based on spectral characters of acoustic emission signals using pattern recognition," *Acta Mechanica Sinica*, vol. 38, no. 10, pp. 1–18, 2022.

[102] Essassi, K., Rebiere, J.-L., Mahi, A. E., Amine Ben souf, M., Bouguecha, A., and Haddar, M., "Health monitoring of sandwich composites with auxetic core subjected to indentation tests using acoustic emission," *Structural Health Monitoring*, vol. 21, no. 5, pp. 2264–2275, 2022.

[103] Taghizadeh, J. and Ahmadi, M., "Identification of damage modes in polypropylene/epoxy composites by using principal component analysis on ae signals extracted from mode i delamination," *Nondestructive Testing and Evaluation*, vol. 27, no. 2, pp. 151–170, 2012.

[104] Rao, A. R. M., Lakshmi, K., and Kumar, S. K., "Detection of delamination in laminated composites with limited measurements combining pca and dynamic qpso," *Advances in Engineering Software*, vol. 86, pp. 85–106, 2015.

[105] Sierra-Pérez, J., Güemes, A., Mujica, L. E., and Ruiz, M., "Damage detection in composite materials structures under variable loads conditions by using fiber bragg gratings and principal component analysis, involving new unfolding and scaling methods," *Journal of Intelligent Material Systems and Structures*, vol. 26, no. 11, pp. 1346–1359, 2015.

[106] Yan, Z., Chen, C.-Y., Luo, L., and Yao, Y., "Stable principal component pursuit-based thermographic data analysis for defect detection in polymer composites," *Journal of Process Control*, vol. 49, pp. 36–44, 2017.

[107] Mohamad, Z., "Classification for damage severity in natural fibre composites using principal component analysis," *International Journal of Integrated Engineering*, vol. 10, no. 8, 2018.

[108] Lu, S., Jiang, M., Wang, X., and Yu, H., "Damage detection method of cfrp structure based on fiber bragg grating and principal component analysis," *Optik*, vol. 178, pp. 858–867, 2019.

[109] Malinowski, P. H., Wandowski, T., and Singh, S. K., "Employing principal component analysis for assessment of damage in gfrp composites using electromechanical impedance," *Composite Structures*, vol. 266, p. 113 820, 2021.

[110] Lu, S., Dong, H., and Yu, H., "Interlaminar damage assessment method of cfrp laminate based on synchrosqueezed wavelet transform and ensemble principal component analysis," *Composite Structures*, vol. 276, p. 114 581, 2021.

[111] Fredo, A. J., Abilash, R., Femi, R., Mythili, A., and Kumar, C. S., "Classification of damages in composite images using zernike moments and support vector machines," *Composites Part B: Engineering*, vol. 168, pp. 77–86, 2019.

[112] Forero-Ramírez, J.-C., Restrepo-Girón, A.-D., and Nope-Rodríguez, S.-E., "Detection of internal defects in carbon fiber reinforced plastic slabs using background thermal compensation by filtering and support vector machines," *Journal of Nondestructive Evaluation*, vol. 38, no. 1, pp. 1–11, 2019.

[113] Shyamala, P., Mondal, S., and Chakraborty, S., "Numerical and experimental investigation for damage detection in frp composite plates using support vector machine algorithm," *Struct. Monit. Maint*, vol. 5, no. 2, pp. 243–260, 2018.

[114] Gillespie, D. I. et al., "Composite laminate delamination detection using transient thermal conduction profiles and machine learning based data analysis," *Sensors*, vol. 20, no. 24, p. 7227, 2020.

[115] Yue, J., Wang, Y., and Beskos, D., "Uniaxial tension damage mechanics of steel fiber reinforced concrete using acoustic emission and machine learning crack mode classification," *Cement and Concrete Composites*, vol. 123, p. 104 205, 2021.

[116] Xu, J., Liu, X., Han, Q., and Wang, W., "A particle swarm optimization–support vector machine hybrid system with acoustic emission on damage degree judgment of carbon fiber reinforced polymer cables," *Structural Health Monitoring*, vol. 20, no. 4, pp. 1551–1562, 2021.

[117] Sheng, W., Liu, Y., and Söffker, D., "A novel adaptive boosting algorithm with distance-based weighted least square support vector machine and filter factor for carbon fiber reinforced polymer multi-damage classification," *Structural Health Monitoring*, p. 14 759 217 221 098 173, 2022.

[118] Rajiv, B., Kalos, P., Pantawane, P., Chougule, V., and Chavan, V., "Classification of damages in composite material using multi-support vector machine," *Journal of The Institution of Engineers (India): Series C*, pp. 1–7, 2022.

[119] Alhammad, M. et al., "Automated impact damage detection technique for composites based on thermographic image processing and machine learning classification," *Sensors*, vol. 22, no. 23, p. 9031, 2022.

[120] Pashmforoush, F., Fotouhi, M., and Ahmadi, M., "Acoustic emission-based damage classification of glass/polyester composites using harmony search k-means algorithm," *Journal of Reinforced Plastics and Composites*, vol. 31, no. 10, pp. 671–680, 2012.

[121] Selva, P., Cherrier, O., Budinger, V., Lachaud, F., and Morlier, J., "Smart monitoring of aeronautical composites plates based on electromechanical impedance measurements and artificial neural networks," *Engineering Structures*, vol. 56, pp. 794–804, 2013.

[122] Crivelli, D., Guagliano, M., and Monici, A., "Development of an artificial neural network processing technique for the analysis of damage evolution in pultruded composites with acoustic emission," *Composites Part B: Engineering*, vol. 56, pp. 948–959, 2014.

[123] Mardanshahi, A., Nasir, V., Kazemirad, S., and Shokrieh, M., "Detection and classification of matrix cracking in laminated composites using guided wave propagation and artificial neural networks," *Composite Structures*, vol. 246, p. 112 403, 2020.

[124] Chen, G. L., Yanamandra, K., and Gupta, N., "Artificial neural networks framework for detection of defects in 3d-printed fiber reinforcement composites," *JOM*, vol. 73, no. 7, pp. 2075–2084, 2021.

[125] Hamdi, K., Moreau, G., and Aboura, Z., "Digital image correlation, acoustic emission and in-situ microscopy in order to understand composite compression damage behavior," *Composite Structures*, vol. 258, p. 113 424, 2021.

[126] Dziendzikowski, M., Heesch, M., Gorski, J., Dragan, K., and Dworakowski, Z., "Application of pzt ceramic sensors for composite structure monitoring using harmonic excitation signals and bayesian classification approach," *Materials*, vol. 14, no. 19, p. 5468, 2021.

[127] Scholz, V., Winkler, P., Hornig, A., Gude, M., and Filippatos, A., "Structural damage identification of composite rotors based on fully connected neural networks and convolutional neural networks," *Sensors*, vol. 21, no. 6, p. 2005, 2021.

[128] Lee, I. Y., Roh, H. D., Park, H. W., and Park, Y.-B., "Advanced non-destructive evaluation of impact damage growth in carbon-fiber-reinforced plastic by electromechanical analysis and machine learning clustering," *Composites Science and Technology*, vol. 218, p. 109 094, 2022.

[129] Allen, H. G., *Analysis and design of structural sandwich panels: the commonwealth and international library: structures and solid body mechanics division*. Elsevier, 2013.

[130] Ma, Q., Rejab, M., Siregar, J., and Guan, Z., "A review of the recent trends on core structures and impact response of sandwich panels," *Journal of Composite Materials*, vol. 55, no. 18, pp. 2513–2555, 2021.

[131] Barbero, E. J., *Introduction to composite materials design*. CRC press, 2010.

[132] Carlsson, L. A. and Kardomateas, G. A., *Structural and failure mechanics of sandwich composites*. Springer Science & Business Media, 2011, vol. 121.

[133] Hassani, S., Mousavi, M., and Gandomi, A. H., "Structural health monitoring in composite structures: A comprehensive review," *Sensors*, vol. 22, no. 1, p. 153, 2021.

[134] Kaszynski, A., *pyansys: Pythonic interface to MAPDL*, version 0.60.3, Nov. 2021. DOI: 10.5281/zenodo.4009466. [Online]. Available: https://doi.org/10.5281/zenodo.4009466.

[135] Chollet, F. et al., *Keras*, https://keras.io, 2015.

[136] Garnett, R., *Bayesian optimization*. Cambridge University Press, 2023.

[137] Hu, J., Shen, L., and Sun, G., "Squeeze-and-excitation networks," in *Proceedings of the IEEE conference on computer vision and pattern recognition*, 2018, pp. 7132–7141.

[138] Canny, J., "A computational approach to edge detection," *IEEE Transactions on pattern analysis and machine intelligence*, no. 6, pp. 679–698, 1986.

[139] Pandey, A., Biswas, M., and Samman, M., "Damage detection from changes in curvature mode shapes," *Journal of sound and vibration*, vol. 145, no. 2, pp. 321–332, 1991.

[140] Sobel, I., "An isotropic 3× 3 image gradient operater," *Machine vision for three-dimensional scenes*, pp. 376–379, 1990.

[141] Othman, G. and Zeebaree, D. Q., "The applications of discrete wavelet transform in image processing: A review," *Journal of Soft Computing and Data Mining*, vol. 1, no. 2, pp. 31–43, 2020.